Title
Electronic Transitions in Perovskite Oxide Heterostructures

Author
Wong, Franklin

Publication Date
2011

Peer reviewed|Thesis/dissertation

Electronic Transitions in Perovskite Oxide Heterostructures

By

Franklin Wong

A dissertation submitted in partial satisfaction of the

requirements for the degree of

Doctor of Philosophy

in

Engineering – Materials Science and Engineering

in the

Graduate Division

of the

University of California, Berkeley

Committee in charge:

Professor Yuri Suzuki, Chair

Professor Daryl C. Chrzan

Professor Ture K. Gustafson

Spring 2011

Electronic Transitions in Perovskite Oxide Heterostructures

Abstract

Electronic Transitions in Perovskite Oxide Heterostructures

by
Franklin Wong
Doctor of Philosophy in Materials Science and Engineering
University of California, Berkeley
Professor Yuri Suzuki, Chair

The focus of this dissertation is on tuning electronic phase transitions in perovskite oxide heterostructures. The recurring theme is the exploitation of characteristics inherent to heteroepitaxy that are unavailable in the bulk materials of identical chemistry; these inherent characteristics are epitaxial strain and interfacial electronic reconstruction. In contrast, the effects of chemical substitution, for example, are not defining traits of heterostructures as they can be routinely studied in bulk materials, and therefore will not be included in this work.

Heteroepitaxial lattice deformation is identified to be crucial in two systems: coherently strained $LaTiO_3$ films on $SrTiO_3$ substrates and $La_{2/3}Sr_{1/3}MnO_3$ films on $LaAlO_3$ substrates. One the other hand, interfacial charge transfer is the responsible for the insulator-metal transitions in $LaAlO_3$ films on $SrTiO_3$ substrates, or $LaAlO_3/SrTiO_3$ heterointerfaces. The charge, orbital, spin, and lattice "degrees of freedom" are intimately linked in perovskite oxides, particularly those containing transition metals. The lattice can be modified through heteroepitaxial strain, and the charge state can be modified through interfacial electronic reconstruction.

It is shown that epitaxial strain can induce an insulator-metal transition in $LaTiO_3$, which is a Mott insulator in the bulk that is near an electronic instability owing to its orbital disorder. It is confirmed that metallic conduction occurs throughout the entire thicknesses of the $LaTiO_3$ films, as opposed to being confined to the surfaces or interfaces. It is possible to exploit heteroepitaxial strain as a knob to modulate the electronic bandwidth. Strain values that can be introduced routinely in thin films are greater than those which are easily accessible in hydrostatic or uniaxial stress studies of bulk materials.

Epitaxial strain also is explicitly linked to the enhanced magnetoresistive properties of $La_{2/3}Sr_{1/3}MnO_3$ films, particularly at low temperatures. The key effect appears to be the stabilization of a more insulating phase that may coexist with the double-exchange metallic ferromagnetic phase, which is stable in the bulk. The more insulating phase in turn becomes unstable upon the application of a magnetic field, resulting in higher magnetoresistance over a wide range of temperatures. While such a mechanism is certainly believed to be pertinent for many bulk manganites, it is not expected to be relevant for the specific chemical composition studied. Similar to the case of $LaTiO_3$, the orbital degrees of freedom in $La_{2/3}Sr_{1/3}MnO_3$ are important for the tunability of such an electronic transition controlled by thin-film lattice deformation; an added ingredient is that there exist two competing magnetic exchange mechanisms that are sensitive to chemical bonding. Both the orbital degree of freedom and competing exchange interactions make the electronic properties of manganite films very sensitive to external lattice perturbations.

Finally, metallic $LaAlO_3/SrTiO_3$ heterointerfaces between two nominally undoped insulators are examined. Interfacial polarity is believed to induce electron transfer from $LaAlO_3$ to $SrTiO_3$. Low-temperature magnetotransport studies reveal signatures of strong spin-orbit interaction in this quasi-two-dimensional metallic channel. The spin-orbit coupling in the heterostructures is enhanced greatly by interfacial electric fields; hence, it represents a property that is fundamentally non-bulk-like. The transport data presented in this work suggest that disorder and carriers are introduced concurrently at the heterointerface, and also shed light on the origin of metallicity.

Electronic Transitions in Perovskite Oxide Heterostructures

Table of Contents

Acknowledgments iv

Chapter 1: Challenges and Opportunities in Complex Oxide Heterostructures

1.1. The challenge of controlling complexity 2
1.2. The complexity of complex oxides 4
1.3. Thin-film deposition technology as an enabler to oxide research 5
1.4. Options to tune the charge and lattice variables 7
1.5. General approach and synopsis of subsequent chapters 8

Chapter 2: Experimental

2.1 Pulsed-laser deposition 12
2.2 Reflective high energy electron diffraction 13
2.3 Atomic force microscopy 13
2.4 Transmission electron microscopy 14
2.5 Rutherford backscattering spectrometry 14
2.6 X-ray diffraction 15
2.7 SQUID magnetometry 17
2.8 Electrical transport 18

Chapter 3: Basic Aspects of Correlated Perovskite Oxides

The Perovskite Structure: Atomic and Electronic

3.1 The cubic perovskite 21

3.2 The distorted perovskite 25

Correlated Electron Systems

3.3 One-electron approximation 27
3.4. Failure of the one-electron approximation 29
3.5 The Hubbard model 30
3.6 A comment of the classification of correlated insulators 32
3.7 Magnetism in correlated oxides 33
3.7.1 Antiferromagnetic coupling from superexchange 33
3.7.2 Ferromagnetic coupling from superexchange 34

Chapter 4: Strain-induced metallicity in $LaTiO_3$ thin films

4.1. Proximity to electronic instability of bulk $LaTiO_3$ 38
4.2. Growth and structure of $LaTiO_3$ thin films 41
4.3. Substrate-dependent electrical transport of $LaTiO_3$ films 45
4.4. Strain-induced metallicity of $LaTiO_3$ films on $SrTiO_3$ substrates 48
4.5. Elimination of other potential sources of metallicity 50
4.6. Outlook on strain engineering of electronic transitions in single-valent oxides 55
4.7. Concluding remarks 56

Chapter 5: Strain-enhanced Magnetoresistance in $La_{2/3}Sr_{1/3}MnO_3$ films

5.1. Double exchange and ferromagnetism 59
5.2. Phase separation and it role in colossal magnetoresistance 60
5.3. General concept and scope of this work 65
5.4. Samples studied and their structures 66
5.5. Thin-film magnetism and magnetotransport 72
5.5.1. Electrical transport 72
5.5.2. Magnetism 73
5.5.3. Magnetotransport 74
5.6. The significance of strain coherency in (001) films 79
5.7. On the possibility of strain-induced phase separation 80
5.8. Can phase separation be tuned? 83
5.9. Conclusions and outlook 83

Chapter 6: Disorder, Magnetotransport, and Spin-Orbit Interaction at $LaAlO_3/SrTiO_3$ Heterointerfaces

6.1. Discovery of and work on metallic (001) $LaAlO_3/SrTiO_3$ interfaces 86
6.2. Interfacial carrier gases in semiconductor heterostructures 89
6.3. Growth and structure of $LaAlO_3$ films on $SrTiO_3$ substrates 91
6.4. Temperature- and $LaAlO_3$ thickness-dependent electrical transport 92
6.5. Low-temperature quantum correction to conductance 96
6.6. Magnetotransport and its anisotropy 97
6.7. Possible origin of disorder and spin-orbit interaction 102
6.8. Exploiting spin-orbit interaction 108
6.9. Conclusions and outlook 110

Afterword 112

Appendix

A.1. Heteroepitaxial strain in thin films 115
A.1.1. Strain and stress as thermodynamic conjugate pairs 115
A.1.2. Physical interpretation of the strain and stress tensors 116
A.1.3. Matrix representation 119
A.1.4. Heteroepitaxial lattice distortions 120
A.2. Disorder and localization in two-dimensional systems 122
A.2.1. Coherent backscattering in electronic systems 123
A.2.2. The competition of disorder and carrier density in localization . . . 124
A.2.3. Quantum correction to conductance 125
A.2.4. Effect of applied magnetic fields on weak (anti)localization 126
A.3. Ferromagnetic coupling through superexchange interaction 128

References 131

Acknowledgments

All of the work in this dissertation was made possible by Yuri's careful guidance. Yuri gives the perfect combination of independence and instruction, of attention to details and searching for big ideas, of encouragement and critique for nurturing a young, aspiring scientist. The collaborative and collegial atmosphere she creates in the lab has allowed me to learn much more than I had ever thought I would have. Much thanks to her.

Special thanks also to Shaobo Zhu, who worked with me as an undergraduate—now a graduate student at Cornell, my alma mater. He helped take some of the data in Chapter 5.

I appreciate the gang of graduate students in my lab: Virat Mehta, without whom I would feel less comfortable doing anything in lab; Jodi Iwata, whose enthusiasm and work ethic are contagious and who is a wonderful Materials Research Society chapter president; Alex Grutter, whose light-hearted spirit doesn't get in the way of fixing serious SQUID problems; Urusa Alaan, whose dedication and devoted work schedule are undoubtedly unmatched; and two first-years, Ted Sanders and Matthew Gray, who have proven themselves to be impressionable yet quite impressive. Thank you, guys.

I would like to thank a collaborator, Jeremy Levy, Professor of Physics and Astronomy at the University of Pittsburgh. The many discussions with him led to some of the ideas presented at the end of Chapter 6. I would like to also acknowledge Seung-Hyub Baek and Professor Chang-Beom Eom, Department of Materials Science and Engineering at the University of Wisconsin, Madison, for their assistance in four-circle x-ray diffraction before I had access to a high-resolution diffractometer on campus. Professor Eom's persistence helped improve the quality of work in Chapter 4. Elke Arenholz, staff scientist at the Advanced Light Source, has been extremely helpful in translating textbook information to user inputs at a beamline endstation.

In addition to being top-notch researchers who push the frontier of knowledge, many faculty members at Berkeley are great teachers who educate and inspire the next generation. In my Master of Science thesis, I thanked Professor Peter Yu (Emeritus) of

Physics and Professor Kenneth Raymond of Chemistry. I would like to do so again. So grateful I am that I took Professor Yu's semiconductor class the year before he retired. It was there where I started to appreciate the beauty of solid-state physics. As it still stands today, my knowledge of chemistry, very modest it is, was largely acquired in the class on chemical bonding taught by Professor Raymond. I love the physical intuition prescribed by molecular orbital theory. I would like to extend my gratitude to the members of my dissertation committee. Professor Daryl Chrzan of Materials Science taught me the tight-binding approach to electronic structure, which serves as the framework for a great deal of the discussion found in this dissertation. Of course, the student will assume all of the blame for any imprecision and mistakes. Professor Chrzan also provided an exceedingly lucid explanation of Monte Carlo simulations, which helped me understand many seminal papers in the field of manganites. Finally, Professor Ture Gustafson (Emeritus) of Electrical Engineering taught me everything I know about electromagnetic radiation; I think about his class whenever I work at a beamline. Incidentally, I will never quite forget Chapter 9 of Jackson's text.

To the many friends in Berkeley and New York City: You know who you are!

Finally, I would like to thank my family for their support over the last six years. They didn't think it would have taken so long. Of course I would tell them that I waited so that my sister, four years more junior, and I will graduate in the same year—she with a Doctor of Pharmacy degree. Skillfully planned, my dad will make it back to the States from China a few days before my commencement day. Last but definitely not least, it amazes me how my mom has gotten so much smarter as I've gotten older in graduate school.

If we knew what it was we were doing, it would not be called research, would it?

- Albert Einstein

Chapter 1

Challenges and Opportunities in Complex Oxide Heterostructures

1.1. The challenge of controlling complexity 2
1.2. The complexity of complex oxides 4
1.3. Thin-film deposition technology as an enabler to oxide research 5
1.4. Options to tune the charge and lattice variables 7
1.5. General approach and synopsis of subsequent chapters 8

Ever since Sir Nevill Mott pointed out the paradoxical insulating properties of NiO in 1949 [1], we have been cognizant of the strong electronic correlations that give rise to complexity in transition-metal oxides. Recent advancements in materials fabrication, particularly in thin-film deposition, have sparked renewed interest in this class of materials. This dissertation is an experimental investigation of electronic transitions in three different complex oxide heterostructures: strained $LaTiO_3$ and $La_{2/3}Sr_{1/3}MnO_3$ thin films as well as $LaAlO_3/SrTiO_3$ heterointerfaces. The ideas of *complexity* and *interactions* are introduced, and throughout the dissertation they are shown to play crucial roles in electronic phase stability and transitions in oxides. The challenges and opportunities in this field of research are briefly overviewed.

§ 1.1 The challenge of controlling complexity

In the physical sciences there has been an increased effort to study and understand *complex* phenomena. *Complexity* exists in systems in which strong interactions among the constituent parts lead to unexpected properties in the whole. The potential of complex oxide research in particular is highlighted in the 2007 Department of Energy (DOE) Office of Basic Energy Sciences Grand Challenges report [2], featuring a scanning transmission electron microscope image of a $SrTiO_3/LaTiO_3$ superlattice by Ohtomo *et al*. [3] on its cover (Fig. 1.1). The Grand Challenges report, titled "Directing Matter and Energy: Five Challenges for Science and the Imagination," suggests that complexity in materials systems* is a key concept to understand and exploit in tackling tomorrow's scientific challenges.

In systems with complex interactions, unanticipated phenomena can emerge. To understand and ultimately control emergent properties, we must explore the rules governing interactions in different systems individually. In fact, the topic is introduced in the book *Sync* by Steven Strogatz, in which he examines different examples of synchronization and emergent behavior in nature—such as the emergence of thought from thoughtless neurons to unthinking fireflies blinking in unison [4]. What are the governing laws that determine the emergent outcomes? The premise is that such governing laws do exist; the challenge is to discover them case by case for different interacting systems.

In the physical sciences, Philip Anderson was the first to form a systematic line of inquiry to approach the investigation of complexity. He points out that more is not only more: more is also different [5]. Often the line of physical science inquiry falls into one of two classes: (1) reductionism that aims to break systems down to their "fundamental" constituents and understand the each component individually and (2) emergence that focuses on how the properties of the system as a whole manifest from interactions. The case for the more holistic emergence approach is that new phenomena, distinctly different from the separate parts in themselves, come about as a consequence of scale

* Ideas of complexity have been more well-known and applied in the social, economic, biological, and computer sciences.

and interactions. Though the whole is comprised of the individual parts, the sum of these parts does not necessarily constitute the entire whole; interactions among the parts need to be considered as well. Regardless, the two "schools" of scientific approach should not be viewed as necessarily mutually exclusive either.

Aside from complex materials, heterostructures provide another exciting and vast playground to realize emergent phenomena, manifested in interfacial properties not exhibited by the constituent materials themselves. A perfect example is giant magnetoresistance exhibited in multilayers of magnetic and nonmagnetic metallic films; the phenomenon of giant magnetoresistance illustrates that an emergent functionality can be explicitly linked to interfaces [6]. The recurrent theme is that the whole in most cases is indeed greater than the sum of the parts.

Ultimately, the task of understanding and subsequently controlling emergent properties is truly daunting, as the very unpredictability of emergence is the reason for interest in the field. In the field of complexity, we are tasked with becoming acquainted with, tuning, designing, and predicting this perceived "unpredictability."

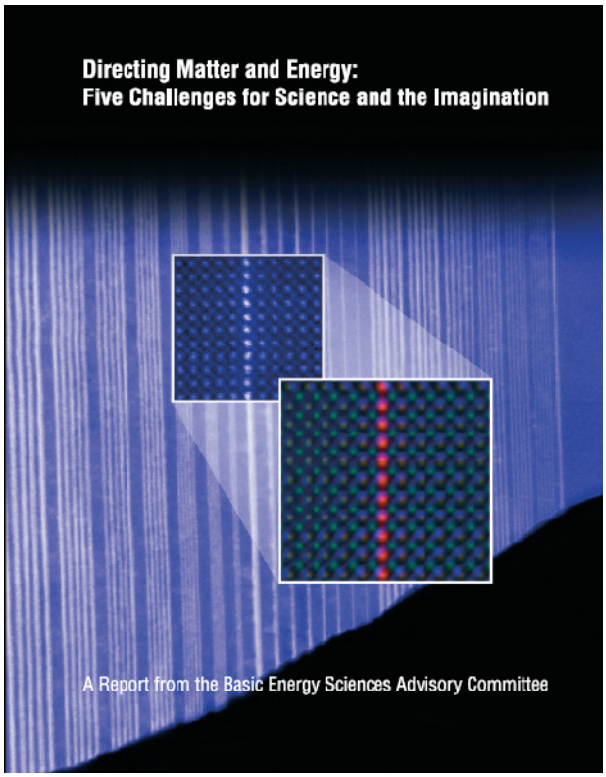

Figure 1.1. Cover of the 2007 DOE Grand Challenges report, showing an image of a $LaTiO_3/SrTiO_3$ superlattice taken by Ohtomo *et al.* [3]. (From Ref. [2])

§ 1.2 The complexity of complex oxides

Interacting parts are at the heart of complexity. The work in this dissertation is focused on complex oxides, a class of materials in which the charge, spin, orbital, and lattice variables are intimately coupled and the interactions are particularly strong. As a result of strong coupling, for example, a change of the charge state by chemical substitution or a modification of the lattice state by external stress in a material will alter the other variables, such that new functionalities can be achieved.

In the past, difficulties in reliable materials synthesis have prevented detailed examination of tailored samples. The demonstration of the precise, atomic-level control of the $SrTiO_3/LaTiO_3$ superlattice (Fig. 1.1), a complex oxide heterostructure, drew the attention of the DOE Grand Challenges committee. Advances in oxide thin-film deposition have enabled further and more detailed investigations of intrinsic materials properties, suggesting the potential and possibilities of carefully selected materials combinations. However, we should not confuse improved fabrication with the truly grand goal of engineering materials properties. For technological applications not only do we have to understand governing principles of exotic emergent properties, but we also must learn ways to tune these properties on demand.

In condensed matter systems, interactions among particles can lead to ordering. A familiar example of ordering is the spontaneous magnetization of a ferromagnet below its Curie temperature. Ordered states resulting from interactions are often called cooperative phenomena. As shown in Fig. 1.2, whereas the moments of a ferromagnet align randomly above its Curie temperature, correlated moment alignment and therefore spontaneous magnetization emerge below its Curie temperature. In a ferromagnet, adjacent spins preferentially align. In the ordered phase of a superconductor below its transition temperature, Cooper pairs move in-phase with one another to expel magnetic fields from the material and allow for frictionless electrical transport. Another cooperative phenomenon is ferroelectricity. As the ordered and disordered phases of a material would invariably have different measurable properties, engineering control of ordering will be technologically significant, and will require the tuning of complex interactions in materials systems.

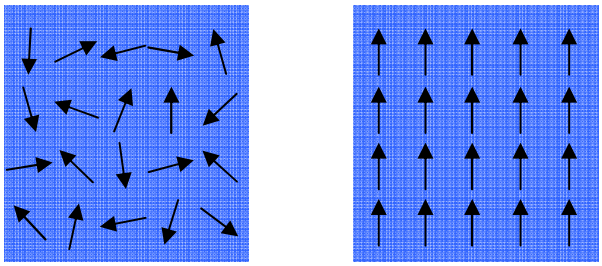

Figure 1.2. Schematics of (a) a disordered spin phase with no net moment above the Curie temperature and (b) an ordered ferromagnetic phase with a non-zero net moment below the Curie temperature.

In the case of a ferromagnet as shown in Fig. 1.2, the order-disorder transition can be traversed by changing the temperature; moreover, other thermodynamic forces—such as an electric field, magnetic field, stress, and chemical potential—can also induce phase transitions. Here a *phase* is defined as any, or any portion of a, material that has well-defined properties. For technological viability of complex oxides for electronic applications, the specific challenges are to discover, design, and engineer materials that are sensitive to any one or more of the aforementioned thermodynamic forces.

§ 1.3 Thin-film deposition technology as an enabler to oxide research

The superlattice in Fig. 1.1 is comprised of perovskite thin films. This dissertation is a study exclusively on perovskite oxides. The perovskite oxide structure ABO_3 is shown in Fig. 1.3 and some of its features will be briefly presented here; a more detailed discussion can be found in Chapter 3. The oxygen anions form an octahedral cage. Within that cage, typical B atoms (cations) include most transition metals, Ga, and Al. The coordination of the A site is 12, and larger atoms (cations) can occupy that site—including alkaline-earth metals, rare-earth metals, Bi, and Pb. With such a robust structure that can serve as a host for a vast combination of crystal chemistry, perovskite oxides exhibit an array of phenomenology: superconductivity,[†] ferroelectricity, magnetic ordering, colossal magnetoresistance, multiferroism, and so on. Because many transition metals can assume several valence states, A-site chemical substitution can be used to tailor the desired valence state of a particular transition metal cation.

Certainly even bulk perovskite oxides are fascinating, and many of them had been well-studied in previous decades. However, propelled largely by advances in thin-film deposition, the field of perovskite oxide *heterostructures* has garnered much current attention. Advances include better control of deposition techniques, higher-quality crystalline substrates, and development of high-pressure reflective high energy electron diffraction to monitor thin-film growth. Structures comparable to the one shown in Fig. 1.1 now can be routinely fabricated. In the field of oxide heterostructures, we are particularly focused on phenomena unique to heterostructures and inaccessible in the bulk materials.

The three main deposition techniques used are oxide molecular beam epitaxy, RF sputtering, and pulsed-laser deposition [7]. Because of the vast array of crystal chemistry available in the perovskite structure, physical deposition techniques allow for more flexibility than chemical-based techniques. Whereas in oxide molecular beam epitaxy, elemental metal targets are employed, oxide ceramic pressed powder targets are typically used in RF sputtering and pulsed-laser deposition. Oxide molecular beam epitaxy is better suited for (001) heteroepitaxy, but heteroepitaxy of different crystal orientations are readily accessible in RF sputtering and pulsed-laser deposition. The

[†] The most famous cuprate perovskite oxide has an A_2BO_4 structure, rather than an ABO_3 structure.

samples in this manuscript are grown using pulsed-laser deposition, and further details are provided in Section 2.1.

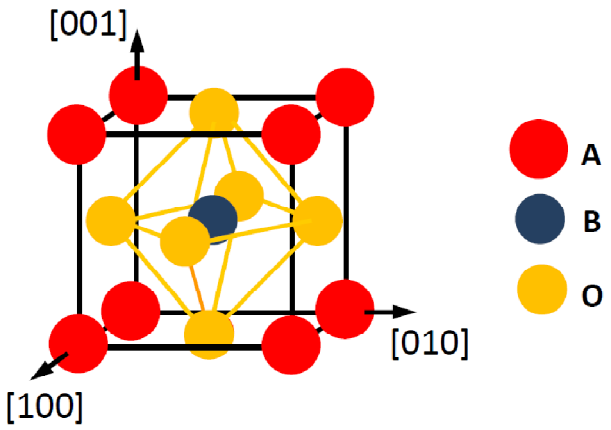

Figure 1.3. A cubic perovskite oxide ABO_3 unit cell.

Another enabler for controlled oxide thin-film synthesis is the number of high structural quality oxide substrates commercially available. Table 1.1 is a list of all of the substrates appropriate for perovskite oxide heteroepitaxy available through commercial vendors. Though most of the listed substrates are of the perovskite structure, as are the materials investigated in this dissertation, $SrLaGaO_4$ and $SrLaAlO_4$ are not; however, their in-plane cubic structure is nevertheless suitable for (001) perovskite thin-film growth, and their out-of-plane lattice parameter is not relevant. Table 1.1 also lists the in-plane lattice parameters for the different substrates. The range of psuedocubic lattice parameters[‡] of available substrates cover the spectrum of those typical for perovskite oxides, particularly the ones with 3*d* transition metals in the B sites; furthermore, the range of substrates allow for the application of various degrees of strain in thin films and the creation of a variety of film/substrate heterointerfaces.

The development of reflective high energy electron diffraction with differential pumping has made *in-situ* monitoring of thin-film growth by electron diffraction possible even when high ambient deposition pressures are required. Although for the deposition of a single film, high crystallinity can be achieved even without *in-situ* monitoring, it is definitely necessary for the fabrication of superlattices of nearly atomic abruptness, as in Fig. 1.1.

The major advances in thin-film growth techniques have stirred much renewed interest in complex oxides. The hope is from controllable growth, many of the properties of oxides can be henceforth manipulated. Many emergent phenomena and tunable functionalities may come about from carefully designed oxide heterostructures.

[‡] Many perovskites are slightly distorted from the perfectly cubic structure. But because the distortions are typically small, using a pseudocubic structure as a reference is a good starting point. The approach is elucidated in Section 3.2.

Table 1.1. List of oxide substrates and their in-plane lattice parameters. For the materials that are orthorhombic in-plane (*), the average of orthogonal in-plane lattice parameters (*a*) is listed.

Substrate	*a* (Å)
$KTaO_3$	3.99
$GdScO_3$*	3.965
$DyScO_3$*	3.94
$SrTiO_3$	3.905
$(LaAlO_3)_{0.3}(Sr_2AlTaO_6)_{0.7}$	3.87
$NdGaO_3$*	3.855
$SrLaGaO_4$	3.84
$LaAlO_3$	3.79
$SrLaAlO_4$	3.75
$YAlO_3$*	3.69

§ 1.4 Options to tune the charge and lattice variables

Certainly, with the combination of aliovalent and isovalent A-site alloying, one can tune the charge and lattice variables of the oxides. Bulk materials properties have largely been studied and tuned through crystal chemistry. However, thin films and heteroepitaxy offer alternative routes. A brief discussion of several pieces of representative work is presented; what follows is by no means an exhaustive survey. The approach of this dissertation is presented in the next section.

Naturally, in a heteroepitaxial system, the lattice state of the film is changed through substrate-induced strain. The goal is to identify a material or group of materials whose properties or even electronic ground states can be profoundly altered by elastic structural deformation. $SrTiO_3$ is a paraelectric insulator that undergoes a cubic-to-tetragonal transition at 105 K and exhibits large dielectric permittivity at low temperatures [8]. Its structural transition is antiferrodistortive in nature, inhibiting long-range electric ordering. However, it is also known that very similar materials such as $BaTiO_3$ and $PbTiO_3$ are ferroelectric. Therefore, one can surmise that $SrTiO_3$ has the basic ingredients for electric ordering. Haeni *et al.* found in-plane electric polarization and ordering at room temperature in $SrTiO_3$ thin films that were tensily strained in plane by $DyScO_3$ substrates [9]. In a similar spirit, Lee *et al.* found that $EuTiO_3$ thin films tensily strained in plane by $DyScO_3$ substrates undergo a paraelectric-to-ferroelectric transition at 250 K and a paramagnetic-to-ferromagnetic transition at about 4 K, whereas the unstrained material is expected to be a ground-state paraelectric antiferromagnet [10]. These studies demonstrate the viability and promise of exploiting lattice

deformation to create ground states that do not exist in bulk materials of the same stoichiometry.

The most lucrative approach for controlling the charge variable in semiconductors is by applying electric fields. The field-effect transistor is the workhorse electronic device not only for applications, but also for realization of fundamental physical phenomena; von Klitzing discovered the quantum Hall effect in a metal-oxide-semiconductor field-effect transistor by using the gate voltage to modulate the channel carrier concentration [11]. Similarly, replacing silicon with an oxide semiconductor such as $SrTiO_3$ or $KTaO_3$ and using Al_2O_3 as the gate dielectric, field-effect channels can be created in oxide semiconductors [12]. However, surface states at the $SrTiO_3/Al_2O_3$ and $KTaO_3/Al_2O_3$ (oxide semiconductor/insulator) interfaces limit the controllability of such structures. Field-effect control can be applied to more correlated materials as well. Scherwitzl *et al*. demonstrated the tunability of the metal-insulator transition temperature in $NdNiO_3$ films using gold contacts and an ionic liquid for gate control [13].[§] In correlated materials, there can be many carriers but they may not very mobile; the issue of screening remains controversial [14].

It is reasonable to guess that the incorporation of isostructural oxide insulators grown epitaxially as barrier materials can improve the performance of oxide field-effect structures. However, the work of Ohtomo and Hwang on metallic $LaAlO_3/SrTiO_3$ interfaces suggests that the formation of oxide heterointerfaces between well-chosen materials can be sufficient to generate a vast array of properties unexpected in the bulk constituent materials [15]. Electron redistribution at oxide heterointerfaces is an avenue to change the charge degree of freedom. Similarly, in modulation-doped semiconductor heterojunctions, rather than being reliant on an applied electric field to bring about a metallic state in semiconductors, quasi-electric fields through band offset engineering aid the transfer of carriers and creation of a metallic interface [16].

§ 1.5 General approach and synopsis of subsequent chapters

Taking advantage of epitaxial strain and heterointerfacial charge transfer to modify materials properties is definitely not unique to oxide materials. In fact, in quantum well lasers, heterointerfacial band offset engineering is used to confine both electrons and holes in the well for optical gain [16]; furthermore, epitaxial strain to used to reduce the threshold current for lasing [17]. Given that the charge and lattice degrees of freedom can be so well engineered in weakly correlated semiconductors, the goal is to achieve comparable control in oxides, in which the charge, lattice, orbital, and spin states are much more strongly coupled. Understanding the parameters that affect interactions in correlated materials will enable tunability and therefore functionalization of their properties.

The overall theme of this dissertation is to broadly address the question: How can we exploit oxide heteroepitaxy to achieve different properties inaccessible in bulk

[§] $NdNiO_3$ is an insulator at low temperatures and a metal at high temperatures.

constituent materials of the same stoichiometry? There is a special emphasis on metal-insulator transitions. Different materials systems are explored for comparison and contrast. The dissertation contains two examples wherein lattice distortions are the key component: strained $LaTiO_3$ (Chapter 4) and $La_{2/3}Sr_{1/3}MnO_3$ (Chapter 5) films. An example wherein interfacial charge transfer is more crucial is $LaAlO_3/SrTiO_3$ interfaces (Chapter 6). The role of electron correlations will be discussed in each case specifically.

Details of the experimental setup and procedures can be found in Chapter 2.

Chapter 3 is a brief overview of the most important physical concepts that will be used throughout the dissertation. Topics include the structure of perovskite oxides, Hubbard's model Hamiltonian for correlated electron systems, and superexchange magnetic interactions in oxides.

Chapter 4 discusses a strain-induced insulator-metal transition in $LaTiO_3$ thin films. $LaTiO_3$ is a Mott insulator on the brink of an electronic transition, which can be deduced from its small band gap and orbital disorder. The data presented in this manuscript is the first study that links the electronic transition in $LaTiO_3$ to tetragonal lattice distortions. A number of other possible sources of metallicity in $LaTiO_3$ films on $SrTiO_3$ substrates have been considered and systematically ruled out. Possible heteroepitaxial strain-induced electronic transitions of other single-valent perovskite oxides,[**] especially ones with orbital degrees of freedom, are considered in the context of the observations in $LaTiO_3$ films.

Chapter 5 discusses strain-induced enhancement of magnetoresistance in $La_{2/3}Sr_{1/3}MnO_3$ films, a mixed-valent system. The improved magnetoresistive properties are likewise related to lattice deformation. Here the data suggest that the underlying mechanism is related to strain-induced stabilization of a low-temperature, insulating state coexisting with a double exchange metal—the stable bulk phase. Whereas other works have demonstrated the Curie transition temperatures of $La_{2/3}Sr_{1/3}MnO_3$ films do indeed depend on strain, the work in Chapter 5 further suggests the potential of engineering magnetoresistance. In addition, it is proposed that rich phase diagrams of different magnetically ordered states can be generated through lattice deformation in lieu of chemical composition.

The possible origins and the nature of the metallic state of $LaAlO_3/SrTiO_3$ heterointerfaces are presented in Chapter 6. This work offers a unified description of the origins of metallicity, still an intensely debated topic, and the creation of disorder in the quasi-two-dimensional electron channel. Low-temperature localization studies reveal the prominence of spin-orbit interaction at the heterointerface. Conductivity along a channel confined to a heterointerface of a *d*-valent system warrants much further investigation. Possible ways to utilize the unexpectedly strong spin-orbit interaction are suggested.

Both strain-induced and interfacial phenomena figure to be lasting themes in oxide heterostructures. Final comments on the work presented in this dissertation and possible future directions of the field of perovskite oxide heterostructures can be found in the Afterword.

[**] Single- or mixed-valency refers to that of the B-site cation.

The Appendix offers reference material on elastic deformation, weak localization, and a superexchange interaction calculation.

Chapter 2

Experimental

2.1 Pulsed-laser deposition 12
2.2 Reflective high energy electron diffraction 13
2.3 Atomic force microscopy 13
2.4 Transmission electron microscopy 14
2.5 Rutherford backscattering spectrometry 14
2.6 X-ray diffraction 15
2.7 SQUID magnetometry 17
2.8 Electrical transport 18

This chapter briefly overviews the oxide thin-film deposition as well as structural, electrical, and magnetic characterization techniques used in the work of this dissertation.

§ 2.1 Pulsed-laser deposition

All of the films studied in this dissertation were deposited using pulsed-laser deposition, which became a relatively widely used research technique in the 1990s because of its success in fabricating high-T_c superconducting oxide thin films. Since then, it has been used as a deposition tool for not only many different types of thin-film oxides but also nitrides and chalcogenides. Because of the availability of safe gaseous oxygen sources that can be readily cracked, pulsed-laser deposition is particularly versatile for oxides.

In pulsed-laser deposition, a laser beam is directed into a vacuum system to hit a polycrystalline sintered ceramic target, which ablates a plume of material that is then deposited on a substrate. A KrF excimer laser operating at 248 nm with an average laser pulse of ~25 ns was used, and a typical laser energy density at the target was ~ 1 J/cm^2. Therefore, the instantaneous power is roughly 40 MW/cm^2.* The high instantaneous power causes highly nonequilibrium evaporation of the target material. Despite the high power, it is still important for the laser energy to be absorbed by the target for ablation to occur. A photon wavelength of 248 nm corresponds to an energy of 5 eV. In principle, materials with a band gap of higher than 5 eV cannot absorb the radiation effectively. In practice, the polycrystallinity of the targets allow for sufficient absorption in materials with band gaps that are in slight excess of 5 eV. Therefore, single crystalline targets are not necessarily the best choice. Also, because of the high instantaneous power, higher-order optical processes are possible. In any case, ablation of materials with considerably larger band gaps, such as MgO and $MgAl_2O_4$, is difficult even with the higher energy densities feasible in our setup. It is also difficult to ablate metals with a plasma frequency higher than 5 eV, due to reflection of radiation. Furthermore, it is best to have materials with lower thermal conductivity because one would want the absorbed energy to be concentrated at the surface, for effective ablation. Powder pressed, polycrystalline targets are also desirable for lower thermal conductivity. All in all, polycrystalline ceramic targets are suitable for pulsed-laser deposition.

In this technique, the cation stoichiometry of the starting target material is very effectively transferred to the film [1]. However, the laser ablation process can reduce the target material, causing it to lose oxygen. This can be compensated by depositing films in an oxygen ambient to recover the stoichiometry. On the other hand, characteristic target reduction of oxides can be exploited in order to achieve thermodynamically unfavorable reduced phases. For example, the valence state of Ti in $LaTiO_3$ is 3+, but the most stable oxidation state of Ti is 4+. To make bulk $LaTiO_3$ crystals, annealing in a reducing H_2 ambient is often required. However, by making use of the (oxygen) reduction that occurs during laser ablation, $LaTiO_3$ (Ti^{3+}) films can be grown in a vacuum environment, containing no H_2, starting from a $La_2Ti_2O_7$ (Ti^{4+}) target. Conversely,

* The laser is typically operated at 1 to 10 Hz; so the average power is only 1 to 10 W/cm^2.

deposition in an ozone ambient can be used to achieve more oxidized phases that are not readily accessible in the bulk. This makes pulsed-laser deposition a very attractive research tool for achieving different and exotic stoichiometric phases of complex oxide thin films.

With silver paste, a single crystalline substrate is glued onto a heater that is loaded on-axis with the plume and roughly 8 cm from the target surface. The target is rotated during the deposition to ensure that it is evenly ablated.

A combination of *ex-situ* structural analytical techniques—atomic force microscopy, x-ray diffraction, and Rutherford backscattering spectrometry—is used to check for and determine suitable deposition conditions for different materials.

§ 2.2 Reflective high energy electron diffraction

Thin-film growth can be monitored by *in-situ* reflective high energy electron diffraction (RHEED). RHEED guns that can operate at relatively high deposition pressures have been readily incorporated into oxide thin-film growth techniques. Most of the films shown in this dissertation were grown without RHEED monitoring, except for a sample in Chapter 6. The RHEED gun was operated at 20 kV (wavelength of 0.086 Å) and ~20 A, and was aimed at the sample surface at grazing (~3^{o}) incidence. Grazing incidence keeps diffraction very surface sensitive, akin to diffraction of a two-dimensional specimen; furthermore, only the nearly elastically scattered electrons contribute to the formation of diffraction patterns. Roughening of the sample surface of just a few unit cells would completely destroy the diffraction pattern. In fact, roughening of the surface by just a single perovskite unit cell is sufficient to decrease the diffracted intensities substantially. By keeping track of a diffracted peak intensity as it evolves with deposition time, one can monitor the layer-by-layer growth exhibited by many (001) perovskite heterostructures. When a new layer begins to grow, the intensity is reduced, but it returns to a local maximum when the entire layer is completed. In this way, the exact thicknesses of the films can be precisely monitored *in-situ* when the growth mode is layer-by-layer. Islanding growth is characterized by an immediate drop in diffracted intensity. Step-flow growth is characterized by constant and high intensity as a function of time and therefore cannot be monitored by RHEED.

§ 2.3 Atomic force microscopy

Surface morphology was studied by atomic force microscopy (AFM). AFM images were taken on a Dimension 3100 atomic force microscope from Bruker (formerly Veeco Instruments) operating in tapping mode. The AFM piezoelectric scanner controls the position of the cantilever that contains a probe tip facing down toward the sample. The cantilever resonates mechanically in an up-and-down motion, scans the sample by making gentle tapping contact, and is deflected by the surface features of the sample. For

topographic images, Si tips of roughly 15 nm tip radii were used and tuned to oscillate with a root-mean-squared amplitude of 2.5 V at its resonance frequency, which is typically 300 kHz for the tips used in this study. Images were taken at an amplitude that is 5% lower than that at the resonance frequency. Once the AFM tip makes initial tapping contact with the sample, the drive amplitude was lowered by roughly 0.1 to 0.2 V to ensure that good tapping contact is maintained throughout the scan.

§ 2.4 Transmission electron microscopy

Transmission electron microscopy (TEM) gives real-space lattice fringe images, produced by the interference of an electron diffraction pattern. For thin-film samples, cross-sectional images are of interest. M-bond, an epoxy-phenolic resin, was used to glue two pieces of samples together on the film side. The specimen was then augmented with two more pieces of silicon on each side to make a cross-section of 3 mm, the diameter of most typical TEM holders. The M-bond needs to be cured at 150°C for at least one hour, and it becomes insoluble in acetone. The specimen was then cut in cross-section using a diamond-coated rotating saw to achieve rectangular pieces of 0.5 mm thickness faced at the cross section of the sample. Then it was cut into circular disks using a SiC slurry with an ultrasonic cutter. The circular disk is then dimpled with a 3 μm diamond slurry such that the typical thickness of the center of the specimen would be 10 μm and the edges would be roughly 100 to 150 μm. A 1 μm diamond slurry was used for the final polishing. For improved structural integrity, the specimen was glued onto a 50 μm thick copper grid before further thinning by ion milling. Electron transparency was obtained by Ar ion-milling in the Fischione ion mill operated at 5 kV and 6 mA at the National Center for Electron Microscopy, Lawrence Berkeley National Laboratory. High-resolution TEM was performed on the Philips CM300 field-emission gun microscope at an electron voltage of 300 kV. A double-tilt holder allows for the tilting of the sample to a specific zone axis. Phase contrast is attained by allowing multiple diffraction spots to pass through a fairly big objective aperture. The microscope projection lenses were used to magnify the image by 49 kx, and further magnification (~40 x) was achieved using a GIF CCD camera.

§ 2.5 Rutherford backscattering spectrometry

Rutherford backscattering spectrometry (RBS) allows for the determination of the stoichiometry and thickness of a single film or a heterostructure containing many layers of different compounds. In the measurement, a beam of helium ions is directed to the sample and is subsequently reflected due to scattering with atoms in the sample. By conservation of momentum and kinetic energy, the energy spectrum of the backscattered He ions collected at a specific angle provides elemental mass sensitivity as well as depth profiling. RBS measurements were performed by Dr. Kin Man Yu, Materials Sciences

Division, Lawrence Berkeley National Laboratory. The spectra were analyzed by RUMP software developed by Michael O. Thompson, Cornell University.

§ 2.6 X-ray diffraction

X-ray diffraction enables us to get information about a sample's real space structure by investigating its reciprocal space lattice. The reciprocal lattice of a perfectly crystalline thin film is a three-dimensional lattice of short rods that are negligibly thin in plane and slightly elongated perpendicular to the sample plane. The amount of out-of-plane elongation depends on the thickness of the film. The diffraction condition, i.e. condition for high diffracted intensity, is

$$\vec{Q} \equiv \frac{2\pi}{\lambda}\left(\vec{k}' - \vec{k}\right) = \vec{g}_{\mathrm{hkl}} \qquad \text{(Eqn. 2.1)}$$

where λ is the x-ray wavelength, $\boldsymbol{k}$ and $\boldsymbol{k'}$ are the incident and diffracted unit vectors, $\boldsymbol{g}_{\mathrm{hkl}}$ is a reciprocal lattice vector for the *hkl* reflection, and $\boldsymbol{Q}$ is commonly called the scattering vector.

In a diffractometer, diffraction peaks occur when the geometric condition of Eqn. 2.1 is satisfied, and the geometry of the reciprocal lattice can be determined; the scanning of appropriate diffraction angles—2θ, ω, ϕ, and ψ, as defined in Fig. 2.1—allows for the navigation of reciprocal space. It can be easily shown that for a 2θ scan with $\omega = 2\theta/2$ (= θ)[†] and constant ϕ and ψ, only the reciprocal lattice points orthogonal to the sample plane can be scanned, and thus only the out-of-plane interplanar spacings can be determined. While 2θ is directly related to the length of a vector in reciprocal space via Bragg's Law, all of the other angles are associated with its direction. When the diffraction condition is satisfied, we refer to the corresponding $2\theta_{\mathrm{hkl}}$ value as the Bragg angle of the *hkl* reflection. It can also be shown that performing ω scans at a Bragg angle corresponding to any out-of-plane reflection and constant ϕ and ψ yields the in-plane shape of reciprocal lattice "points." The in-plane intensity breadth of reflection spots can be used to describe the crystalline quality of epitaxial thin films.

It is often useful to get the positions of reciprocal lattice points that have both in-plane and out-of-plane components to determine in-plane interplanar spacings as well. It is convenient to define an angle δ, which is the angle between the normal of the sample plane and that of the crystal planes of interest,[‡] as shown in Fig. 2.2a, from which we get the following relationship

$$2\theta = 2(\omega + \delta)$$

[†] Any reference to θ should be thought of explicitly as 2θ/2, because 2θ (not θ) is the physically meaningful angle for diffraction.

[‡] The normal to the (*hkl*) plane is the reciprocal lattice vector $\boldsymbol{g}_{hkl}$.

The angle δ is not an independent angle. If we write $\boldsymbol{Q}$ in components parallel and perpendicular to the plane: $\boldsymbol{Q} = \boldsymbol{Q}_{||} + \boldsymbol{Q}_{\perp}$, for a given position in reciprocal space of arbitrary $\boldsymbol{Q}$,

$$\delta = tan^{-1}(Q_{\parallel}/Q_{\perp})$$

$$\theta = sin^{-1}\left(\frac{\lambda}{4\pi}\sqrt{Q_{\parallel}^2 + Q_{\perp}^2}\right)$$

for fixed ϕ and ψ. In a strained thin film, *a priori* one would know neither δ nor 2θ, so the relevant reflection spot can be easily missed with just a single one-dimensional scan. Two-dimensional maps of the reciprocal space can be attained by scanning over a range of ω and 2θ values, where ω determines the orientation of $\boldsymbol{Q}$ and 2θ determines the length of $\boldsymbol{Q}$. A schematic of such a map, commonly referred to as a reciprocal lattice map, is shown in Fig. 2.2b.

At a Bragg angle that contains both in-plane and out-of-plane reciprocal lattice components, a ϕ scan to can be performed to examine the in-plane crystalline symmetry of the thin films. As with an ω scan, the length of the scattering vector remains constant.

In this work, the following types of x-ray diffraction experiments are commonly employed: (1) 2θ scans with ω = 2θ/2, (2) ω scans at a particular $2\theta_{hkl}$, and (3) two-dimensional off-orthogonal 2θ-ω maps of regions in reciprocal space. All of these scans are performed at fixed ϕ and ψ. The diffraction experiments presented in this dissertation were taken on a Panalytical X'Pert MRD diffractometer. The radiation source was copper *K*-edge emission; a four-bounce Ge-crystal monochromator selects only the K_{α} radiation, which corresponds to a wavelength of 1.541 Å. For a standard reference in x-ray diffractrometry optics, see Chapter 6 of Ref. [2].

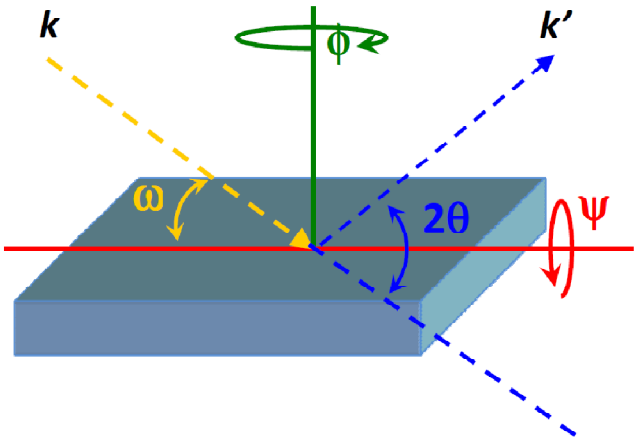

Figure 2.1. Schematic showing all of the relevant angles (2θ, ω, ϕ, and ψ) with respect to the sample for four-circle diffraction. *k* and *k'* are the wavevectors of the incoming and outgoing radiation.

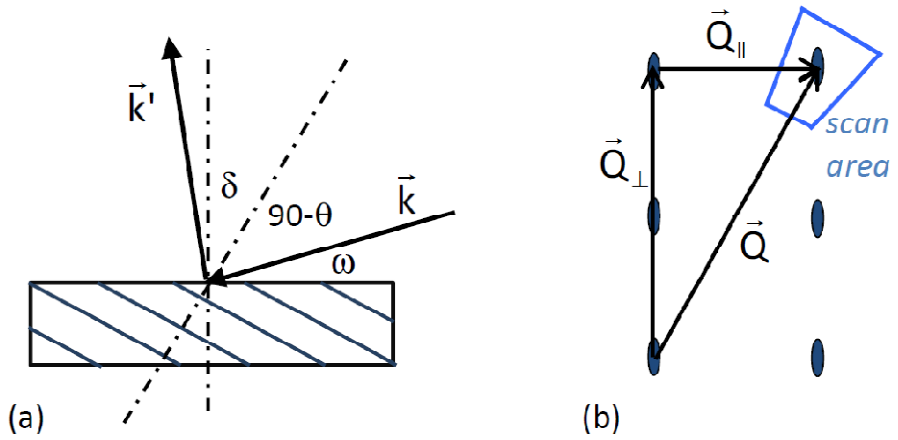

Figure 2.2. (a) Schematic of the x-ray alignment for a scan of a reflection spot with components parallel and perpendicular to the sample surface plane. The sample planes of interest are shown. ϕ and ψ are fixed. (b) Schematic of a two-dimensional map of reciprocal space by scanning a range of 2θ and ω values with ϕ and ψ fixed. The reciprocal lattice is represented by an array of cigar-shaped spots, typical for a thin-film material.

§ 2.7 SQUID magnetometry

Magnetometry with a superconducting quantum interference device (SQUID) from Quantum Design to detect the magnetic flux was used to measure the magnetic moments in samples. The magnetic moment is measured in units of *emu*, where one Bohr magneton $\mu_B = 9.27\times10^{-21}$ emu. Magnetization values were calculated by normalizing the measured moments by the volume of the sample. The thicknesses of the thin films were measured by Rutherford backscattering spectrometry, and their lateral dimensions were measured with a caliper.

A common measurement is the magnetization as a function of temperature. Typically, the temperature is swept from low to high. In the work of Chapter 5 the temperature is raised above the film's Curie temperature before it is cooled to the initial temperature of the scan. During this initial cool down prior to taking measurements, a magnetic field may (field cool) or may not (zero field cool) be applied.

Another common scan is magnetization versus applied field. Because any substrate invariably contributes at least a diamagnetic signal, a linear background needs to be subtracted from the magnetic moment versus field curves after the measurement.

The data on studies of thin-film magnetization in Chapter 5 were taken along the easy axis (plane) of each sample. The field applied in the SQUID magnetometer was always along the cylindrical sample area as a consequence of the geometry of the experimental setup. In order to achieve magnetization measurements along various crystal directions of a single sample, the sample itself was loaded in different orientations with respect to the cylindrical sample area.

§ 2.8 Electrical Transport

Electrical transport measurements were made on a Physical Property Measurement System (PPMS) from Quantum Design. Four-point probe measurements of single-layer films were performed in the van der Pauw sheet resistance and Hall geometries, as shown in Figure 2.3. In the sheet resistance geometry, resistance R_{VA} is determined by sourcing the current through leads 1 and 2, and measuring the voltage across leads 3 and 4, as shown in Figure 2.3. Similar definitions of the other resistance values, i.e. R_{VB} as well as R_{HA} and R_{HB} in the Hall geometry, are also shown in Figure 2.3. The sheet resistance R_S is determined by solving the transcendental equation [3]:

$$exp\left(-\frac{\pi R_{VA}}{R_S}\right) + exp\left(-\frac{\pi R_{VB}}{R_S}\right) = 1$$

The implicit assumption is that the sample conductivity is isotropic. If the thickness d of the conducting layer is known, e.g. from RBS data, the resistivity ρ can be calculated:

$$\rho = R_S d$$

Hall effect measurements can decouple the contributions of carrier concentration and mobility in the measured resistivity. In a Hall bar geometry with a magnetic field applied out of plane, the Hall voltage is measured across the bar (transverse) while an electric current is sourced along the bar (longitudinal). However, in the van der Pauw geometry, there is no geometric confinement that explicitly distinguishes transverse voltage from longitudinal voltage. Therefore, any longitudinal voltage component must be subtracted from the measured voltage, which can be done by measuring both R_{HA} and R_{HB}. The Hall resistance is given by [3,4]

$$R_{Hall} = \frac{R_{HA} - R_{HB}}{2}$$

A Hall measurement can decouple the contributions of carrier concentration (n) and mobility (μ) to conductivity ($1/\rho$), by using the relationships:

$$R_{Hall} = -\frac{B}{ned}$$

$$\rho = \frac{1}{\sigma} = \frac{1}{ne\mu}$$

where B is the magnetic field and e is the elementary charge.

Hall resistance values are measured for different fields and a slope is then calculated: $m = \Delta R_{Hall}/\Delta B$. The convention used in these equations is negative (positive) slope m for carrier electrons (holes). The mobility and sheet carrier concentration ($n_S = nd$) can be deduced even without knowing the thickness of the conductive film:

$$n_S = \frac{1}{e|m|}$$

$$\mu = \frac{|m|}{R_S}$$

For conductive interfaces, in which the exact thicknesses may not be known or readily measured, it is customary to use sheet carrier concentration and sheet resistance rather than carrier concentration and resistivity.

With an applied magnetic field, the resistivity of the sample may change, and the magnetoresistance (MR) can be measured

$$MR(H) = \frac{R_S(H) - R_S(0)}{R_S(0)}$$

where $H=B/\mu_0$ and μ_0 is the permittivity of free space. The MR is measured at constant temperature. In principle, the magnetic field can be applied at any orientation with respect to the sample. In practice within a standard Quantum Design PPMS setup, the field is always applied along the long axis of the sample space. The sample can be mounted onto a horizontal rotator which then allows for the rotation of a sample from being fully in-plane to fully out-of-plane. For the sample holders used, in-plane rotation must be done manually by physically changing how the sample is loaded.

Sheet resistance, Hall resistance, and MR measurements were heavily used in this dissertation to study the transport behavior of oxide heterostructures.

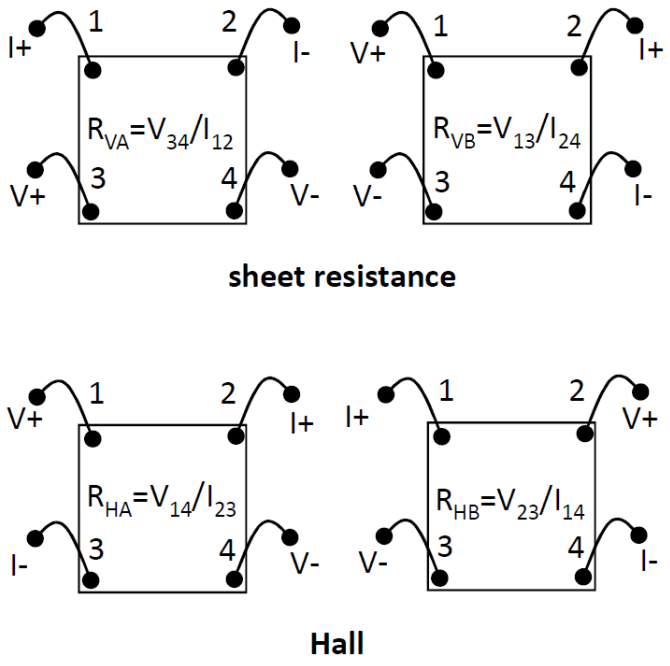

Figure 2.3. Van der Pauw sheet resistance (top) and Hall (bottom) geometries used in the electrical transport measurements.

Chapter 3
Basic Aspects of Correlated Perovskite Oxides

The Perovskite Structure: Atomic and Electronic

3.1 The cubic perovskite 21
3.2 The distorted perovskite 25

Correlated Electron Systems

3.3 One-electron approximation 27
3.4. Failure of the one-electron approximation 29
3.5 The Hubbard model 30
3.6 A comment on the classification of correlated insulators 32
3.7 Magnetism in correlated oxides 33
3.7.1 Antiferromagnetic coupling from superexchange 33
3.7.2 Ferromagnetic coupling from superexchange 34

The Perovskite Structure: Atomic and Electronic

One of the underlying themes that resonates throughout this dissertation is how the perturbations in the atomic structure of perovskite oxides can profoundly affect their electronic structures, which in turn govern the electronic properties we can measure. This section discusses the intimate relationship between the atomic and electronic structures of these materials from a chemical bonding perspective. Noncubic lattice distortions are treated perturbatively, and the cubic crystal structure is used as a reference.

§ 3.1 The cubic perovskite

A conventional cubic perovskite ABO_3 has a simple cubic structure with a five-atom basis. It can be most readily visualized as an oxygen octahedron, with the oxygen atoms on the faces of the cube surrounding the center B atom; the 12-coordinated A atoms occupy positions at the corners of the cube, as shown in Fig. 3.1. The structure of the perovskite is defined mainly by the $BO_{6/2}$ octahedron.[*†] In an extended solid, A atoms fill in the spaces between repeating $BO_{6/2}$ octahedra. In this dissertation, we will consider compounds in which alkaline-earth and rare-earth metals occupy the A sites and 3*d* transition metals and Al occupy the B sites.

Qualitative aspects of the electronic band structure of a perovskite material can be understood using a chemical bonding approach. Let us first consider the general case of the formation of a chemical bond between a metal atom and an oxygen atom. Two atomic orbitals, one from each atom, combine to form two molecular orbitals—a lower-energy bonding orbital with character of mainly the oxygen orbital and a higher-energy antibonding orbital with character of mainly the metal orbital, as shown in Fig. 3.2. Molecular orbitals are treated as linear combinations of atomic orbitals. In the limit of a perfectly ionic cation-anion bond, it can be thought of as the metal donating electrons to the oxygen. We now have a simplified, but conceptually correct, description of the valence electron atomic orbitals, which are perturbed by the act of bonding. As a result of this perturbation, the oxygen-like bonding molecular orbital decreases in energy at the expense of the transition metal-like antibonding molecular orbital, which increases in energy. If the chemical bonding is stronger, perturbations to the atomic orbitals consequently become larger, and the separation between the bonding and antibonding levels also increases—as is schematically represented in the right panel of Fig. 3.2.

In a nearly ionic bond, the valence *s* electrons from both the A and B atoms are readily donated to the oxygen atoms. Consequently, the *s* electronic levels from A and B have high energy, and in a solid, they form high-lying empty conduction bands, which do not directly affect the ground-state properties of the material. In transition-metal

[*] ReO_3 and WO_3 are examples of perovskites without A-site atoms.

[†] The notation $BO_{6/2}$ is used to emphasize that each oxygen atom is corner-shared by 2 octahedra.

perovskite oxides, the electronic bands that are closest to the Fermi level originate from the *d* electrons in the B transition metal, which interact with *p* electrons of the neighboring oxygen atoms. For simplicity, we disregard the *s* orbitals of the oxygen atoms because the omission does not affect our conceptual description.

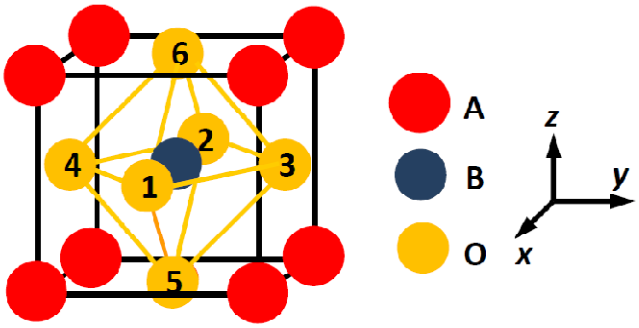

Figure 3.1. The perovksite unit cell.

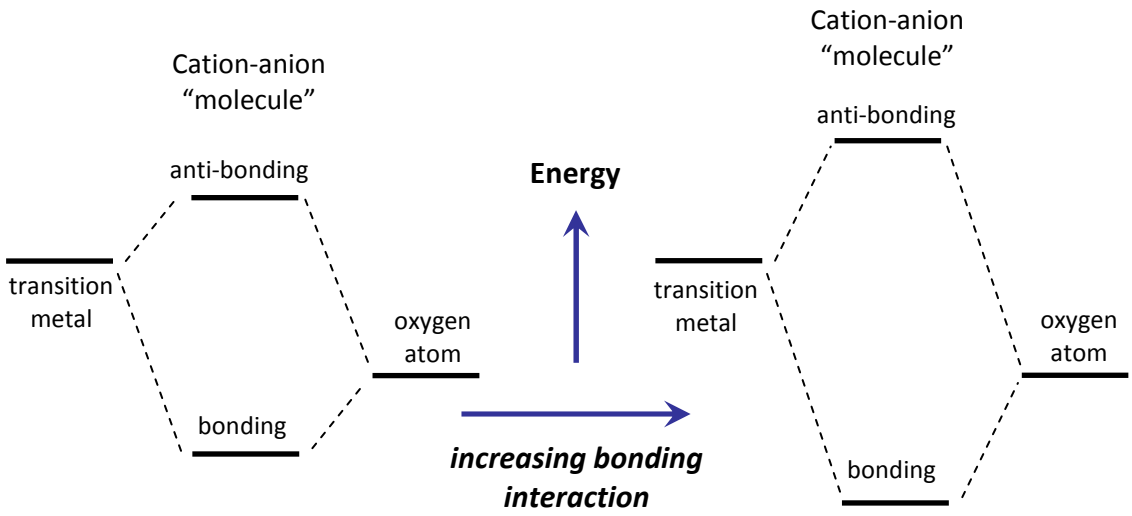

Figure 3.2. Schematic of two atomic orbitals forming two molecular orbitals: one bonding and one antibonding. The amount of separation between the two levels depends on the degree of bonding interaction.

Molecular orbitals of a $BO_{6/2}$ octahedron provides the best physical picture of the bonding in perovskites. The *p* orbitals of the oxygen atoms and the *d* orbitals of the transition metal will be used as the basis set. The oxygen *p* orbitals are three-fold degenerate: p_x, p_y, and p_z. The transition-metal *d* orbitals are five-fold degenerate: *xy*, *xz*, *yz*, x^2-y^2, and z^2 (or more precisely $3z^2$-r^2). The shapes of these atomic orbitals are shown in Figs. 3.3 and 3.4.

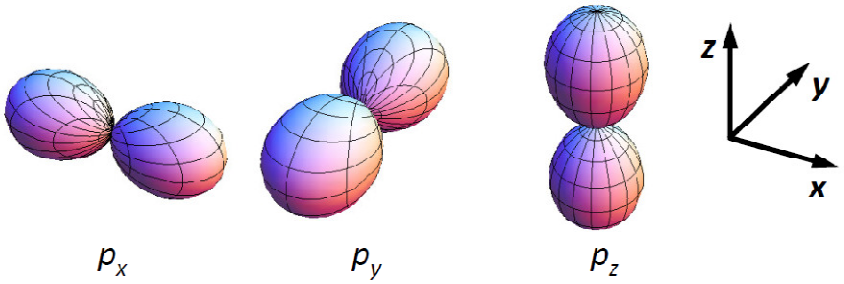

Figure 3.3. Shapes of the three-fold degenerate *p* orbitals.

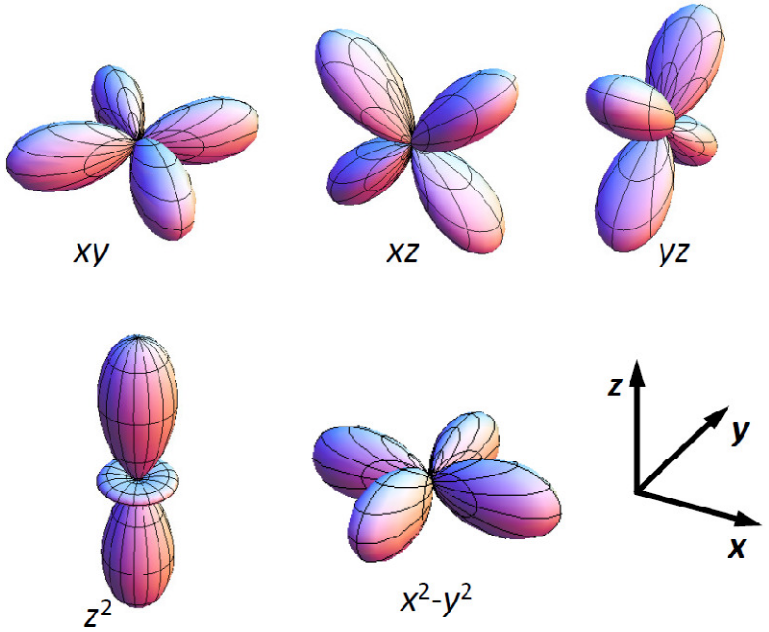

Figure 3.4. Shapes of the five-fold degenerate *d* orbitals.

The B-O bond can be envisaged as the overlap between atomic orbitals.[‡] There is direct overlap between the x^2-y^2 orbital of B and the p_x orbitals of O1, O2 as well as p_y of O3, and O4 (the oxygen sites O1, O2, … O6 are as defined in Fig. 3.1). Likewise there is direct overlap between the z^2 orbitals and p_z orbitals of O5 and O6. This strong orbital overlap is referred to as σ bonding and signifies a large perturbation to the atomic orbitals. An example is shown in Fig. 3.5a. The remaining *d* orbitals in the B transition metal also overlap with the other oxygen *p* orbitals, e.g. *xy* with p_y of O1 and O2, p_x of

[‡] Overlap here is used loosely to refer to the bonding matrix element in a tight-binding approach.

O3 and O4, and similarly for *xz* and *yz*. However, the orbital overlap in these cases is more indirect, and therefore the bonding is weaker; this is referred to as π bonding and atomic orbitals are less perturbed compared to the case of σ bonding. An example is shown in Fig. 3.5b. Compared to π bonding, the stronger σ bonding creates lower-lying bonding orbitals and higher-lying antibonding orbitals. In summary, the bands near the Fermi level of perovskites can be described by the molecular orbitals schematically shown in Fig. 3.6. The key feature is that the five-fold degenerate atomic *d* orbitals are split into three-fold π antibonding (π*) and two-fold σ antibonding (σ*) orbitals, with group theory symmetry designations of t_{2g} and e_g, respectively. The energy between the σ* and π* states is commonly known as crystal field splitting. Group theory notations are used primarily in Chapters 4 and 5, and they refer to the symmetry of the *d*-like bands at the Γ point in k-space.

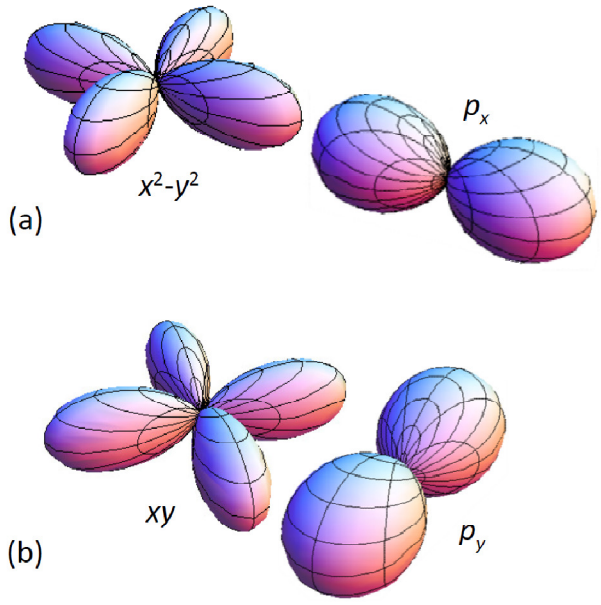

Figure 3.5. Schematics of orbital overlap in the case of (a) σ bonding formed by x^2-y^2 of the B transition metal and p_x of a neighboring oxygen and (b) π bonding formed by *xy* of the B and p_y of a neighboring oxygen. There is greater orbital overlap in the case of σ bonding.

In our basis set of a $BO_{6/2}$ octahedron, the π and σ bonding orbitals are 6- and 3-fold degenerate, respectively. But note that we neglected some orbitals in our basis set—for example, the oxygen 2*s*. In any case, since the bonding levels of the transition-metal oxides are typically completely filled, these levels do not directly control their properties, and we will not dwell on the details. The antibonding *d*-like levels are the ones that determine the properties of transition-metal perovskite oxides, and this simplified discussion gives us a good description of those levels. In extended solids, instead of discrete molecular orbital levels, electronic bands of finite energy bandwidths are

formed, and orbitals become Bloch waves. The formation of energy bands from a tight-binding approach is presented in Section 3.3. The characteristics of the bands in a solid are closely related to the molecular orbitals from which they originate. In many parts of this work, the bands arising from such antibonding molecular orbitals will be *loosely* referred to as transition-metal *d* bands.

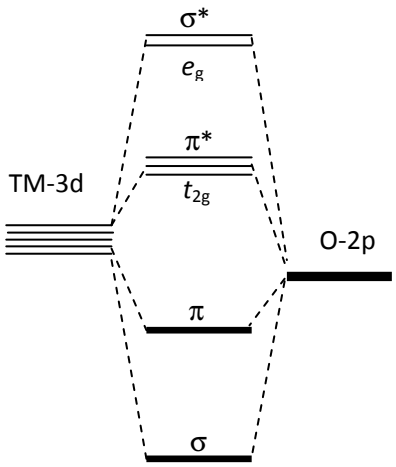

Figure 3.6. Schematic of molecular orbitals formed by the *d* orbitals of the transition metal (TM) and the *p* orbitals of neighboring oxygen atoms. The antibonding levels, t_{2g} and e_g (mainly *d*-like), are three- and two-fold degenerate respectively.

§ 3.2 The distorted perovskite

Now that we have considered the origins of the electronic levels of interest, the transition-metal σ* and π* bands, we are in a position to consider how these levels change as the crystal lattice structure is perturbed. Most perovskite oxides are in fact noncubic and have reduced symmetry—tetragonal, orthorhombic, rhombohedral, or monoclinic. However, in most systems the deviation from cubic symmetry is small; therefore, the materials can be treated using a cubic reference and then incorporating the appropriate distortion as a perturbation to the reference structure.

Structural distortions in these materials arise from accommodation of internal lattice strain; it comes about because the A-O and B-O equilibrium bond lengths are not a perfect fit to form a perfectly cubic structure.[§] Internal lattice strain is intrinsic to the crystal [1], and should not be confused with substrate-induced heteroepitaxial strain. From Fig. 3.1, we can see that a structure with B-O-B bond angles that are exactly 180°

[§] The equilibrium A-O bond length refers to the bond length between an A cation and an oxygen anion only, and similarly for B-O. There are a variety of means to measure such a quantity (see Ref. [1]).

must satisfy the following relationship between equilibrium A-O and B-O bond lengths ($L_{A\text{-}O}$ and $L_{B\text{-}O}$ respectively):

$$L_{A-O} = \sqrt{2}L_{B-O}$$

The tolerance factor (TF) is defined as

$$TF \equiv L_{A-O}/\sqrt{2}L_{B-O}$$

As long as TF ≠ 1, there is some internal lattice strain that needs to be accommodated by lattice distortions. For example, consider TF < 1 which signifies that the $L_{B\text{-}O}$ is larger than its "ideal" value, as is often the case for transition-metal perovskites. We can visualize that the collective rotation of all octahedra about the [001] axis can relieve the in-plane lattice strain: Fig. 3.7 shows the effect of octahedra rotation on the (002) BO_2 plane. This rotation is commonly accompanied by an elongation of the [001] axis, and a tetragonal structure is formed. The (002) AO plane remains unchanged. In the rotated structure depicted in Fig. 3.7b, adjacent B atoms are closer than a distance of $2L_{B\text{-}O} = \sqrt{2}\ L_{A\text{-}O}$; hence, the distortion allows for the accommodation of a B-O bond that would have been otherwise too long. Such collective octahedra rotation can occur along other crystalline axes—for example, [110] and [111]—leading to orthorhombic and rhombohedral distortions. See Ref. [2] for details.

Such a structural distortion alters the electronic structure. Because the B-O-B bond angles now are not exactly 180°, the bonding orbitals do not overlap from one octahedron to the next as much. Therefore, owing to the distortion there is a reduction of transition-metal electronic bandwidth as compared to the cubic reference. The further the angle θ, as defined in Fig. 3.7b, strays from 180°, the narrower the bands become. However, if the bond lengths are shortened, bonding and electronic bandwidth are increased.

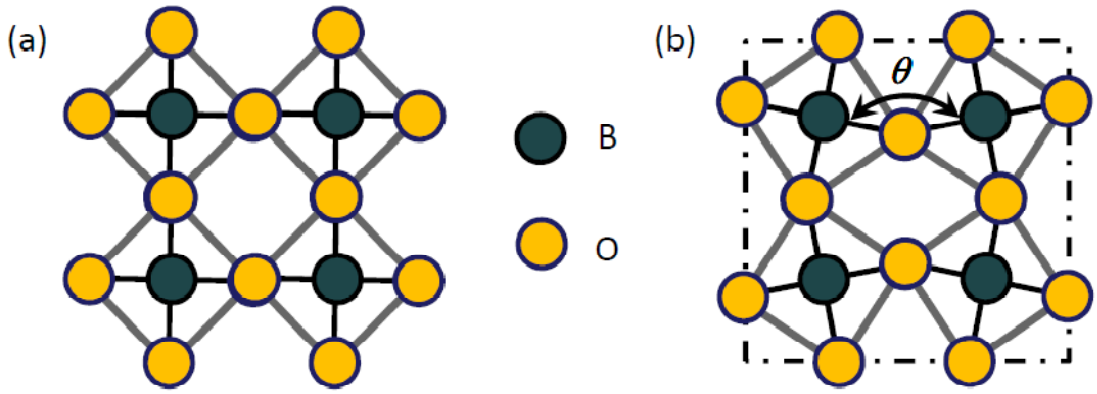

Figure 3.7. Schematic of the (002) BO_2 plane (a) before and (b) after a collective octahedra rotation about the [001] direction. Adapted from Ref. [2].

Correlated Electron Systems

This section introduces correlations in materials by first explaining how uncorrelated materials can be modeled using an one-electron band picture, then pointing out why the model fails for certain materials, and finally describing how strong correlations in electronic systems are treated. Correlation in oxides and their classifications will be described. The section ends with a discussion on superexchange magnetic interaction, which is typically in 3*d* transition-metal oxides.

§ 3.3 One-electron approximation

A central task of condensed matter and materials physics is to describe how electrons behave in solids, because the electron eigenstates and eigenenergies determine many properties of a material. The nearly free electron picture provides the simplest description of solids: the valence electrons are dispersed among a background of immobile ion cores.[**] When atoms bond to form solids, the discrete electronic levels of the valence electrons are perturbed and create continuous bands. Valence electrons in the Fermi sea have kinetic energy. The electrons also have potential energy, derived from electrostatic interactions with ion cores and other electrons. Electron interaction with collective lattice displacement modes, phonons, can alter the energy of electronic eigenstates; such an interaction may be either electrostatic or mechanical. Therefore, using the Born-Oppenheimer approximation and neglecting the energy of the immobile ion cores, we end up with the following Hamiltonian for a crystal:

$$H = \sum_i \frac{p_i^2}{2m} + \frac{1}{2}\sum_{i,i'} \frac{e^2}{4\pi\varepsilon_0 |r_i - r_{i'}|} - \sum_{i,j} \frac{Z_j e^2}{4\pi\varepsilon_0 |r_i - R_{0j}|} + H_{e-ph}(r_i, \delta R_j)$$

(Eqn. 3.1)

where i and i' index electrons participating in bonding
j indexes ions,
p is the electron momentum,
m is the electron mass,
e the electron charge,
r the electron position,
Z the atomic number,
R_0 the equilibrium position of the ion,
and δR its displacement.

[**] Although the tight-binding approach was used to discuss the electronic structure of perovskite oxides in Section 3.1, starting from the nearly free electron model paints a more vivid comparison and contrast between uncorrelated and correlated materials. Tight-binding is covered in later.

and *all* of the valence electrons, in principle, must be counted. The first term is the kinetic energy; second, electron-electron repulsion; third, electron-ion attraction; and last, electron-phonon interaction. Albeit harmless-looking, diagonalizing this Hamiltonian is, in practical terms, impossible. The summation of each term is over all ions and bonding electrons, amounting to ~10^{23} for a macroscopic sample.

A model is only as good as the insight it gives us. Having the correct but insoluble many-body Hamiltonian is of no use to us. The task is to obtain a tractable model Hamiltonian. The one-electron approximation is an extreme simplification. It implies that the electronic dispersion of the system can be adequately modeled by considering how one test electron behaves in a mean-field potential V(*r*), which lumps together all of the potential energy terms in Eqn. 3.1. By assuming that all bonding electrons will behave as the test electron does, we need not perform the cumbersome summations in Eqn. 3.1. In crystalline materials, the ionic cores constitute a periodic potential; therefore, lattice periodicity is imposed on V(*r*). We will ignore the electron-phonon interaction for now. The Schrödinger equation for a crystal becomes

$$H^*\psi_n = \left[\frac{p^2}{2m} + V(r)\right]\psi_n = E_n\psi_n$$

(Eqn. 3.2)

where H* is the one-electron Hamiltonian, and ψ_n and E_n are the *n*th one-electron eigenstate and eigenenergy, respectively. The single-particle Hamiltonian approximated from the many-body system not only is tractable, but also has been used since the mid-20th century to successfully predict the electronic properties of a wide range of materials, and to classify them as metals, semimetals, semiconductors, and insulators. The interested reader is referred to several exemplary references [3-6].

Another approach to band theory that likewise neglects correlations in the many-body problem is the tight-binding model. Instead of starting from a plane wave basis as in the free-electron approach, the basis set is comprised of atomic orbitals. Tight-binding is in the spirit of the discussion of Section 3.1. The orbitals are linked by chemical bonding expressed through an overlap (also called transfer or hopping) integral *t*. A tight-binding Hamiltonian can be written in reference to real space sites *i* and *j*: [5]

$$H_{TB} = -\sum_{i,j} t_{ij}\left(c_i^\dagger c_j + c_j^\dagger c_i\right)$$

(Eqn. 3.3)

where t_{ij} is the transfer integral between an orbital on site *i* and one on site *j*, and c_i^+ and c_i are electron creation and annihilation operators of an orbital on site *i*. Let us consider the case of a one-dimensional chain of *N* sites. We will assume only nearest-neighbor overlap: $t_{ij} = t$ if *i* and *j* are nearest-neighbor sites and $t_{ij} = 0$ otherwise. The electron operators can be written in Fourier (*k*) space as

$$c_i^\dagger = \frac{1}{\sqrt{N}}\sum_k c_k^\dagger exp\left(i\vec{k}\cdot\vec{R}_i\right)$$

$$c_j = \frac{1}{\sqrt{N}} \sum_{k'} c_{k'} exp\left(-i\vec{k}' \cdot \vec{R}_j\right)$$

where $\boldsymbol{R}_i$ is the real-space coordinates of site i and $\vec{R}_i - \vec{R}_j = \vec{a}$ for nearest neighbor sites i and j, where $|\vec{a}|$ is the nearest-neighbor site-to-site distance or the lattice constant. There are N nearest-neighbor sites.[††] All $k \neq k'$ ($-\pi/a \leq k, k' \leq \pi/a$) terms in $c_i^+ c_j$ are equal to zero. We get

$$\vec{k} \cdot \left(\vec{R}_i - \vec{R}_j\right) = ka$$

We also can use the following relationships

$$c_k^\dagger c_k = n_k$$

$$cos(ka) = \frac{1}{2}\left[exp(ika) + exp(-ika)\right]$$

where n_k is the number operator of a state with momentum k. We finally see that the tight-binding Hamiltonian, starting with atomic orbitals, does indeed lead to eigenstates $|k\rangle$ within the first Brillouin zone which are dispersed in energy

$$H_{TB} = -\sum_k 2tcos(ka)n_k \qquad \text{(Eqn. 3.4)}$$

Eqn. 3.4 tells us that the electronic bandwidth resulting from nearest-neighbor bonding is $4t$. The tight-binding Hamiltonian H_{TB} is a good starting point for describing transition-metal *d* states, because they are generally less delocalized eigenstates than those of *sp*-valent materials. The H_{TB} as expressed in Eqn. 3.3 will be used heavily because of its physical, real-space appeal.

§ 3.4 Failure of the one-electron approximation

A priori we would not know whether the overly simplistic one-electron Hamiltonian H* or H_{TB} can capture the properties of real materials. Perhaps we should not be surprised that the model may not hold for certain materials; rather, we should wonder how it can be valid for *any* materials system. Its versatility in capturing the electronic behavior of many *sp*-valent materials justifies the approximation of a collection of quasi-independent particles residing in some type of mean field. We understand such systems to be weakly correlated or uncorrelated.

From Eqns. 3.2 and 3.4, we see that in a one-electron picture, the electronic states do not explicitly depend on the number of electrons in the system; therefore inherent to the approximation, electron-electron interactions cannot be treated

[††] In principle, for the case of a linear chain, there are N-1 nearest neighbor sites, but with periodic boundary conditions, there are N.

appropriately with this over-simplified model. Furthermore, the mean-field approximation becomes invalid when interactions, including electron-electron and electron-phonon coupling, are strong and short-ranged. Such systems are strongly correlated. For example, a similar mean-field approach has been effectively used to describe superconductivity in conventional superconductors, in which Cooper pairs span a large spatial extent. The model, however, fails to describe high-T_c ceramic oxide superconductors, in which Cooper pairs are much smaller—on the order of atomic spacings. Transition-metal oxides, with *d*-valent cations, exhibit strong correlations; hence, Eqns. 3.2 and 3.4 do not adequately model the electronic properties of this class of materials.

§ 3.5 The Hubbard model

Mott was the first to eloquently articulate the need to formulate a new framework to explain the electronic behavior of transition-metal oxides [7], pointing out that the one-electron, independent-particle theory would predict insulating NiO to be metallic. NiO is a nearly ionic compound with Ni^{2+} and O^{2-} ions. Mott speculated that electrical conduction in NiO would require the formation of Ni^{+} and Ni^{3+} cations by the following "reaction":

$$2Ni^{2+} \rightarrow Ni^{+} + Ni^{3+}$$

The reaction needs energy input; thus the ground state of NiO is insulating. The inability of electrons to move freely in NiO is a manifestation of short-ranged electron-electron repulsion, a form of electronic correlation. This argument remains as good of a conceptual explanation today as it was when Mott proposed it in 1949 [7].

Owing to correlations in some materials as exemplified by NiO, bonding electrons may not be as free as is suggested by the one-electron Hamiltonian H* or H_{TB}. Although Eqns. 3.2 and 3.3 are not valid in describing, even qualitatively, transition-metal oxides, we cannot automatically retreat to Eqn. 3.1 since it is not solvable. The approach taken by Hubbard is to add a term that represents strong electron correlation to the Hamiltonian [4,5]:

$$H' = -\sum_{i,j,\sigma} t_{ij}\left(c_{i\sigma}^{\dagger}c_{j\sigma} + c_{j\sigma}^{\dagger}c_{i\sigma}\right) + \sum_{i} U_i n_{i\uparrow} n_{i\downarrow} \qquad \text{(Eqn. 3.5)}$$

where i indexes bonding orbitals with strong correlation, $n_{i\sigma}$ is the electron number operator of orbital i and spin σ, and U_i is the on-site potential associated with the ith orbital. The tight-binding model is appropriate as a starting point because the 3*d* states of transition-metal oxides are expected to be fairly localized. In the Hubbard model (Eqn. 3.5), there is an energy cost of U for both spin-up and spin-down electrons to be in the same orbital. In contrast, the one-electron picture assumes spin degeneracy, whereby electrons of both spins can occupy the eigenstates of the same spatial component

simultaneously. Consequently, on-site repulsion in transition-metal oxides often results in moments, magnetic interactions, and long-range magnetic order—a topic to be covered in Section 3.7.

Electron-electron repulsion splits the spin degeneracy of levels, resulting in the formation of lower and upper Hubbard bands (LHB and UHB) separated by the potential energy U that needs to be overcome for electrical conduction. Encapsulated in H_{TB} is the net electron kinetic energy gained as result of the condensation of atoms into a solid with a periodic lattice. Kinetic energy can be represented by electronic bandwidth (B). From Eqn. 3.4, $B = 4t$. If the kinetic energy overwhelms the on-site potential energy, i.e. $B > U$, there is overlap between the LHB and UHB (Fig. 3.8), and the material is a correlated metal. Conversely if $U > B$, there is no overlap, and the material is a Mott insulator. For Mott insulators, the gap is approximately $U - B$. We see that correlations can, but do not necessarily, localize electrons of would-be metallic systems. Furthermore, the Hubbard Hamiltonian should not be viewed as the perfect model for correlated insulators; it is simply the best we have at the present. There is no definite way to determine U, and computational results can be entirely (pre)determined by the initial input value of U. In describing the Hubbard model, Marder says in his textbook that "there is no better illustration of the difficulties involved in progressing systematically beyond the one-electron pictures of solids." [4]

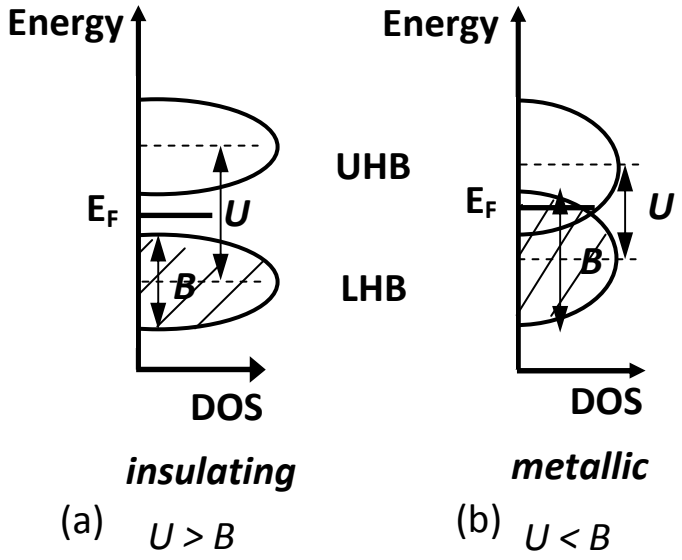

Figure 3.8. Schematic density of states (DOS) plots of (a) a Mott insulator with a gap between the LHB and UHB and (b) a correlated metal with band overlap. The filled states are shaded.

§ 3.6 A comment on the classification of correlated insulators

As noted previously, the electrical conduction in transition-metal oxides can be envisaged as the flow of an electron from a cation to a neighboring cation. For an arbitrary cation of oxidation state ν+ ($M^{\nu+}$), the reaction responsible for conduction is

$$2M^{\nu+} \rightarrow M^{(\nu-1)+} + M^{(\nu+1)+}$$

Energy is required for the ionization of $M^{\nu+}$ to a higher oxidation state, but then upon getting an extra electron, a neighboring cation lowers its energy. Finally, the extra electron at the $M^{(\nu-1)+}$ site and the hole at the $M^{(\nu+1)+}$ site are bound by the Coulomb interaction. Therefore, the energy U required for excitation from the LHB to the UHB can be approximated as [8]

$$U = I_v - EA_v - \frac{e^2}{4\pi\varepsilon_0 r}$$

where I_v and EA_v are the ionization energy and electron affinity of $M^{\nu+}$ respectively, r is the distance between nearest-neighbor transition-metal cations, and $-e^2/4\pi\varepsilon_0 r$ is the electron-hole Coulomb attraction energy.

Zaanen *et al*. further classified correlated insulators into two types: Mott-Hubbard insulators and charge-transfer insulators [9]. Conduction can be visualized in another way—electrons moving from oxygen anions to transition-metal cations, i.e.

$$M^{\nu+} + O^{2-} \rightarrow M^{(\nu-1)+} + O^{-}$$

The excitation energy here is

$$\Delta = I_O - EA_v - \frac{e^2}{4\pi\varepsilon_0 r'}$$

where Δ is the charge-transfer energy, I_O is the ionization energy of O^{2-}, and r' is the nearest-neighbor anion-cation distance. If $B < U < \Delta$, the material is a Mott-Hubbard insulator. If $B < \Delta < U$, the material is a charge-transfer insulator. The charge-transfer gap is approximately $\Delta - B$.

Such a classification is somewhat artificial, as it assumes the perfect ionic limit. Bonds between transition-metal and oxygen atoms always exhibit a degree of covalency, so the relevant eigenstates of the solid must be partly transition-metal 3*d* and partly oxygen 2*p* in character. From the categorization of perovskite oxides tabulated by Arima *et al.* [10], the apparent distinguishing factor between Mott-Hubbard and charge-transfer insulators is the degree of hybridization of the highest occupied state. Insulating compounds with electrons occupying e_g states are more charge-transfer-like, whereas insulator compounds with only t_{2g} electrons are more Mott-Hubbard-like.

The term "Mott insulator," without distinction between Mott-Hubbard and charge-transfer insulator, will be used throughout the dissertation.

§ 3.7 Magnetism in correlated oxides

As was shown Eqn. 3.5, an on-site potential naturally favors unpaired electrons. If there is a mechanism for exchange coupling among the spins of the unpaired electrons of different sites, then long-range order is possible in complex oxides. The fact that many 3*d* transition-metal oxides do exhibit a disordered paramagnetic state at high temperatures and magnetic ordering at low temperatures further justifies using the Hubbard model as a baseline to describe these materials. The issue of magnetic ordering is particularly important in Chapter 5.

It turns out the relevant magnetic interaction between adjacent transition-metal cations in oxides is made possible by bonding with the oxygen anions; this is known as superexchange. The concept of superexchange as we understand it today can be traced back to the Kramers's idea of an exchange mechanism between moments mediated by nonmagnetic atoms, and in the case of the oxides, the nonmagnetic mediators of magnetism are the oxygen anions [11]. Anderson formulated Kramer's concepts further, made predictions on the sign of the superexchange interaction for some model cases, and distinguished the superexchange effects in MnO for 90^{o} and 180^{o} Mn-O-Mn bonds [12]. The language of orbitals and hybridization were introduced by Goodenough [13,14] and Kanamori [15] who made predictions for the sign and strength of the exchange interactions for a variety of transition-metal perovskites. The generalizations that they made are referred to as the Goodenough-Kanamori rules. The discussion of magnetic ordering in oxides herein and throughout this dissertation will be largely based on their work, as there has not yet been a more accurate or physically satisfying model proposed since to describe the magnetism in transition-metal oxides. Goodenough's text, printed in 1963, still remains the best and most physically transparent monograph on the subject [16].

3.7.1 Antiferromagnetic coupling from superexchange

Let us start with the simplest example of a two-site system with one orbital and one electron in each site. The two orbitals are connected by a hopping term *t*. For transition-metal oxides, *t* may refer to 3*d*/2*p* σ or π bonding. The question is whether the spins of the two electrons are coupled. A calculation of the exchange interaction of this situation starting from the Hubbard Hamiltonian (*t*-*J* model) can be found elsewhere [17]. A qualitative description is presented here. By studying the Hubbard Hamiltonian H', we see the system can lower its energy by the allowing electrons to hop from one site to another. Schematically shown in Fig. 3.9, if the relative spin orientation is antiparallel, the energy cost will be the on-site potential *U*, and if the relative spin orientation is parallel the energy cost will be associated with disobeying the Pauli exclusion principle. For relevant energy scales of solids, the Pauli exclusion principle must always be obeyed; therefore, ferromagnetic alignment is not possible in this situation. Because of the energy penalty *U*, hopping of electrons that are aligned antiparallel must be transient (or

virtual). To express magnetic interaction, we would like to attain an exchange Hamiltonian of the form

$$H_{ex} = J\vec{S}_1 \cdot \vec{S}_2$$

For $t \ll U$, it can be shown that antiparallel moment alignment is the lowest energy state, and the antiferromagnetic exchange energy is given by [17]

$$J = \frac{2t^2}{U}$$

Here, a positive J signifies antiferromagnetic coupling. We need t to be non-negligible to allow for exchange interaction through chemical bonding; however, t cannot be too large as to destabilize the Mott insulating state. For $t \gg U$, it can be shown that the diamagnetic, metallic state has the lowest energy—as expected for uncorrelated or weakly correlated materials [17].

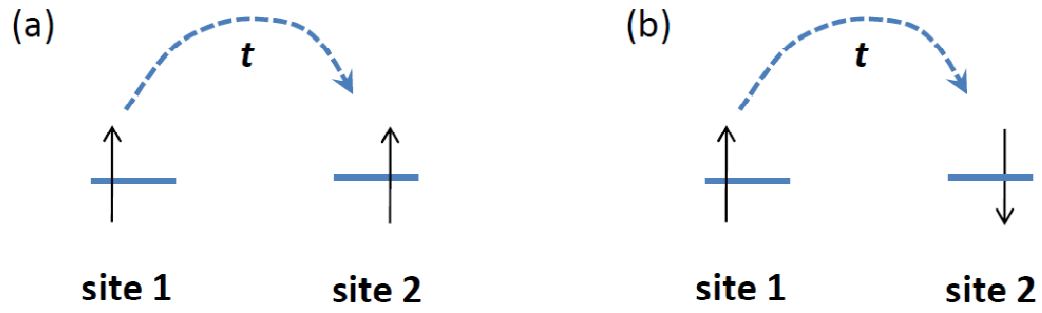

Figure 3.9. Schematics of the transient hopping with amplitude t in a two-site system with one orbital and one electron per site. The hopping in the case of (a) parallel moment alignment incurs an energy penalty associated with violating the Pauli exclusion principle, while in the case of (b) antiparallel moment alignment incurs a energy penalty of the on-site potential U.

3.7.2 Ferromagnetic coupling from superexchange

The Hamiltonian H′ in Eqn. 3.5 is actually more suited for a system that contains only one orbital per site. In considering multiorbital sites, we must include a term to account for the propensity of each site to maximize its total spin momentum. We can call this added energy term the on-site Hund energy J^{H}, and extend H′ to get

$$H^{"} = -\sum_{i,p,j,p',\sigma} t_{ipjp'}\left(c^{\dagger}_{ip\sigma}c_{jp'\sigma} + c^{\dagger}_{jp'\sigma}c_{ip\sigma}\right) + \sum_{i,p} U_{ip}n_{ip\uparrow}n_{ip\downarrow} + \sum_{i,p,p'=p} J^{H}_{i}n_{ip\uparrow}n_{ip'\downarrow}$$

where the first index of the electron operators (i and j) account for the site, the second index (p and p') account for the orbital within each site, and the third index (σ) accounts for the spin. Exactly as in the case of H′, H″ includes an on-site (on-orbital) energy penalty of the pairing of electrons in orbital p on site i (U_{ip}). The Hund energy is added as an energy penalty for not maximizing the spin angular momentum of each multiorbital site i (J_i^H).

Within this Hamiltonian, we are now equipped to study how ferromagnetic coupling can also emerge from superexchange interactions. We will investigate the hypothetical case of a linear transition metal/oxygen/transition metal bond, considering only the x^2-y^2 and z^2 orbitals and one electron per transition metal. Then the only bond is the σ bond between the transition-metal x^2-y^2 and oxygen p orbitals, and the z^2 orbital is nonbonding.

Let us consider a special case of a type of charge and orbital ordering. First, we will enforce charge order; that is, we add yet another energy penalty (V) for two electrons to be on different orbitals of the same site, i.e.

$$\hat{H} = H'' + \sum_{i,p,p' \neq p,\sigma,\sigma'} \upsilon_i n_{ip\sigma} n_{ip'\sigma'}$$

Furthermore, we enforce that the electron on the one transition metal prefers to occupy the x^2-y^2 orbital (in site 1 of Fig. 3.10) and the electron in the other transition metal prefers to occupy the z^2 orbital (in site 2 of Fig. 3.10).[‡‡] If $t \ll \upsilon$, the added term effectively renders the hopping of the electron on the left to the right side as transient (virtual); that is, it must spend most of its time on the left side. A qualitative description will be given here, and a more rigorous treatment with all of the appropriate arguments can be found in Appendix A.3.

In order to lower the energy of the system, the electron on left side (see Fig. 3.9) will want to hop to the x^2-y^2 orbital on the right side. The question is whether this hopping induces magnetic exchange. When the electron in the z^2 orbital has a different spin orientation from the hopping electron, the system is penalized an energy J^H. Therefore, parallel alignment of electrons is favored—ferromagnetic coupling. From these simple arguments, we learn two important things. First, localized moments in insulating oxides with the aforementioned orbital configuration can have ferromagnetic interaction. The second important realization is that without such charge and orbital restrictions, a multiorbital system that is not perfectly half-filled can easily be a diamagnetic and ferromagnetic metal even if $B = 4t$ is smaller than U. These ideas pervade the discussions in Chapters 4 and 5.

[‡‡] This is a case of orbital ordering, which will be discussed in greater detail in Chapter 5. Here, we have demanded such an orbital condition on the system without justifying its origins. Also, the energy associated with such ordering is not specifically taken into account in the Hamiltonian H″. Although all of these restrictions may seem somewhat arbitrary, they are quite commonplace in transition-metal perovskites because of the strong coupling among the charge, orbital, spin, and lattice states.

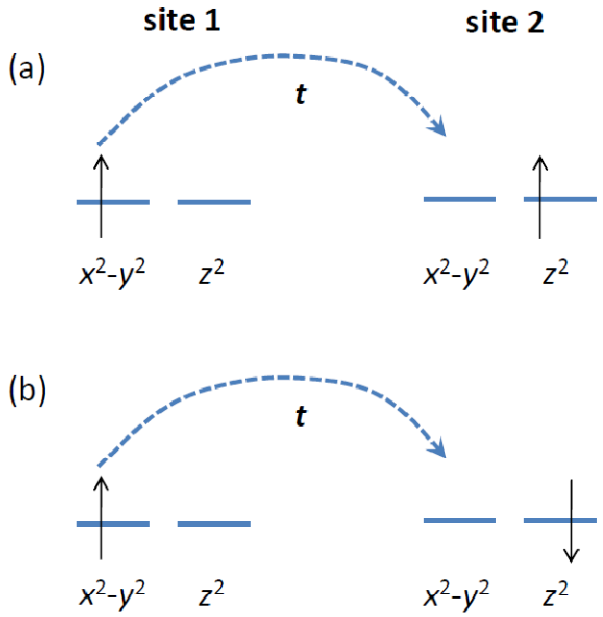

Figure 3.10. Schematics of the transient hopping with amplitude *t* in a two-site system with two orbitals and one electron per site. The hopping in the case of (b) antiparallel moment alignment incurs a Hund energy penalty, while in the case of (a) parallel moment alignment it does not.

Chapter 4

Strain-induced metallicity in $LaTiO_3$ thin films

4.1. Proximity to electronic instability of bulk $LaTiO_3$ 38
4.2. Growth and structure of $LaTiO_3$ thin films 41
4.3. Substrate-dependent electrical transport of $LaTiO_3$ films 45
4.4. Strain-induced metallicity of $LaTiO_3$ films on $SrTiO_3$ substrates 48
4.5. Elimination of other potential sources of metallicity 50
4.6. Outlook on strain engineering of electronic transitions in single-valent oxides 55
4.7. Concluding remarks 56

This chapter discusses an insulator-metal transition in $LaTiO_3$ thin films induced by heteroepitaxial strain. The data presented here suggest that metallic conduction can be realized in epitaxial tetragonally distorted $LaTiO_3$ thin films on (001) $SrTiO_3$ substrates, while films grown on (110) $DyScO_3$ and $GdScO_3$ substrates are insulating.* These results illustrate the sensitivity of electrical transport to lattice effects and demonstrate the tunability of correlated oxide thin-film properties through substrate-induced tetragonal deformation.

There has been renewed interest in $LaTiO_3$ after reports of metallicity in $LaTiO_3/SrTiO_3$ superlattices that was attributed to Mott/band insulator interfacial electronic reconstruction, arising from the Ti^{3+}/Ti^{4+} charge discontinuity at the interface [1]. Metallic conduction was thought to occur only at the interface with $SrTiO_3$. Interfacial polar discontinuity will be discussed in greater detail in Chapter 6. However, it will be argued here that since $LaTiO_3$ has a small Mott gap of ~0.1 eV, measured optically [2], the material itself is on the brink of an electronic transition; therefore, any small external perturbation can profoundly alter its electronic properties. Lattice strain from heteroepitaxy will be shown to be capable of inducing an electronic transition in $LaTiO_3$. Hence, in addition to any possible interfacial effects in superlattices, the role of lattice distortions must be examined carefully.

Prior to the presentation of the experimental data, properties of bulk $LaTiO_3$ will be overviewed. Special emphasis is placed on how and why $LaTiO_3$ is near an electronic instability. The growth conditions and transport properties of $LaTiO_3$ will then be shown, followed by a systematic presentation of reference samples to test for other possible sources of metallic conduction measured in strained $LaTiO_3$ films on (001) $SrTiO_3$ substrates. The findings here will be compared to a recent computational study on the electronic structure of strained $LaTiO_3$ [3]. The chapter ends with comments and an outlook on other perovskite oxides that may be susceptible to strain-induced metal-insulator transitions.

§ 4.1 Proximity to electronic instability of bulk $LaTiO_3$

Electron correlations are thought to be important for most 3*d* transition-metal perovksite oxides. In the limit of on-site potential energy (U) being much greater than transfer integral (t) between neighboring electronic sites ($U \gg t$), the Hubbard Hamiltonian applied to a system of exactly half-filled orbitals invariably yields an insulating state with antiferromagnetically coupled electrons. One can think of such a system as a canonical Mott insulator. However, because of the orbital degeneracy of the t_{2g} and e_g states, for many materials these states are not exactly half-filled. Although antiferromagnetic insulators are predicted for systems with half-filled orbitals, when interacting orbitals are

* Substrate orientations will be discussed in Section 4.2.

not exactly half-filled, there is ambiguity as to whether ferromagnetism, antiferromagnetism, or no long-range ordering is most stable; furthermore, it is unclear whether the material would be a metal or insulator. The charge, spin, orbital, and lattice states can be intimately coupled.

$LaTiO_3$ is a $3d^1$ transition-metal system, with one *d* electron occupying the three-fold degenerate t_{2g} levels. In fact, when the one electron randomly occupies any of the three orbitals, i.e. exercises its orbital degree of freedom, the antiferromagnetic, insulating state becomes unstable. It is precisely this electronic instability that can be exploited through heteroepitaxial strain of $LaTiO_3$ films. Further details on the role of orbital degeneracy in systems with orbitals that are not exactly half filled can be found in Appendix A.3.

In bulk form, $LaTiO_3$ is a Mott insulator that exhibits an orthorhombic $GdFeO_3$-type distortion [4,5], which is a relaxation mechanism for a tolerance factor less than 1. A brief discussion of the tolerance factor can be found in Section 3.2. The reduction of symmetry from a cubic to an orthorhombic structure can also break the degeneracy of electronic levels, and can then lead to preferential occupation of a certain t_{2g} orbital(s) rather than occupation of each of the three with equal probability. If the occupational preference of the different electronic states is weak, then the system is susceptible to orbital fluctuations, leading to instabilities of both the insulating state and long-range magnetic ordering of Mott insulators. This scenario seems to be the case in bulk $LaTiO_3$; although it is an antiferromagnetic Mott insulator, its moment is only 0.45 μ_B per Ti site [6]—reduced from the expected 1 μ_B. In a computational study, Pavarini *et al*. showed that distortions of the oxygen octahedra in $3d^1$ perovskite oxides can play a large role in suppressing orbital fluctuations and therefore stabilize not only the charge and orbital order but also the magnetic order of these systems [7].

Other compounds of $RTiO_3$ (*R* = trivalent rare-earth cation) also exhibit similar $GdFeO_3$-type distortions, wherein adjacent octahedra rotate about a common axis but in the opposite sense. Rotations about the [001] axis is schematically shown in Fig. 4.1b. The Ti-O-Ti angle between adjacent octahedra is reduced as a result, and the angle is used to quantify the degree of lattice distortion. Though the distortion in $LaTiO_3$ is orthorhombic rather than tetragonal to accommodate for internal lattice strain, the focus here will be on the local Ti-O-Ti bond angle and not the symmetry of the unit cell. For an orthorhombic distortion, the axis of collective octahedral rotations is <110>-type, but the key result is still reduced Ti-O-Ti bond angles. Figures 4.1c and 4.1d show a schematic representation of the change of π bonding between transition metal *d* orbitals with an oxygen 2*p* orbital as a result of bond rotation.

The Ti-O-Ti bond angle changes depending on the rare-earth cation in the A site. Compared to bulk $LaTiO_3$ with a Ti-O-Ti bond angle of 157°, $YTiO_3$ has a smaller angle of 140° [5]. Greater deviation from the ideal angle of 180° results in reduced hybridization of orbitals of adjacent atoms, i.e. electronic bandwidth; therefore, $YTiO_3$ has a much larger bandgap than $LaTiO_3$, ~1 eV compared to ~0.1 eV [2]. The significance of the role of local structural distortions in the titanates is exemplified by

bulk studies on $La_{1-x}Y_xTiO_3$; La^{3+} and Y^{3+} have the same valence, but the difference in the ionic radii of La^{3+} and Y^{3+} leads to an increase in magnitude of the $GdFeO_3$ distortion and subsequently an increase in magnitude of the bandgap E_g as x approaches 1 [8]. Furthermore, Crandles *et al*. investigated the gradual closing of the Hubbard gap, owing to changes in the tolerance factor and hence in electronic bandwidth, using optical absorption of Ti^{3+} titanites with different A-site cations [9].

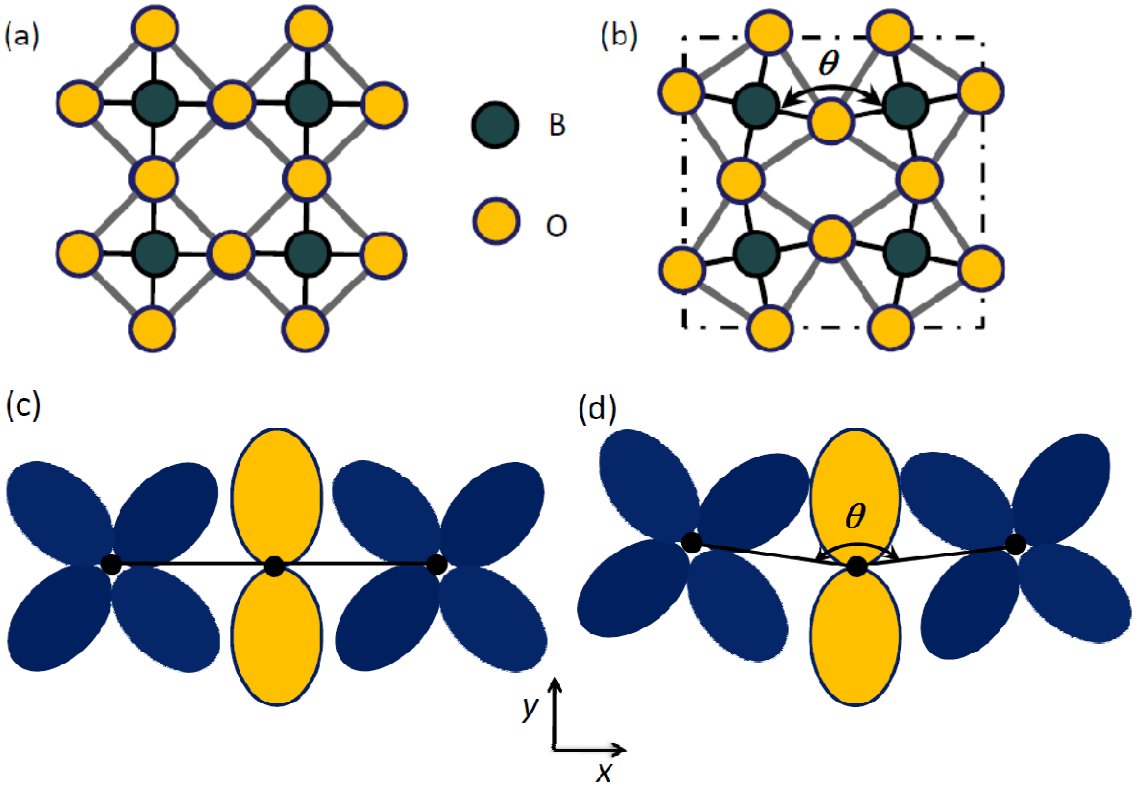

Figure 4.1. Schematics of the BO_2 plane (a) with and (b) without octahedral rotations about the [001] axis. Schematics of bonding between the Ti $3d_{xy}$ and O $2p_y$ orbitals with a Ti-O-Ti bond angle (c) equal to and (d) less than 180°.

Although significant D_{3d} distortions to the oxygen octahedra [5,10] and even Jahn-Teller distortions [11] have been claimed to stabilize the antiferromagnetism and induce orbital ordering of $LaTiO_3$, neutron scattering [12] and nuclear magnetic resonance [13] studies show no signs of orbital ordering in $LaTiO_3$, whereas staggered orbital ordering in $YTiO_3$ is clearly visible [13,14]. The staggered orbital ordering is directly related to the observed ferromagnetism [5], and this relation is fully expected according to the Goodenough-Kanamori rules. Ferromagnetic coupling arising from staggered orbital ordering is introduced in Section 3.7.2 and will be discussed in the context of the manganites in Section 5.2.

Much of the investigation of bulk $LaTiO_3$ suggests that it is indeed near an electronic instability, and it is possible to induce an insulator-metal transition through thin-film heteroepitaxy. There have been many investigations on effects of chemical substitution [8,15-20], cation vacancy [21], and hydrostatic pressure [16] on atomic structure, electronic band filling, and electrical and magnetic properties of bulk $LaTiO_3$; the work on substrate-induced strain effect should compliment bulk studies.

There have been several thin-film studies of $LaTiO_3$ [22-24] and $La_{1-x}Sr_xTiO_3$ [25,26], but the effects of epitaxial strain have not been carefully examined. The small band gap of $LaTiO_3$ makes it a particularly promising candidate to study an insulator-metal transition through changes in the electronic energy bandwidth induced by heteroepitaxial lattice perturbations.

§ 4.2 Growth and structure of $LaTiO_3$ thin films

The $LaTiO_3$ stoichiometry is difficult to stabilize in the bulk, because Ti prefers a 4+ to a 3+ oxidation state. Therefore, in fact many of the bulk properties of $LaTiO_3$ are still controversial, including its low-temperature antiferromagnetic state, as mentioned in previous sections. However, assisted by heteroepitaxial growth on an isostructural substrate and the typically reducing nature of the pulsed-laser deposition, $LaTiO_3$ thin films can be grown rather routinely.

Starting from a more oxidized $La_2Ti_2O_7$ target, Ohtomo *et al.* reported the stabilization $LaTiO_3$ thin films on perovskite substrates for oxygen partial pressures below 10^{-4} Torr over a range of 650 to 950 ^oC [22]. They used a combination of x-ray diffraction, scanning transmission electron microscopy, and electron energy loss spectroscopy to distinguish the $LaTiO_3$ and $La_2Ti_2O_7$ phases. Both x-ray diffractometry and electron microscopy revealed that a $LaTiO_3$ film on a (001) $SrTiO_3$ substrate can be grown under appropriate deposition conditions, and there are no reflections from possible $La_2Ti_2O_7$ secondary phases.

In principle to grow a more reduced phase, it is best to deposit the film at high temperatures and low oxygen pressures. However, that combination may lead to oxygen vacancies in the substrates, which are particularly concerning for $SrTiO_3$ substrates, where oxygen vacancies are known to be electrically active *n*-type dopants. Therefore, the compromise is to deposit $LaTiO_3$ films in as low oxygen pressures as possible, but also at as low temperatures as possible while still maintaining relatively high thin-film crystalline quality. The deposition times should also be short. It can be viewed that a more reduced phase is achieved kinetically rather than thermodynamically.

Thin films of $LaTiO_3$ were deposited in a vacuum of 5×10^{-6} Torr, at 625 ^oC, with a 3 Hz laser pulse rate, using a fluence of ~1.4 J/cm^2 on (001) $SrTiO_3$, (110) $DyScO_3$, and (110) $GdScO_3$ substrates. Because $DyScO_3$ and $GdScO_3$ crystals are slightly orthorhombically distorted, a (110) plane corresponds to a pseudo-(001) plane in these pseudocubic crystals. Although $DyScO_3$ and $GdScO_3$ are orthorhombic, the interplanar

spacing $d_{1\text{-}10}$ is extremely close to d_{002}; since [1-10] and [001] are orthogonal in-plane directions, the in-plane symmetry of the scandate substrates is nearly four-fold. The (pseudocubic) lattice parameters for $SrTiO_3$, $DyScO_3$, and $GdScO_3$ are 3.905, 3.942, and 3.968 Å, respectively—hence providing different degrees of heteroepitaxial lattice stress on the overlying $LaTiO_3$ film, whose bulk pseudocubic lattice parameter is 3.97 Å.[†]

Figure 4.2 shows atomic force microscopy (AFM) images of 34 nm $LaTiO_3$ films on the three substrates; the images reveal atomically smooth surfaces. To check that the $LaTiO_3$ phase is stabilized, 2θ with $\omega = 2\theta/2$ x-ray diffractometry scans were performed on all of the films, and the scans suggest that perovskite ABO_3 films were indeed deposited isostructurally onto perovskite substrates (Fig. 4.3), showing only the 00*l* reflections of both the substrates (high-intensity peaks) and thin films (low-intensity peaks). Furthermore, ω scans about the 002 thin-film reflections reveal small full-width-half-maximum values (Table 4.1).

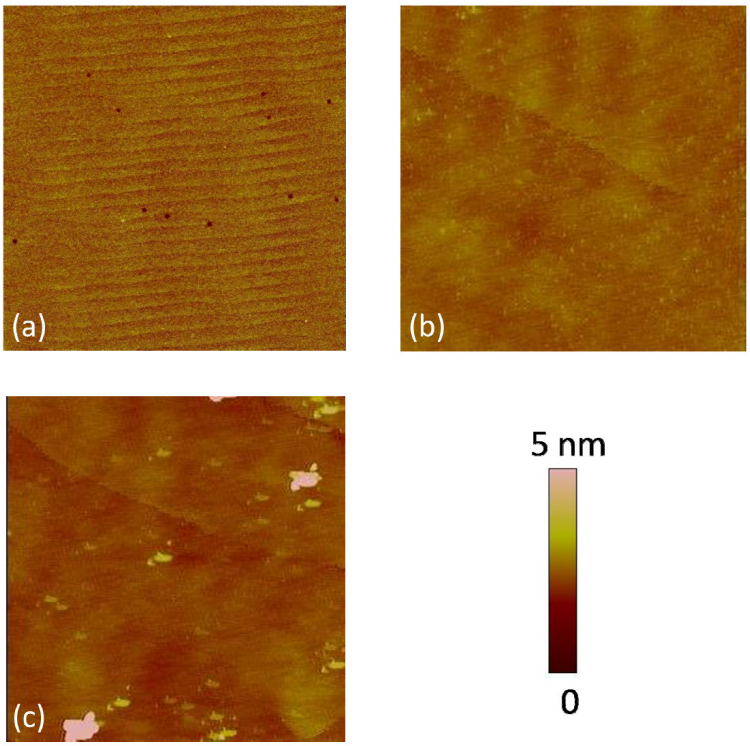

Figure 4.2. Atomic force microscopy images (5 μm × 5 μm) of $LaTiO_3$ films on (a) $SrTiO_3$, (b) $DyScO_3$, and (c) $GdScO_3$ substrates. Despite the particulates in image (c), the underlying film is still atomically smooth.

[† †] The pseudocubic lattice parameters for the scandates and $LaTiO_3$ are calculated as averages of their $d_{1\text{-}10}$ and d_{002} interplanar spacings.

Figure 4.4a is a high-resolution cross-sectional transmission electron microscopy (TEM) image of a $LaTiO_3$ film on a $SrTiO_3$ substrate at the film/substrate interface, showing epitaxial film growth. The fast Fourier transform of the image indicates that the film is single-phase and isostructural to the substrate. In addition, TEM imaging also confirms that the perovskite ABO_3 structure and the [001] growth orientation is preserved throughout the entire film, as seen in Fig. 4.4b which shows a section of the film away from the interface. Numerous images at different locations and magnifications on the sample were taken, and there was no indication of the oxygen-rich $La_2Ti_2O_7$ phase, whose structure in bulk [27] and thin-film [22,28] form have been reported in previous TEM studies. Therefore, the samples are expected to be nearly stoichiometric $LaTiO_3$, although this study does not include a measurement of possible slight nonstoichiometries.

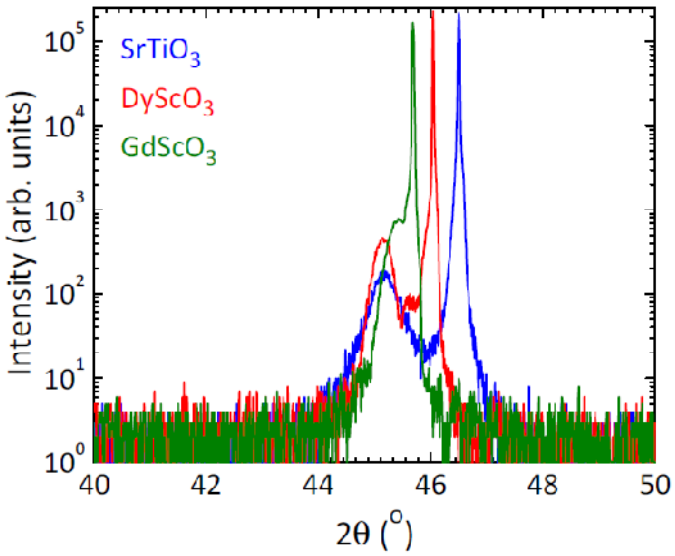

Figure 4.3. 2θ scans of the out-of-plane 00*l* reflections.

Table 4.1. In-plane and out-of-plane lattice parameters (*a* and *c*) of 34 nm $LaTiO_3$ films grown on different substrates. Strain components associated with volume dilation and tetragonal distortions are estimated for each sample.

Substrate	*a* (Å)	*c* (Å)	FWHM (°)*	$\varepsilon_{xx}+\varepsilon_{yy}+\varepsilon_{zz}$	$2\varepsilon_{zz}-\varepsilon_{xx}-\varepsilon_{yy}$
$GdScO_3$	3.968	3.991	0.075	0.43%	1.16%
$DyScO_3$	3.944	4.014	0.07	-0.20%	3.52%
$SrTiO_3$	3.905	4.015	0.06	-2.14%	5.54%

*full-width at half-maximum of the 002 reflection

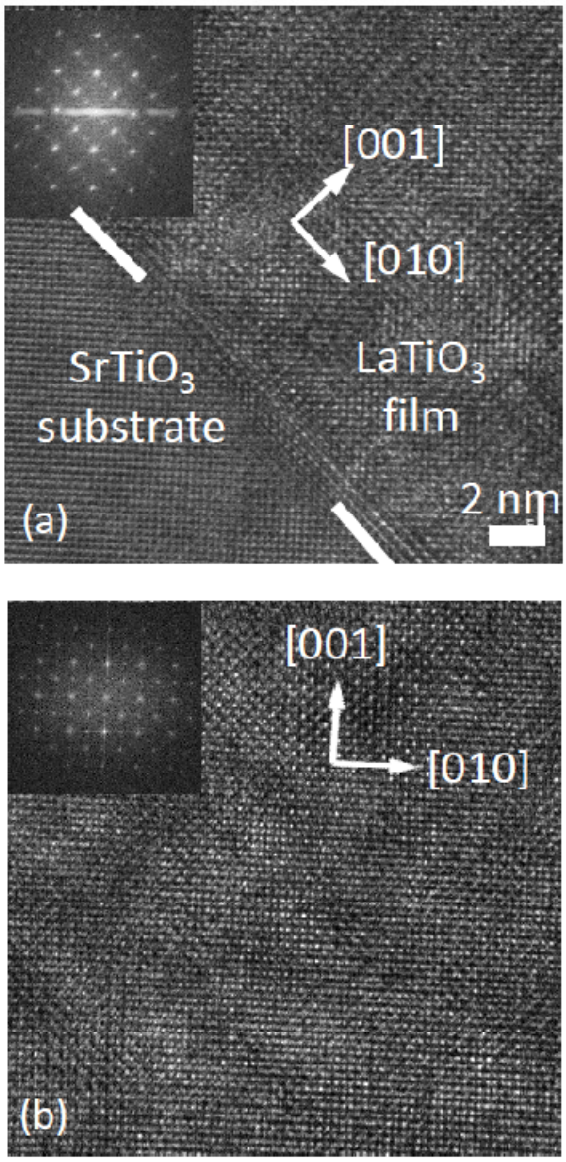

Figure 4.4. Cross-sectional transmission electron micrographs of (a) the $SrTiO_3/LaTiO_3$ interface and (b) the only $LaTiO_3$ film along the [100] zone axis. [001] is the growth direction. The insets are fast Fourier transforms of the images.

For verification of in-plane strain coherency of the films, scans of reflections with in-plane components must be performed. Reciprocal space maps (RSMs) of the 103 $LaTiO_3$ peak allow for determination of both out-of-plane and in-plane lattice parameters of the $LaTiO_3$ films and verify that the films are coherently strained to the substrate. Figure 4.5 is a RSM of the 103 reflection of a 34 nm $LaTiO_3$ film on $SrTiO_3$, and the thin-film in-plane and out-of-plane lattice parameters are 3.905 Å and 4.015 Å, respectively. The intensity streak of the substrate peak is caused by the line-focused shape of the x-ray beam. The 103 reflection peaks of 34 nm films on $DyScO_3$ and

$GdScO_3$ substrates were likewise mapped out to determine in-plane and out-of-plane lattice parameters (Table 4.1). The in-plane and out-of-plane lattice parameters presented in Table 4.1 were determined by x-ray scans taken by S.-H. Baek of Materials Science and Engineering, University of Wisconsin, Madison. The small degree of orthorhombic in-plane distortion from the scandate substrates amounts to less than 0.005 Å difference in in-plane interplanar spacings, and is difficult to detect in thin films because of the lack of diffracted intensity owing to finite size. In summary, all of the films are coherently strained in plane to conform to the underlying substrates.

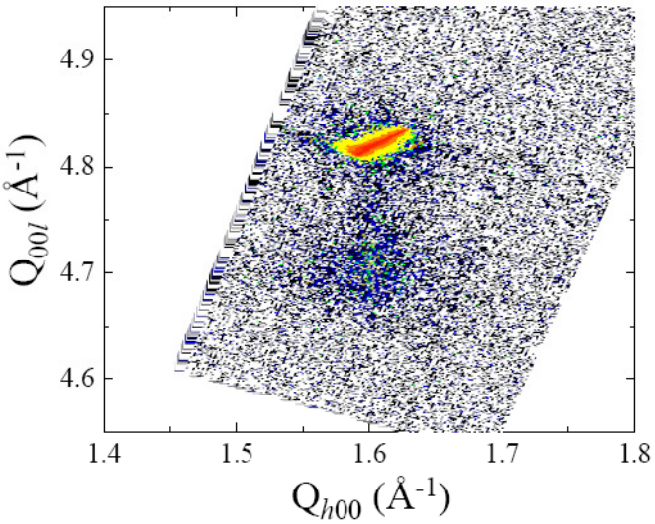

Figure 4.5. Reciprocal lattice map of the 103 reflection of the $SrTiO_3$ substrate (more intense peak) and the $LaTiO_3$ thin film (less intense peak).

§ 4.3 Substrate-dependent electrical transport of $LaTiO_3$ films

Electrical transport measurements in the van der Pauw geometry were performed on the films. Figure 4.6 shows resistivity curves of 34 nm $LaTiO_3$ film on $SrTiO_3$ as well as $LaTiO_3$ films of the same thickness grown on $DyScO_3$ and $GdScO_3$ under the same deposition conditions. While the $LaTiO_3$ film on $SrTiO_3$ displays metallic behavior, $LaTiO_3$ films on both $DyScO_3$ and $GdScO_3$ are insulating—though $LaTiO_3$ on $GdScO_3$ exhibits higher resistivity than $LaTiO_3$ on $DyScO_3$ over the entire measured temperature range.

Furthermore, $LaTiO_3$ films on $SrTiO_3$ are metallic for all film thicknesses measured in this study. Fig. 4.7a shows that the metallic resistivity curves of the different samples overlay one another for film thicknesses from 15 to 45 nm. The magnitude and temperature dependence of the resistivity values are comparable to those of the metallic d^1 perovskite oxide ReO_3 [29]. Spectroscopic features of ReO_3 suggest that its free carriers are sufficiently mobile to screen would-be correlation effects [30]. An insulator-

metal transition in $LaTiO_3$ may result in a similar effect. The inverse scaling of sheet resistance at 300 K with film thickness is shown in Fig. 4.7b. In Fig. 4.7c, it can be seen that specifically the sheet carrier concentration values increase roughly linearly with film thickness, indicating that higher sample conductance in thicker films is due to more carriers rather than higher mobility. This scaling is evidence that the metallic conduction occurs in the entire film. It is found by x-ray diffraction that over this thickness range, the out-of-plane lattice parameter of the $LaTiO_3$ does not noticeably change, suggesting preservation of thin film/substrate coherence.

Hall effect measurements were performed on the 34 nm $LaTiO_3$ film on $SrTiO_3$ to decouple the carrier concentration and mobility over the temperature range from 3 K to room temperature (Fig. 4.8). The carriers are electron-like. The carrier concentration is fairly temperature-independent and corresponds to an average of 0.77 electrons per Ti cation. Its Hall mobility has a power-law dependence at high temperatures, $\mu_H \propto T^{-3.07}$, and the main scattering mechanism likely is carrier interaction with optical phonons. Carrier mobility limited by optical phonons, particularly the longitudinal modes, is common in polar oxide materials. At low temperatures, the resistivity is governed by scattering by defects in and at the boundaries of the sample, and the mobility saturates to ~10^4 cm^2/Vs. Attempts in performing Hall effect measurements on the $LaTiO_3$ films on $DyScO_3$ and $GdScO_3$ resulted in data that translate to very low effective mobility values (< $1cm^2/Vs$), which correspond to mean free paths smaller than a lattice constant, thus suggesting non-Boltzmann-like transport. Therefore, meaningful carrier concentration and mobility values cannot be easily deduced from Hall effect measurements on these samples. Regardless, it can still be inferred that the reason for the low conductance of these samples is immobile electrons rather than the lack of carriers, as would be expected for conventional semiconductors or insulators.

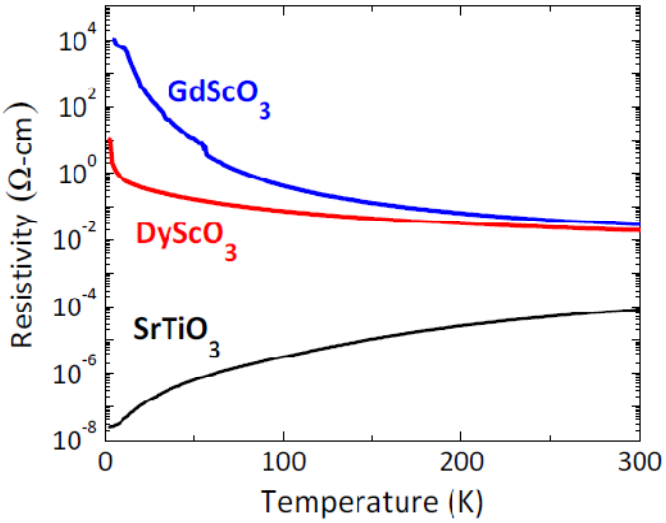

Figure 4.6. Resistivity curves of the three 34 nm $LaTiO_3$ films on (001) $SrTiO_3$, (110) $DyScO_3$, and (110) $GdScO_3$ substrates. Difficulties in maintaining an ohmic contact on an insulating sample contributed to the noise at low temperatures observed in $LaTiO_3$ on $GdScO_3$.

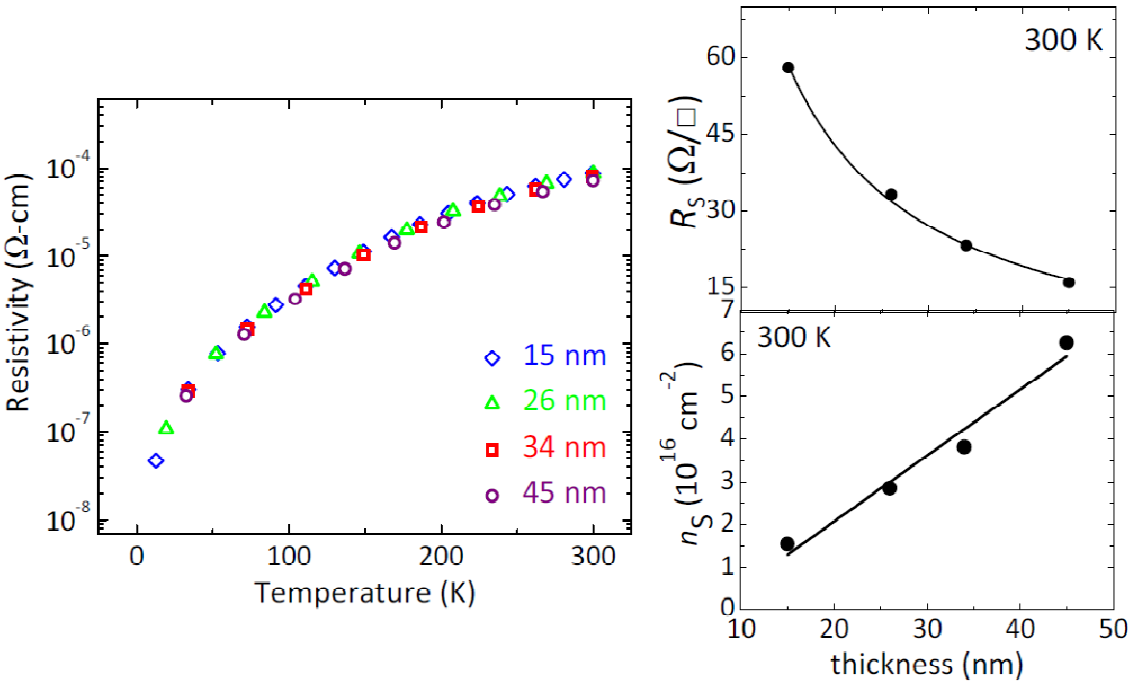

Figure 4.7. (a) Resistivity of $LaTiO_3$ thin films of different thicknesses on (001) $SrTiO_3$ substrates. Film thickness-dependent variations in (b) sheet resistance and the (c) sheet carrier concentration measured at 300 K.

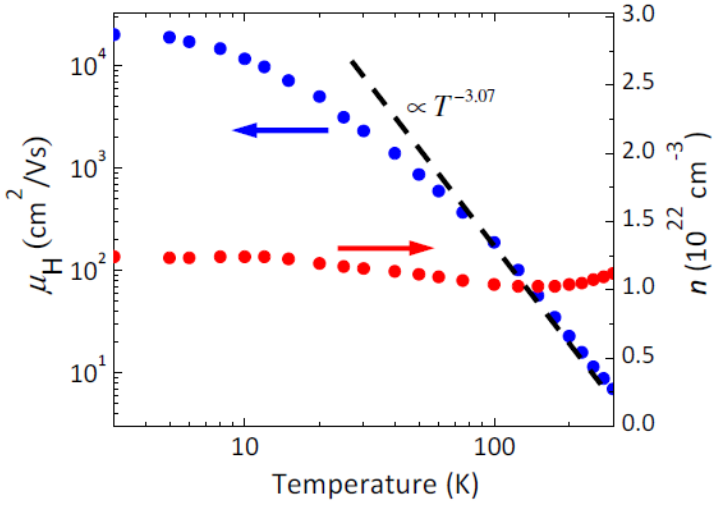

Figure 4.8. Hall mobility (μ_H) and carrier concentration (n) of the 34 nm $LaTiO_3$ film on a $SrTiO_3$ substrate.

§ 4.4 Strain-induced metallicity of $LaTiO_3$ films on $SrTiO_3$ substrates

It is common to probe the electronic properties of crystalline bulk oxides under hydrostatic pressure, which can cause two different and somewhat competing effects: (1) the shortening of bonds, which increases hybridization and therefore the transfer integral, and (2) rotation of bonds, which decreases the transfer integral. The following dependence of π bonding (t_{2g}) matrix element of a single transition metal-oxygen bond can be shown to be [31]

$$t_{dp\pi} \propto \frac{1}{\lambda^{7/2}} |cos\theta|$$

where λ is the bond length and θ is the bond angle as illustrated Fig. 4.1d. For the electrons to have high kinetic energy, the bonds should be as short as possible but without significant bond rotations. Experimentally, hydrostatic pressure on $LaTiO_3$ has been shown to result in higher sample conductance, but an insulator-metal transition was not induced [16]. Nevertheless, based on these finding, it appears that some degree of compression can be introduced to $LaTiO_3$ without causing significant bond rotations so that the band kinetic energy of electrons would increase. Unlike hydrostatic pressure studies on bulk crystals, higher magnitudes of lattice distortions can be readily achieved in heteroepitaxial films; furthermore, the inherent anisotropy of heteroepitaxial strain can be exploited, particularly when the tuning parameter of interest is lateral conductivity.

The metallic behavior of $LaTiO_3$ films on $SrTiO_3$ versus the insulating behavior of $LaTiO_3$ films on $DyScO_3$ and $GdScO_3$ substrates can be correlated with the atomic structure of the $LaTiO_3$ films. Since detailed structural characterization indicates that the $LaTiO_3$ films are coherently grown on all substrates with a high degree of crystallinity and smooth surfaces, the electronic transition cannot be attributed to differences in microstructure or defect structure.

The observation of insulating to metallic behavior that depends on the choice of underlying substrate indicates that lattice distortions profoundly modify the electronic structure of $LaTiO_3$. As there is no off-diagonal element shear strain in (001) heteroepitaxy; only volume dilation and tetragonal distortion need to be considered. The strain tensor elements are defined in Appendix A.1. From the measured in-plane and out-of-plane lattice parameters, the volume dilation $\varepsilon_{xx} + \varepsilon_{yy} + \varepsilon_{zz}$ and an element representing the degree of volume-preserving tetragonal distortion $2\varepsilon_{zz} - \varepsilon_{xx} - \varepsilon_{yy}$ can be deduced (Table 4.1). $LaTiO_3$ is virtually lattice-matched with the $GdScO_3$ substrate; hence, there is little in-plane compression. In the $LaTiO_3$ film on $DyScO_3$, the film is under a slight compressive strain (-0.7%) and exhibits resistivity values from a factor of about two at room temperature to more than two orders of magnitude at low temperatures lower than those of $LaTiO_3$ on $GdScO_3$. Finally under a larger compressive strain (-1.6%), $LaTiO_3$ films on $SrTiO_3$ films undergo a lattice-induced insulator-metal

transition. Greater in-plane compression yields structural anisotropy, resulting in metallic conduction in $LaTiO_3$ on $SrTiO_3$.

It appears that on $SrTiO_3$, the strained $LaTiO_3$ film is distorted to the degree that its kinetic energy—electronic bandwidth—overwhelms the potential energy—on-site repulsion energy. The implication is that the in-plane compression shortens the Ti-O bonds without excessively reducing the Ti-O-Ti bond angle, leading to a net increase of hydridization and hence greater kinetic energy—consistent with the aforementioned hydrostatic pressure studies of bulk crystals. It is unclear whether that volume contraction or tetragonal distortions are more important in inducing metallicity in $LaTiO_3$. The two contributions cannot be systematically separated out in heteroepitaxial systems, as elastic deformation is not volume-preserving. In general for many similar oxides, in-plane compression (tension) leads to volume contraction (expansion). Furthermore, from lattice parameters listed here, it is possible that the degree of strain is large enough that the films on $SrTiO_3$ substrates are beyond the linear regime of elasticity. It has also been argued that a localized-to-itinerant (insulator-metal) transition typically comes about with volume contraction owing to the shortening of bonds between the transition metal and oxygen [32]; if this statement is applicable for a variety of oxide materials, it may suggest that achieving insulator-metal transitions through in-plane thin-film compression should be particularly effective. However, as will be shown in Chapter 5, this condition is by no means general. In any case, it is clear than the in-plane compression is important to the insulator-metal transition in $LaTiO_3$ thin films.

Although the tetragonal distortions in $LaTiO_3$ films on $DyScO_3$ are insufficient to induce metallicity, it is speculated the slight in-plane compression produces a larger bandwidth of occupied states and hence higher electronic kinetic energy and conductance in $LaTiO_3$ on $DyScO_3$ compared to that on $GdScO_3$. In order to fully understand metallic conduction in $LaTiO_3$ on $SrTiO_3$, electron-phonon interactions in tetragonally deformed $LaTiO_3$ thin films must be also explored. Phonon dispersion in distorted $LaTiO_3$ and electron-phonon interactions are topics that warrant further attention in future studies.

Ishida and Liebsch considered tetragonal distortions in $LaTiO_3$ and found broadening of the t_{2g} bands compared to the orthorhombic bulk structure [3]. The in- and out-of-plane lattice parameters that they used for the strained $LaTiO_3$ on $SrTiO_3$ were 3.92 and 4.01 Å respectively, corresponding to $\varepsilon_{xx} + \varepsilon_{yy} + \varepsilon_{zz} = -1.52\%$ and $2\varepsilon_{zz} - \varepsilon_{xx} - \varepsilon_{yy} = +4.53\%$ [3]; though not exactly the same, their values are comparable to the experimental values in this work. Their calculations show that tetragonally distorted $LaTiO_3$ on $SrTiO_3$ exhibits metallicity, while orthorhombic bulk $LaTiO_3$ is an insulator. The metallicity observed in the $LaTiO_3$ films on $SrTiO_3$ reported here is qualitatively consistent with their claim that bonding effects, in the form of reduced magnitude of t_{2g} band splitting[‡] and enhanced electron bandwidth near the Fermi level, are important factors in the stabilization of a metallic ground state in tetragonally deformed $LaTiO_3$. However, one of the shortcomings of their computational study is that they did not take

[‡] There is energy splitting of the t_{2g}-like bands because of noncubic distortions.

into account rotations and tilting of the oxygen octahedral cages. Such distortions result in deviation of the Ti-O-Ti bond angle from 180°, as is visualized in Figs. 4.1b and 4.d, and can therefore lead to reduction in bond hybridization. Regardless, experimentally, metallicity can be achieved in tetragonally deformed $LaTiO_3$ films on $SrTiO_3$ substrates.

We also cannot ignore the role of electron-electron correlations even in the metallic state of $LaTiO_3$. Given the high mobility values measured in $LaTiO_3$ films on $SrTiO_3$ substrates, electron-electron interactions intrinsic to $LaTiO_3$ are not strong enough to limit the mobility of the films. The role of screening effects at the $LaTiO_3$ film/substrate interface must also be considered since $SrTiO_3$ has a high and highly temperature-dependent dielectric constant, whereas the dielectric response of $DyScO_3$ and $GdScO_3$ are lower and constant with temperature [33]. The fact that metallic behavior is not observed in a $LaTiO_3$ film on 10 nm $SrTiO_3$-buffered $DyScO_3$ substrate (as will be further discussed in the next section) suggests that dielectric screening is not the primary cause of metallicity and has, at most, a second order effect in carrier itineracy, such as allowing for high mobility. It is possible that dielectric screening from the $SrTiO_3$ substrate screens would-be strong electron-electron correlations in the $LaTiO_3$ films, allowing carriers in $LaTiO_3$ to behave as nearly free electrons. While the finding in this work cannot completely decouple the effects of screening across the interface, the transport properties over a range of film thicknesses in $LaTiO_3$ films on $SrTiO_3$ indicate that tetragonal distortions play a dominant, likely the primary, role in inducing metallicity in $LaTiO_3$ thin films. Screening from nearly free electrons can cause a positive feedback effect. The more effective screening is, the freer the conduction electrons become; the freer the conduction electrons are, screening becomes more effective.

§ 4.5 Elimination of other potential sources of metallicity

Because of the sensitivity of the electrical transport of both $SrTiO_3$ and $LaTiO_3$ to crystal defects, several different possibilities of defect-induced metallic conduction were systematically ruled out. Unintentional doping by interdiffusion, oxygen vacancy formation in $SrTiO_3$ during the deposition process, and electronic reconstruction were considered and tested as possible origins of the observed metallicity.

Sr doping of $LaTiO_3$ is known to cause *p*-type conduction [25,26,34]. In addition La doping of $SrTiO_3$ can induce not only *n*-type metallicity, but also superconductivity for a range of dopant concentrations [35]. As revealed by the Hall effect, since the carriers in the $LaTiO_3$ films on $SrTiO_3$ are electron-like, *p*-type Sr doping of $LaTiO_3$ cannot possibly explain the observed metallicity. Moreover, Rutherford backscattering spectrometry analysis indicates that interdiffusion is negligible compared to the film thicknesses and cannot produce the large carrier densities observed in the $LaTiO_3$ films on $SrTiO_3$ substrates; hence, it is improbable that the measured metallic conduction be due to La doping of $SrTiO_3$.

The major concern was to check for the possibility of introduction of mobile electrons in the $SrTiO_3$ substrate by creating oxygen vacancies, known to be electron donors in $SrTiO_3$ [36], during the pulsed-laser deposition process. Oxygen vacancies act as donors to many such oxides by the reaction:

$$(O^{2-}{}_{O^{2-}})^0 \rightarrow (V_{O^{2-}})^{2+} + 2e^-$$

A $SrTiO_3$ substrate loaded into the chamber and just annealed in the deposition conditions of $LaTiO_3$ thin films did not show metallic behavior. Therefore, the deposition temperature and pressure in themselves could not have caused metallicity in the $SrTiO_3$ substrates. A sample of a 10 nm $EuTiO_3$ thin film grown on $SrTiO_3$ in the same deposition conditions was made to test whether an actual deposition can cause metallic substrates. With Eu^{2+} and Ti^{4+} cations, $EuTiO_3$ is a material that is likewise optimally grown in rather reducing conditions to prevent the formation of Eu^{3+} cations, which is the preferred oxidation state; the stabilization of the phase close to the $EuTiO_3$ stoichiometry can be checked by a 2θ scan of the out-of-plane reflections that shows the growth of a single-phase film isostructural to the perovskite substrate (Fig. 4.9). Figure 4.10 shows the electrical transport measurements of the sample, and it can be seen that the sample is too insulating to be measured electrically. The apparent noise in the data signifies the difficulty of maintaining ohmic contacts on and measuring large resistance values of an insulating sample. Therefore, it is concluded that the deposition conditions alone do not result in metallic $SrTiO_3$ substrates. Moreover, given the short deposition times—3 to 20 minutes depending on film thickness—and oxygen vacancy diffusion constants [37], the carrier concentration numbers cannot be explained in terms of reduced $SrTiO_3$ substrates.

Although the aforementioned sample suggests that electron-doped $SrTiO_3$ substrates are not created during thin-film deposition, it does not immediately indicate that lattice deformation is the key component to the insulator-metal transition. Because $EuTiO_3$ (a ~ 3.92 Å) has a similar lattice parameter to $SrTiO_3$ (a = 3.905 Å), a 10 nm coherently strained buffer layer of $EuTiO_3$ on a $SrTiO_3$ substrate was used as a template for deposition of a 17 nm $LaTiO_3$ film ($SrTiO_3$ // $EuTiO_3$ / $LaTiO_3$), which is expected to undergo a similar thin-film lattice distortion as would be if it were directly on a $SrTiO_3$ substrate. Atomic force microscopy image of $SrTiO_3$ // $EuTiO_3$ / $LaTiO_3$ reveals terraces of unit-cell height (Fig. 4.11), showing that the insertion of $EuTiO_3$ buffer layer likely does not degrade the growth of the $LaTiO_3$ film. Figure 4.12 shows that the temperature-dependent resistivity curves of $SrTiO_3$ // $EuTiO_3$ / $LaTiO_3$ and a 17 nm $LaTiO_3$ film grown directly on a $SrTiO_3$ substrate are roughly the same for the entire temperature range. Since the $EuTiO_3$ layer barely contributes to sample conductance as was determined by the transport measurements of the single $EuTiO_3$ film, the resistivity values were attained by multiplying the sheet resistance values with just thickness of the $LaTiO_3$ film. This result implies that substrate-induced lattice distortions are indeed the origin of metallicity in tetragonally deformed heteroepitaxial $LaTiO_3$ films on $SrTiO_3$ substrates.

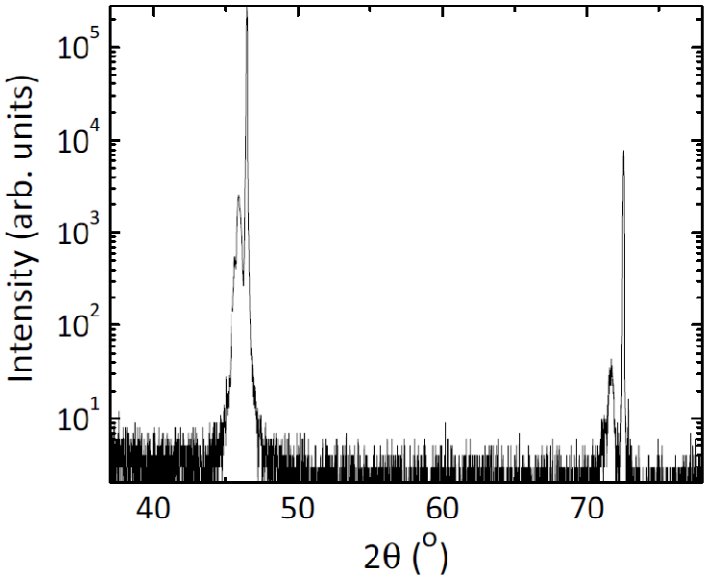

Figure 4.9. 2θ scan of a 15 nm $EuTiO_3$ film on a $SrTiO_3$ substrate.

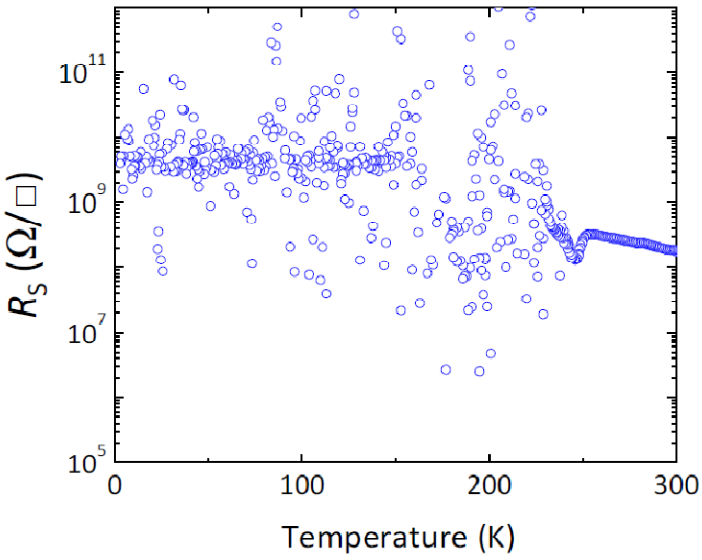

Figure 4.10. Temperature-dependent sheet resistance of a 15 nm $EuTiO_3$ on a $SrTiO_3$ substrate.

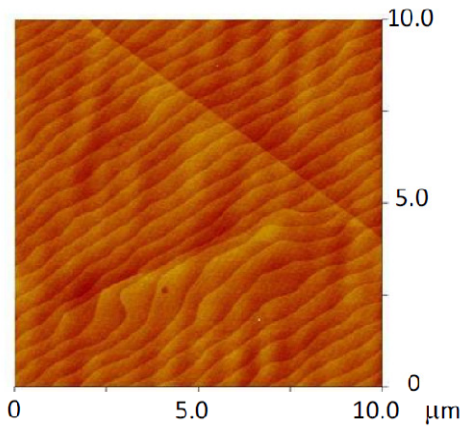

Figure 4.11. A 10 µm × 10 µm atomic force microscopy scan of the $SrTiO_3$ // $EuTiO_3$ / $LaTiO_3$ sample.

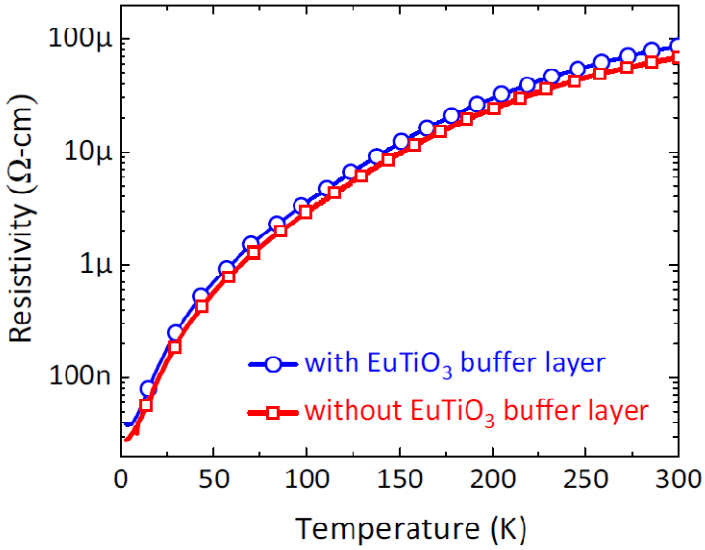

Figure 4.12. Temperature-dependent resistivity of a 17 nm $LaTiO_3$ on a $SrTiO_3$ substrate with and without a 10 nm $EuTiO_3$ buffer layer in between.

Finally, metallicity through interfacial electronic reconstruction must also be considered. In order to test for this possibility, a 10 nm $LaTiO_3$ film was deposited on a $DyScO_3$ substrate with a 7 nm $SrTiO_3$ buffer layer ($DyScO_3$ // $SrTiO_3$ / $LaTiO_3$). The $SrTiO_3$ film was first deposited at 700 °C in 2.5×10^{-5} Torr of oxygen; the chamber was then evacuated, and the $LaTiO_3$ film was deposited at 625 °C in vacuum. Again because the $SrTiO_3$ buffer layer is thin, the $LaTiO_3$ film is expected to be deformed similarly to a film directly deposited on a $DyScO_3$ substrate. Figure 4.13 reveals that the sheet

resistance of this sample has weak temperature dependence. Furthermore, the mobility and sheet carrier concentration (Fig. 4.14) are also found to be weakly temperature-dependent. Since the sheet resistance curve does not resemble that of a single $LaTiO_3$ film on $DyScO_3$, other possibilities must be taken into account. If sample conductance were to arise mainly from the thin layer of $SrTiO_3$, lower sheet carrier concentration but higher mobility values would be expected. For example, assuming that all of the carriers are in the thin $SrTiO_3$ layer, a measured sheet concentration of about 3.5×10^{15} cm^{-2} corresponds to a volume concentration of about 5×10^{21} cm^{-3}, which roughly translates to one carrier per three unit cells of $SrTiO_3$. Such a high carrier concentration in $SrTiO_3$, a band insulator which has no *d* electrons in its undoped state, is unlikely. It is possible that conductance arises from both the $LaTiO_3$ and $SrTiO_3$ layers as well as the interface between them through electronic reconstruction. Since there may be at least two types of carriers, the Hall effect measurements are difficult to interpret. It is speculated that the $SrTiO_3$ has a much lower concentration of but more mobile carriers, and its conductance is the dominant term at low temperatures; the $LaTiO_3$ layer has a much higher concentration of but less mobile carriers, and its conductance is the dominant term at high temperatures. Furthermore in this case, the conduction in $LaTiO_3$ is expected to be hopping transport rather than Drude-like. In any case, the differences in the temperature dependences and magnitudes of resistivity, carrier concentration, and mobility of $DyScO_3$ // $SrTiO_3$ / $LaTiO_3$ sample and the $LaTiO_3$ films on $SrTiO_3$ substrates indicate that any possible electronic reconstruction at the $LaTiO_3/SrTiO_3$ interface cannot completely explain the metallicity in strained $LaTiO_3$ films.

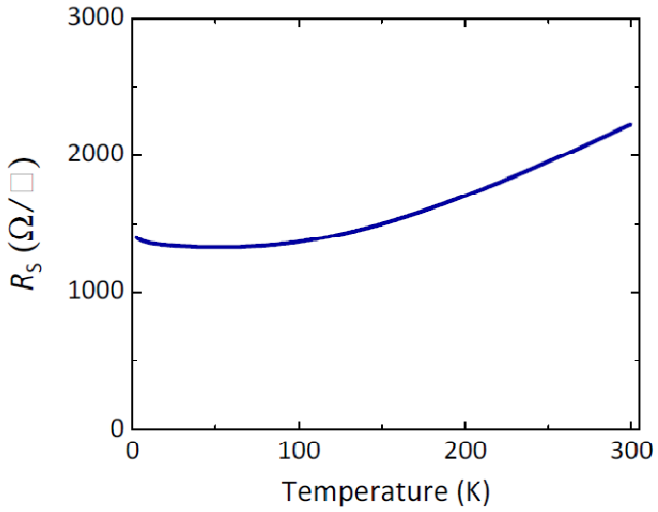

Figure 4.13. Temperature-dependent sheet resistance of a 10 nm $LaTiO_3$ film on a (110) $DyScO_3$ substrate with a 10 nm $SrTiO_3$ buffer layer in between ($DyScO_3$ // $SrTiO_3$ / $LaTiO_3$).

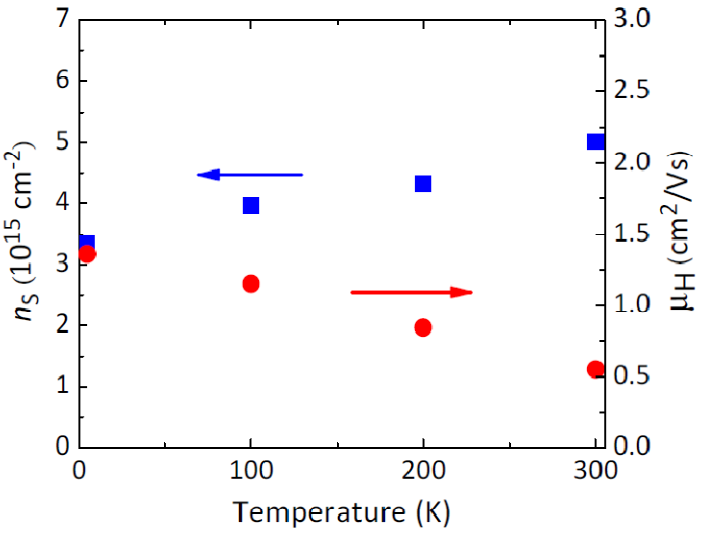

Figure 4.14. Temperature-dependent sheet carrier concentration and Hall mobility of $DyScO_3$ // $SrTiO_3$ / $LaTiO_3$.

§ 4.6 Outlook on strain engineering of electronic transitions in single-valent oxides

There has been a vast array of studies on superlattices and heterointerfaces that aim at generating new states at interfaces. This work shows that when one incorporates a Mott insulator that may be close to an instability—usually signified by a small band gap—lattice perturbation from heteroepitaxy may play a more dominant role than any interfacial charge redistribution. This chapter will end with a short discussion commenting on how the ideas presented here can be extended to other transition-metal perovskite oxides.

The proximity to an electronic instability for $LaTiO_3$ is largely related to its orbital fluctuations, because it contains one $3d$ electron in triply degenerate t_{2g} states—considering only one spin orientation.[§] On the other hand, correlated systems that are perfectly half-filled are expected to be very stable Mott insulators. For example, $LaCrO_3$ (t_{2g}^3) has a sizeable band gap of 3.3 eV [2,38], and $BiFeO_3$ ($t_{2g}^3 e_g^2$) has a band gap of 2.7 eV [39].

Systems with one electron or hole in the doubly degenerate e_g band—e.g. high-spin d^4, low-spin d^7, and d^9—appear to fit the criterion of electronic states that are not exactly half-filled. However, such systems are also susceptible to Jahn-Teller distortions that favor the ordering of orbitals and in turn make a Mott insulating state stable. Such is the case for $LaMnO_3$ ($t_{2g}^3 e_g^1$). It is interesting that $LaNiO_3$ exhibits metallic behavior despite its low-spin d^7 configuration. As insulating phases are found in nickelates with

[§] In the limit of exceedingly weak correlations, the degeneracy of these states is 6, accounting for spin degeneracy.

smaller A-site rare-earth cations, it may be worthwhile to explore whether $LaNiO_3$ can be made insulating, i.e. undergo a metal-insulator transition, with the introduction of thin-film epitaxial strain.

Other materials with t_{2g} states that are not exactly half-filled may be on the brink of an insulator-metal transition and hence be suitable for tuning through heteroepitaxial strain; they include d^2, low-spin d^4, high-spin d^6, and high-spin d^7 systems. $LaVO_3$ is a $3d^2$ material, but it has a sizeable optical gap of about 1 eV [2,38]. This electronic excitation gap is likely related to the orbital ordering [40] that stabilizes its Mott insulating as well as its antiferromagnetic ground state. However, it may be possible to introduce thin-film strain to destabilize the orbital-ordered state and subsequently induce an insulator-metal transition.

To the author's knowledge, there is no low-spin $3d^4$ ABO_3 perovskite oxide, but $SrRuO_3$ is a low-spin $4d^4$ system. As a general rule, the electron bandwidth of and the energy splitting between t_{2g} and e_g states of 4*d* transition-metal oxides are greater—as a result of stronger hybridization between the transition-metal 4*d* orbitals, compared to the 3*d* orbitals, with the oxygen 2*p* orbitals. Despite both experimental [41] and theoretical [42] studies of strain-induced modification of the electronic and magnetic properties of $SrRuO_3$, it is not clear whether a metal-insulator transition is possible. There is still debate on whether electron-electron correlations are important in $SrRuO_3$ and in similar 4*d* oxide materials [43]. Nevertheless, a recent report of an insulating and perhaps antiferromagnetic phase induced in ultrathin $SrRuO_3$ films suggests the possible role of lattice distortions [44]. Thicker films become metallic.

$LaCoO_3$ is an example of a $3d^6$ system. It is close to a low-to-high spin transition that can be thermally activated [45]. In its low-spin state the t_{2g} band is completely filled, and not surprisingly it is insulating; furthermore, along with its transition to a high-spin state at higher temperatures ($t_{2g}^4 e_g^2$), it also becomes metallic. It would be interesting to explore whether a high-spin state can be stabilized and an insulator-metal transition be tuned at lower temperatures. Recent studies have shown that long-range magnetic ordering in epitaxial films may be linked to an intermediate spin state ($t_{2g}^4 e_g^2$) [46,47]. The films are ferromagnetic and insulating. Though not an insulator-metal transition, magnetic ordering in strained $LaCoO_3$ thin films is another example of the importance of epitaxial distortions in a material near an electronic or spin transition. But remarkably, according to the calculations of Rondinelli and Spaldin, a half-metallic *A*-type antiferromagnetic state is most stable for tetragonally strained $LaCoO_3$ [48].

To the author's knowledge, there is no high-spin d^7 ABO_3 perovskite oxide.

4.7. Concluding remarks

The work reported here provides an alternative explanation to the metallicity observed in $LaTiO_3/SrTiO_3$ heterostructures [1]. A detailed study suggests that metallicity in $LaTiO_3$ thin films on $SrTiO_3$ substrates is induced by epitaxial strain. As $LaTiO_3$ is a $3d^1$ system,

it has proved to be a good starting point for strain-controlled insulator-metal transitions. In fact, several other d^1 systems—e.g. $CaVO_3$, $SrVO_3$, and ReO_3—are metallic. The ability to maintain strain coherency in heteroepitaxial films enables the investigation of possible strain-induced electronic transitions based on rather simple ideas. In this particular example, the lattice state of a material that naturally has orbital degrees of freedom is modified.

There are many proposals of band offset engineering of Mott insulators; however, because many Mott insulators are also susceptible to orbital disorder, the effects of lattice distortions may prove to be critical. The challenge is to achieve engineering control within a single sample. Deposition on substrates with a strong piezoelectric response may be an avenue to control the electrical properties of the thin films.

Though there may be several opportunities to exploit heteroepitaxy to tune electronic transitions in single-valent transition-metal perovskite oxides, there is great potential in mixed-valent materials as well, as demonstrated in the following chapter.

Chapter 5

Strain-enhanced Magnetoresistance in $La_{2/3}Sr_{1/3}MnO_3$ films

5.1. Double exchange and ferromagnetism 59
5.2. Phase separation and it role in colossal magnetoresistance 60
5.3. General concept and scope of this work 65
5.4. Samples studied and their structures 66
5.5. Thin-film magnetism and magnetotransport 72
5.5.1. Electrical transport 72
5.5.2. Magnetism 73
5.5.3. Magnetotransport 74
5.6. The significance of strain coherency in (001) films 79
5.7. On the possibility of strain-induced phase separation 80
5.8. Can phase separation be tuned? 83
5.9. Conclusions and outlook 83

Since its discovery in lanthanum calcium manganites [1], the phenomenon of colossal magnetoresistance (CMR) continues to be of great scientific inquiry. The phase diagrams of chemically alloyed bulk crystals have been heavily investigated. Because of the strong dependence of the properties of many such correlated electron systems on their lattice states, epitaxial strain has been considered in lieu of chemical doping as a possible route of generating equally rich phase diagrams as seen in the bulk materials and to tune CMR in this class of materials. Thin-film properties that are distinct from bulk properties can be engineered if the critical parameters are identified and controlled. In this study, a more insulating low-temperature phase is shown to be induced in an otherwise very stable ferromagnetic metallic $La_{2/3}Sr_{1/3}MnO_3$—close to the optimal stoichiometry for the highest Curie temperature for an alloy of La and Sr. The stabilization of insulator/metal phase coexistence in a material, whose bulk is dominated by ferromagnetic double exchange, exemplifies the potential of exploiting epitaxial strain to design the magnetoresistive properties of thin-film manganites.

§ 5.1 Double exchange and ferromagnetism

In colossal magnetoresistive manganites $R_{1-x}A_xMnO_3$ (R = trivalent rare-earth metal, A = divalent alkaline-earth metal, and $0 \leq x \leq 1$), Mn cations have both t_{2g} and e_g electrons. There are 3 t_{2g} and $1-x$ e_g electrons per Mn. As introduced in Section 3.7.1, the Hubbard Hamiltonian demands antiferromagnetic coupling between two neighboring half-filled orbitals that hybridize. A description of the effects of orbital degeneracy on orbitals that are less than half-filled is presented in Section 4.1 to illustrate the antiferromagnetic instability of $LaTiO_3$, a $3d^1$ system. In $La_{2/3}Sr_{1/3}MnO_3$, each Mn has on average 3.67 electrons and a valence state of 3.33+. Disregarding the noncubic distortions, 0.67 electrons occupy two degenerate e_g states. Electrons in the t_{2g} levels are assumed to be extremely localized, and the e_g states are more hybridized. A model Hamiltonian relevant for this system is as follow [2]:

$$H = -\sum_{i,j,\sigma} t_{ij}\left(c_{i\sigma}^{\dagger}c_{j\sigma} + c_{j\sigma}^{\dagger}c_{i\sigma}\right) - \frac{1}{2}J_H \sum_{i,\sigma,\sigma'} \boldsymbol{S}_i \cdot c_{i\sigma}^{\dagger}\,\boldsymbol{\sigma}_{\sigma\sigma'}c_{i\sigma'} + U\sum_i n_{i\uparrow}n_{i\downarrow} + J\sum_{i,j}\boldsymbol{S}_i \cdot \boldsymbol{S}_j$$

where t_{ij} is the transfer integral between the e_g states of cations i and j, $c_{i\sigma}^{\dagger}$ and $c_{i\sigma}$ are the creation and annihilation operators for an e_g electron in ion i, $\boldsymbol{S}_i$ is the total spin of the three t_{2g} electrons in each ion ($|\boldsymbol{S}_i| = 3/2$ for all i), $\boldsymbol{\sigma}$ are the Pauli spin matrices, U is the on-site potential for t_{2g} states, n is the number operator for t_{2g} electrons, and J is the superexchange energy of the t_{2g} states. The hybridization of the t_{2g} electrons is not explicitly taken into account because it is assumed that the on-site potential of the t_{2g} states (U) is much greater than its transfer integral. Therefore, the t_{2g} states have a very stable configuration of three electrons with their spins aligned to the same direction due to Hund's coupling. Orbital overlap between adjacent t_{2g} states is hidden in the $J\,\boldsymbol{S}_i \cdot \boldsymbol{S}_j$, the superexchange term, as discussed in Section 3.7 and Appendix A.3.

Shown in Fig. 5.1 is a schematic of the transfer of an e_g electron from Mn^{3+} to an adjacent Mn^{4+} ion. Often, the orbital degeneracies of the t_{2g} and e_g states are disregarded in the modeling, and the states are replaced by a nondegenerate upper and lower levels (Fig. 5.1b). The effects of orbital degeneracy of the e_g states are discussed in detail in the next section. The charge in the lower energy level carries a spin S = 3/2. One can also see that if J_H is large enough, which is assumed to be the case, the delocalization of the e_g electron demands that adjacent magnetic cations be aligned parallel to each other, which constitutes the mechanism for double-exchange ferromagnetism [3,4]. For the manganites, it is often assumed that not only J_H is large, but so is U; the assumptions are a statement of the application of Hund's rules on each cation and large on-site repulsion on the t_{2g} states that ensures exactly half filling of parallel spin electrons, validating the single spin S=3/2 approximation. The superexchange interaction between t_{2g} electrons of adjacent cations will most assuredly be antiferromagnetic. Therefore, the antiferromagnetic coupling between the localized t_{2g} competes with the ferromagnetic coupling arising from the e_g electrons that can delocalize. For certain manganites, the two interactions are comparable in strength, and their competition is believed to be the underlying ingredient for colossal magnetoresistive properties. The relevant part of the Hamiltonian for this problem consists of these two terms, and can be written as:

$$H' = -\sum_{i,j} t_{ij}^{eff}\left(c_i^{\dagger}c_j + c_j^{\dagger}c_i\right) + J\sum_{i,j} \boldsymbol{S}_i \cdot \boldsymbol{S}_j$$

where

$$t_{ij}^{eff} = t\cos\frac{\theta}{2}$$

and θ is the angle between $\boldsymbol{S}_i$ and $\boldsymbol{S}_j$. Whereas first term represents double exchange and favors ferromagnetic alignment of moments, the second terms represents superexchange the favors antiferromagnetic alignment of moments. The competition between hybridization-induced delocalization of e_g electrons and superexchange coupling between localized t_{2g} electrons is quantified by the magnitudes of t and J in mixed-valent manganites.

§ 5.2 Phase separation and it role in colossal magnetoresistance

A canted spin structure may appear to be the most reasonable moment configuration exhibited by the mixed-valent manganites owing to the competing ferromagnetic and antiferromagnetic interactions. However, it be can shown that based solely on the double exchange Hamiltonian used by deGennes [4], a single-phase canted magnetic state, with two sublattices of opposite canting orientations, is unstable with respect to phase separation; in particular, Kagan *et al.* showed that a canted spin state at both low hole concentrations (small x in $La_{1-x}A_xMnO_3$ where A = alkaline-earth metal) as well as low electron concentrations has negative electronic compressibility [5]:

$$\kappa = \left(\frac{d^2E}{dn^2}\right)^{-1}$$

where E is the total energy of the system and n is the hole (or electron) concentration. Note that in their simplified model calculations, there is electron-hole symmetry; that is $La_{1-x}A_xMnO_3$ is expected to behave as $La_xA_{1-x}MnO_3$. The system is therefore unstable with respect to the spontaneous formation of hole-rich ferromagnetic regions and hole-poor antiferromagnetic regions. This can be viewed as the electronic analog to chemical spinodal decomposition. Although Kagan *et al.*'s study, based solely on the double exchange Hamiltonian, is definitely insufficient to describe all of the phenomenology of manganites, it does bring to bear their tendency toward carrier phase separation.* It is generally believed that this type of phase coexistence of carrier-rich and carrier-poor regions should be on the nanoscale, because Coulomb interaction will make larger phase separated regions unstable. However, it has been observed that certain manganites can exhibit mesoscopic phase separation [6]. Here, *nanoscale* refers to within a few lattice constants, or ~1 nm, and *mesoscale* refers to any bigger scale, up to the micrometer range.

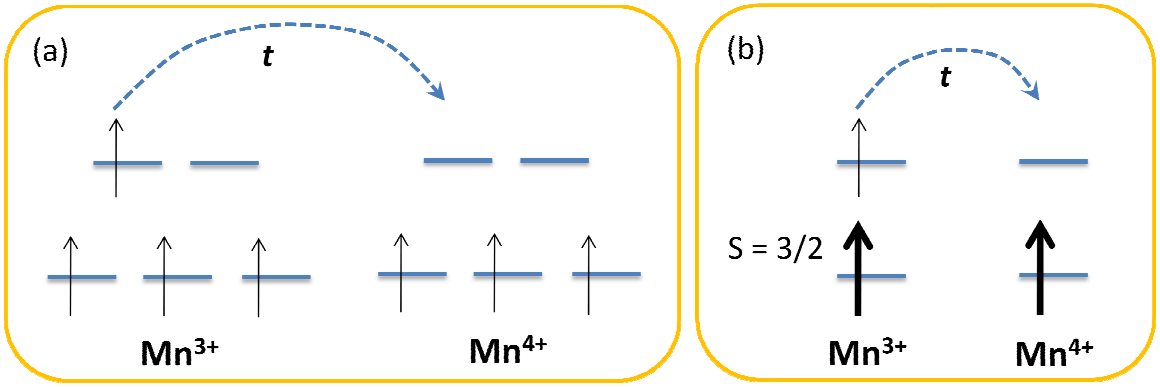

Figure 5.1. (a) Schematic of the energy levels of adjacent Mn^{3+} and Mn^{4+} cations and the hopping of the e_g electron from Mn^{3+} to Mn^{4+} with amplitude t. (b) Simplified picture of the same hopping mechanism, disregarding the orbital degeneracy of the lower t_{2g} and the upper e_g levels. A single spin S = 3/2 in the lower energy state is used to replace the three parallel electrons of the half-filled t_{2g} levels. It is assumed that the t is large enough to lead to ferromagnetic alignment of adjacent moments that is mediated by the delocalization of the higher-energy electron.

In real manganites $R_{1-x}A_xMnO_3$ (R = trivalent rare-earth metal; A = divalent alkaline-earth metal), the electronic properties are determined jointly by electronic band filling, which is governed by the ratio between rare-earth and alkaline-earth ions, and

* Although it is typical in literature to use the term "electronic phase separation," the author believes that "carrier phase separation" is a more unambiguous term for this specific case, because other works have shown two phases with the *same carrier density*, ferromagnetic and antiferromagnetic or metallic and insulating phases, can likewise coexist. Whereas in such a scenario, the electronic properties of the two comprising phases differ, their carrier densities do not. Electronic phase separation (or just phase separation) will be more generally used to refer to scenarios with or without carrier separation.

bandwidth, which in bulk materials is governed mainly about the average ionic size of the rare-earth and alkaline-earth ions. Therefore tunability of bulk manganites can be achieved through a combination of aliovalent and isovalent substitution of La in the parent material $LaMnO_3$.

Considering that the mixed valence of Mn is dependent on alloying, the effects of chemical disorder from alloying is important; disorder turns out to be of crucial importance to metal/insulator or ferromagnetic/antiferromagnetic phase separation with both phases containing the *same* carrier density [7,8]. Using Monte Carlo simulations, Moreo *et al*. showed that though a mixed-valent manganite in the clean limit is unstable to carrier spinodal decomposition for $0 \lesssim x < 0.25$, this is not the case when disorder is taken into account [7]. The superexchange energy is very sensitive to local chemical bonding changes and so is double exchange. Therefore, having randomly dispersed A-site cations from alloying not only can bring about a change in the Mn valence state, but also can cause small yet consequential fluctuations in magnetic exchange due to the variance of local bonds. Using a combination of different A-site cations, Kundu *et al*. studied the effects of the variance in A-site cation size while keeping the average radius constant; they found that disorder, resulting from a distribution in A-site cation sizes, does indeed profoundly change the magnetic and transport properties of their crystals [9]. Disorder induced by size differences is commonly quantified by the Attfield parameter, which is the square of the variance of the A-site ionic radius. Moreo *et al*. handled the problem by including a random field term on each lattice site in the Ising model, rather than taking into account the fluctuations directly into the exchange integral [7]. From the spatial mapping of average nearest-neighbor spin-spin correlation, it was found that ferromagnetic/antiferromagnetic phase coexistence is possible with random fields, without carrier separation. This description is more amenable to phase separation in the mesoscopic scale, up to even the micrometer scale, as there is not a Coulomb energy penalty that would arise from charge separation. Recent work on digital superlattices of alternating layers of $LaMnO_3$ and $SrMnO_3$ films, mimicking the chemically clean limit, will certainly give further insight to the role of disorder in phase separation and ultimately CMR in the manganites [10].

Metal/insulator coexistence in both the nanoscopic [7,11] and mesoscopic [6,7,12-14] scales may be important to the CMR phenomenon. If a particular manganite is at or near a two-phase coexistence state, metamagnetic transitions induced by a magnetic field may become relevant and be responsible for CMR. Metamagnetic transitions are especially prominent in lower electronic bandwidth manganites such as $Pr_{1-x}Ca_xMnO_3$ and $Nd_{1-x}Ca_xMnO_3$ [15].

It appears that the separation and coexistence of distinct electronic phases are a natural result of model Hamiltonians widely used to describe manganites. However, the phenomenology may perhaps be even more commonplace in correlated electron systems. Experimentally, magnetic/superconducting phase coexistence has been observed both in superoxygenated $La_{2-x}Sr_xCuO_{4+y}$ [16] and underdoped $Ba_{1-x}K_xFe_2As_2$ [17]. Though the strength of electron correlations in the iron pnictides is still debated, they certainly play a prominent role in the cuprates. Different phenomena that may arise from electronic phase-separated states are of much current interest.

Understanding and ultimately engineering the CMR effect in manganites remains an active area of research. It is generally believed that phase separation does play a role in CMR, but there is no universally accepted explanation. Because of the degeneracy of the e_g level, there is an orbital degree of freedom that is not fully captured in the aforementioned studies [18]. In fact, when there is exactly one electron in the doubly degenerate e_g levels, as is the case with the parent material $LaMnO_3$, the system is extremely Jahn-Teller active. Jahn-Teller distortions refer to deformation of each $MnO_{6/2}$ octahedron, and are independent from octahedral rotations that are discussed in Section 3.2.[†] A type of collective Jahn-Teller distortion of the $MnO_{6/2}$ octahedra was proposed by Kanamori [19][‡] and experimentally verified by Proeffen *et al.* in $LaMnO_3$ [20]. A schematic collective distortion on the *x-y* plane is shown in Fig. 5.2. The result is orbital ordering of the e_g electrons into x^2-z^2 and y^2-z^2 orbitals: the e_g electrons of adjacent Mn^{3+} sites in an *x-y* plane occupy alternating orbitals, and along the *z* direction they occupy the same orbital [21], as shown in Fig. 5.3. The numbering of the sites and orbitals in Figs. 5.2 and 5.3 show the correspondence between the lattice and orbital states. The reduction in crystal symmetry, leads to a rehybridization (different linear combinations) of the familiar x^2-y^2 and $3z^2$-r^2 orbitals:

$$x^2 - z^2 = \frac{1}{2}(Y_2^2 + Y_2^{-2}) - \frac{1}{\sqrt{2}}Y_2^0 \propto (x^2 - y^2) - (3z^2 - r^2)$$

$$y^2 - z^2 = \frac{1}{2}(Y_2^2 + Y_2^{-2}) + \frac{1}{\sqrt{2}}Y_2^0 \propto (x^2 - y^2) + (3z^2 - r^2)$$

where the Y_l^m's are the spherical harmonics. Because of the Jahn-Teller origin of orbital ordering, it is necessarily associated with the collective lattice distortion. Furthermore, the orbital ordering explains the *A*-type antiferromagnetic ordering in $LaMnO_3$. The staggered in-plane orbital ordering leads to in-plane ferromagnetic coupling (see Section 3.7.2 and Appendix A.3 for details). There is some discrepancy on the ordering of the orbitals along the *z* axis, whether they repeat the same *x-y* pattern [21] or are staggered along adjacent *x-y* planes [22]. Nonetheless, the preferential arrangement of e_g electron density in the *x-y* planes makes the superexchange coupling of half-filled t_{2g} orbitals the most dominant interplanar exchange interaction—hence, antiferromagnetic coupling. All in all, the manganites are indeed an exemplary model system of the strong coupling among the charge, lattice, orbital, and spin states.

Given that orbital degeneracy is important, in ferromagnetic alloyed manganites, the competition between double exchange and Jahn-Teller distortions are thought to result in large MR observed near the magnetic transition [23,24]. Experimentally, it is seen that associated with the magnetic transition, there is a reduction in octahedral symmetry of the $MnO_{6/2}$ cages manifested above the Curie temperature [25], as one would expect for a Jahn-Teller distortion. Furthermore, there are suggestions that phase

[†] Though octahedra rotations do occur in $LaMnO_3$, the primary lattice effect is deformation of each octahedron, which reduces the Mn-site symmetry.

[‡] Although Kanamori used MnF_3 instead of $LaMnO_3$ as an example, the important aspect is that both materials have octahedral Mn^{3+} cations, which are extremely Jahn-Teller active [19].

coexistence of a metallic ferromagnetic state and a more insulating paramagnetic state is also essential for explaining the temperature- [26,27] and field-dependent resistivity [26] of ferromagnetic manganites.

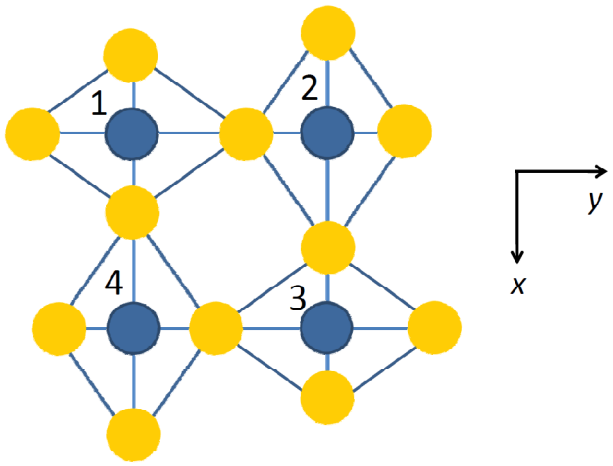

Figure 5.2. The collective Jahn-Teller distortion in the *x*-*y* plane exhibited by $LaMnO_3$. Adapted from Refs. [19,20].

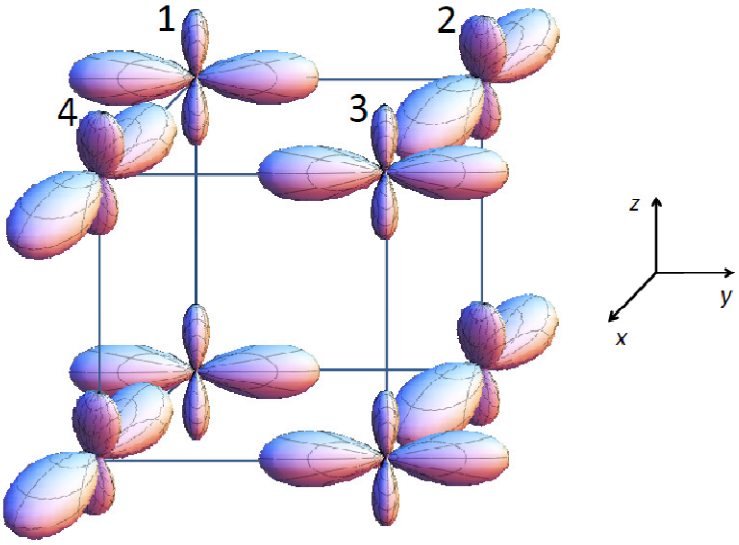

Figure 5.3. Schematic of the orbital ordering of the one e_g electron per Mn site in $LaMnO_3$. Adjacent orbitals in the *x*-*y* plane are staggered alternating between x^2-z^2 and y^2-z^2. The pattern is repeated in the *z* direction.

In manganites with relatively small electronic bandwidths, a charge-ordered-to-ferromagnetic transition can be induced by both temperature and magnetic field [8,26,28] particularly near the 50:50 rare-earth/alkaline-earth composition. In these

cases, the high MR values can be observed at temperatures well below the Curie temperature or charge ordering temperature. It is important to distinguish the measured MR into two categories: that near the magnetic transition and that well below the ordering temperature(s). Most can agree that a low-temperature metallic state in the manganites must arise from ferromagnetic double exchange. But both antiferromagnetic superexchange exchange and Jahn-Teller distortions favor the single occupancy of e_g states. This commonality has made the determination of "the correct mechanism" of CMR more challenging [29]; different mechanisms may be relevant within a single sample, but their comparative importance may vary with temperature.

§ 5.3 General concept and scope of this work

This work is motivated in part to shed light on the potential of using heteroepitaxial strain in manganite thin films in lieu of chemical doping to generate rich phase diagrams of a variety of magnetically ordered states. However, the work is more particularly aimed at examining how MR can be engineered in strained manganite thin films. The material of choice is $La_{2/3}Sr_{1/3}MnO_3$, which in the bulk has a Curie temperature of about 355 K and a saturated magnetization of about 590 emu/cm^3. For the manganites, the Curie temperature is fairly high, signifying that double exchange dominates superexchange for this particular composition. Also, the kinetic energy of the mobile e_g electrons overwhelms the propensity of Jahn-Teller distortions up to the relatively high Curie temperature. Its Attfield parameter is small, 8.9×10^{-5} Å^2 based on Pauling ionic radii; in comparison, the commensurately charge-ordered $La_{1/2}Ca_{1/2}MnO_3$, which is susceptible to phase separation, has an Attfield parameter of 6.4×10^{-3} Å^2. $La_{2/3}Sr_{1/3}MnO_3$ has received interest as a half metal, as it has only conduction electrons of majority spin, and therefore a viable electrode in all-oxide magnetic tunnel junctions [30-34]; however, it is not particularly interesting within the manganites as a CMR material in itself.

Though bulk $La_{2/3}Sr_{1/3}MnO_3$ is not near any ferromagnetic/charge-ordered or any low-temperature metal/insulator phase boundary, this investigation is focused on whether the material can be brought closer to a phase boundary through lattice distortions. A low-temperature insulating state has been stabilized in coherently strained films, and indirect evidence from magnetism and transport data points to metal/insulator coexistence. Selecting a starting material that is a stable ferromagnet in the bulk fully illustrates the potential for using epitaxial strain to tune the electronic properties and possible phase coexistence in related manganites. From the discussion in the previous two sections, it is not surprising that thin-film lattice strain can profoundly change the electronic state of manganite films. In bulk $La_{0.75}Ca_{0.25}MnO_3$, it is shown that a ferromagnetic-to-antiferromagnetic transition can be traversed with the application of uniaxial stress using a diamond anvil cell [35]. However, heteroepitaxy provides an ideal and vast platform to routinely realize more strain and therefore thoroughly investigate the effects of lattice deformation.

There have been some studies in strained $La_{2/3}Sr_{1/3}MnO_3$ films that have suggested phase coexistence wherein charge localization is induced by heteroepitaxial lattice deformation [36-38], and the stabilized insulating phases have been shown to persist at low temperatures, well below the Curie temperature [36,38-41]. Similar findings were reported in the $La_{2/3}Ca_{1/3}MnO_3$ thin films [42,43]. Several studies have concentrated only on the effect of lattice distortions on the Curie temperatures of $La_{2/3}Sr_{1/3}MnO_3$ films and not explored the magnetotransport properties [44-46].

Heteroepitaxial lattice distortions can be exploited as a means to change electronic bandwidth and thereby tune the magnetic ordering and CMR effect of these materials. The interdependence of magnetic ordering and electrical transport in the thin films is emphasized. Manipulating phase coexistence in $La_{1-x}Sr_xMnO_3$ thin films to achieve desired magnetoresistive properties is a promising route for materials design; the dual goals in this study are to increase MR as well as broaden the temperature range in which high MR is observed.

§ 5.4 Samples studied and their structures

$La_{2/3}Sr_{1/3}MnO_3$ films were deposited on (001), (110), and (111) $LaAlO_3$ substrates at 700 ^oC and in 300 mTorr of oxygen by pulsed-laser deposition. The laser pulse rate was 10 Hz. The deposited films were cooled from 700 ^oC to room temperature in 300 Torr of oxygen. The pseudocubic lattice constant is 3.88 Å for $La_{2/3}Sr_{1/3}MnO_3$ and 3.79 Å for $LaAlO_3$. In each deposition a substrate of every orientation is loaded, and films of the different orientations are grown simultaneously. Rutherford backscattering spectrometry was used to measure the thicknesses of the films. It was seen that within the same deposition, the film thicknesses on differently oriented $LaAlO_3$ substrates were the same—to within the error of the measurement. This chapter will be focused on 34 nm thick films, but data of an additional 45 nm (001) film will be shown. The magnetism, electrical transport at zero magnetic field, and magnetotransport properties of the films on the three $LaAlO_3$ substrates of different orientations will be compared with one another and correlated with their respective lattice strain states. Atomic structures and microstructures of the films were studied with four-circle x-ray diffraction.

Representative atomic force microscopy images, Fig. 5.4, reveal that the (001) film is the smoothest with a typical root mean squared roughness of ~1 nm. This finding is typical for films thicknesses less than 100 nm. In order to prevent equilibrium faceting of the surfaces of the (110) and (111) films to lower energy {001} planes, the films were grown at 10 Hz pulse rate, a relatively high rate for pulsed laser deposition. As a result, films of reasonable smoothness, with root mean squared roughness values $\lesssim$ 2 nm, can be attained on all substrate orientations, as can be seen in the atomic force microscopy images. Decreasing the deposition temperature can also reduce surface faceting by limiting surface diffusion, but it also generally results in lower thin-film crystallinity.

X-ray diffraction 2θ and ω scans of the out-of-plane reflections were performed on the films on the three different substrates. Figure 5.5a, 2θ scans with $\omega = 2\theta/2$, show

that the films grow in the same orientation as the substrates for all three substrates. The ω scans of the out-of-plane film peaks are taken with ω being the angle between the incident beam and various in-plane directions for each sample by changing the angle ϕ. In Fig. 5.5b, the (001), (110), and (111) substrates are aligned such that ω is the angle between the x-ray beam and the [100], [1-10], and [-1-12] in-plane directions respectively, which correspond to the $\phi = 0^{o}$ orientations for each sample. Rocking curve ω scans of out-of-plane reflections yield the in-plane breadth of reciprocal lattice points. For all ϕ, the full-width at half-maximum values of out-of-plane reflections are smaller in the (001) and (110) films than in the (111) film, thus indicating higher crystalline quality in the (001) and (110) films.

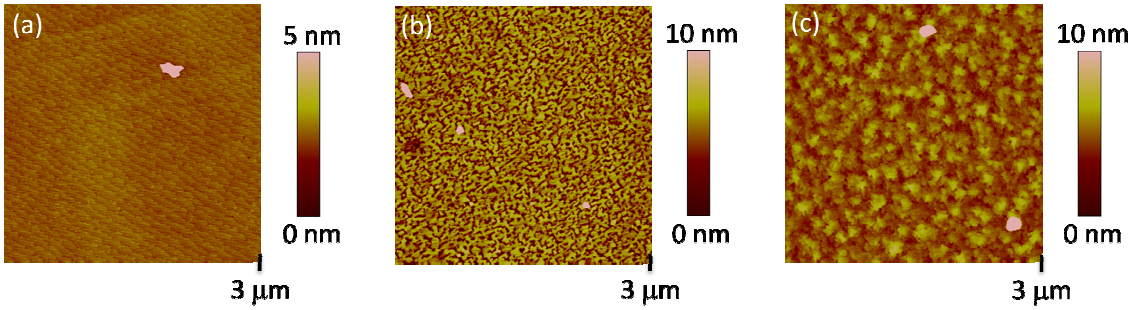

Figure 5.4. Atomic force microscopy images (3 μm × 3 μm) of 25 nm $La_{2/3}Sr_{1/3}MnO_3$ films on (a) (001), (b) (110), and (c) (111) $LaAlO_3$ substrates.

Reciprocal lattice maps of the 103 reflection of the (001) film, the 221 and 310 reflections of the (110) film, and the 312 reflection of the (111) film were taken to determine the in-plane (in)coherency between the film and substrate (Fig. 5.6). From Fig. 5.6a, it is seen that the (001) film is strained coherently in plane. The thin-film distortion is tetragonal. The (110) film is coherently strained along the in-plane [001] direction (Fig. 5.6c), but is almost fully relaxed along the [1-10] direction (Fig. 5.6d). The (111) film is nearly completely relaxed in the plane of the film (Fig. 5.6b), and the (111) interplanar spacing is found to be almost the equal to that of the bulk (Table 5.1). It appears that coherent strain can be more easily maintained if the stress is applied along a direction of only principal components, but structural relaxation occurs more readily when the stress is applied along a direction with both principal and shear components. Structural relaxation due to substrate/film incoherency is the greater in the (111) film, which also has the largest full-width at half-maximum value in the ω scan (Fig. 5.5 and Table 5.1).

In bulk $La_{2/3}Sr_{1/3}MnO_3$ noncubic lattice distortions is driven by partially unfilled Mn e_g states, or the Jahn-Teller effect. On the other hand, in thin films the noncubic distortions that can arise from heteroepitaxy are not electronically induced. The reciprocal lattice maps in Fig. 5.6 allow for the determination of the strain tensors for the (001) and (110) deformed films, and the distortions are defined with the reference structure of a cubic perovskite with a lattice parameter of 3.88 Å.

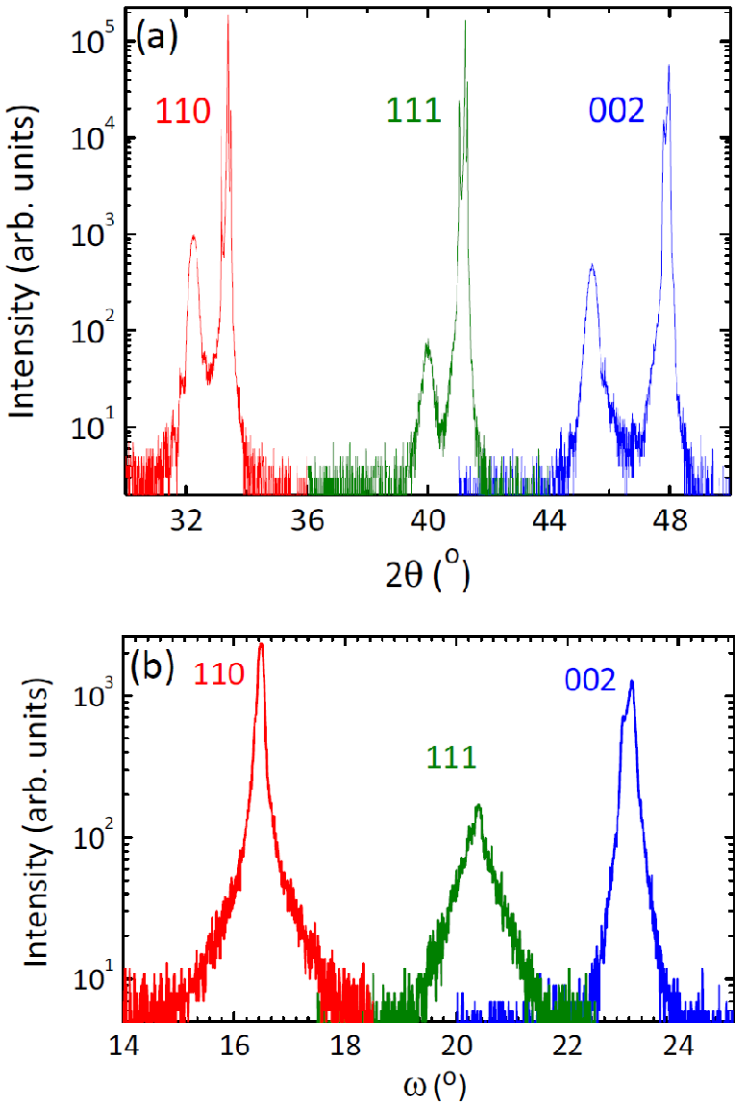

Figure 5.5. (a) 2θ and (b) ω scans of the out-of-plane reflections of the (001), (110), and (111) films.

The strain tensor of the (001) film is

$$\boldsymbol{\varepsilon}^{(001)} = \begin{bmatrix} -2.32 & 0 & 0 \\ 0 & -2.32 & 0 \\ 0 & 0 & 2.76 \end{bmatrix} \%$$

The tensor can be decomposed into components that represent the volume dilation and tetragonal (or more generally, orthorhombic) distortion:

$$\boldsymbol{\varepsilon}^{(001)} = -0.63 \begin{bmatrix} 1 & 0 & 0 \\ 0 & 1 & 0 \\ 0 & 0 & 1 \end{bmatrix} \% + \begin{bmatrix} -1.69 & 0 & 0 \\ 0 & -1.69 & 0 \\ 0 & 0 & 3.39 \end{bmatrix} \%$$

Similarly, the strain tensor of the (110) film is

Table 5.1. Properties of the heteroepitaxial 34 nm (001), (110), and (111) films. The saturated magnetic moment (M_S) is measured at 7 K, MR at 10 K and 50 kOe, and resistivity (ρ) at 10 K. *d* refers to the spacing between (*hkl*) planes for the corresponding (*hkl*) films, and the interplanar spacings are compared to those of the bulk. Bulk interplanar spacing values are calculated using a pseudocubic lattice parameter of 3.88 Å. The measured full-width at half-maximum (FWHM) values are from ω scans in Fig. 5.5b.

Sample	T_c (K)	M_S (μ_B/Mn)	MR (%)	ρ (mΩ·cm)	ρ_{273K} / ρ_{10K}	d_{film}(Å)	d_{bulk}(Å)	FWHM (°)
(001)	325	2.49	-65	1.69	2.92	3.99	3.88	0.18
(110)	334	3.48	-10	0.227	8.04	2.77	2.745	0.11
(111)	347	3.53	-1	0.117	7.81	2.25	2.24	0.33

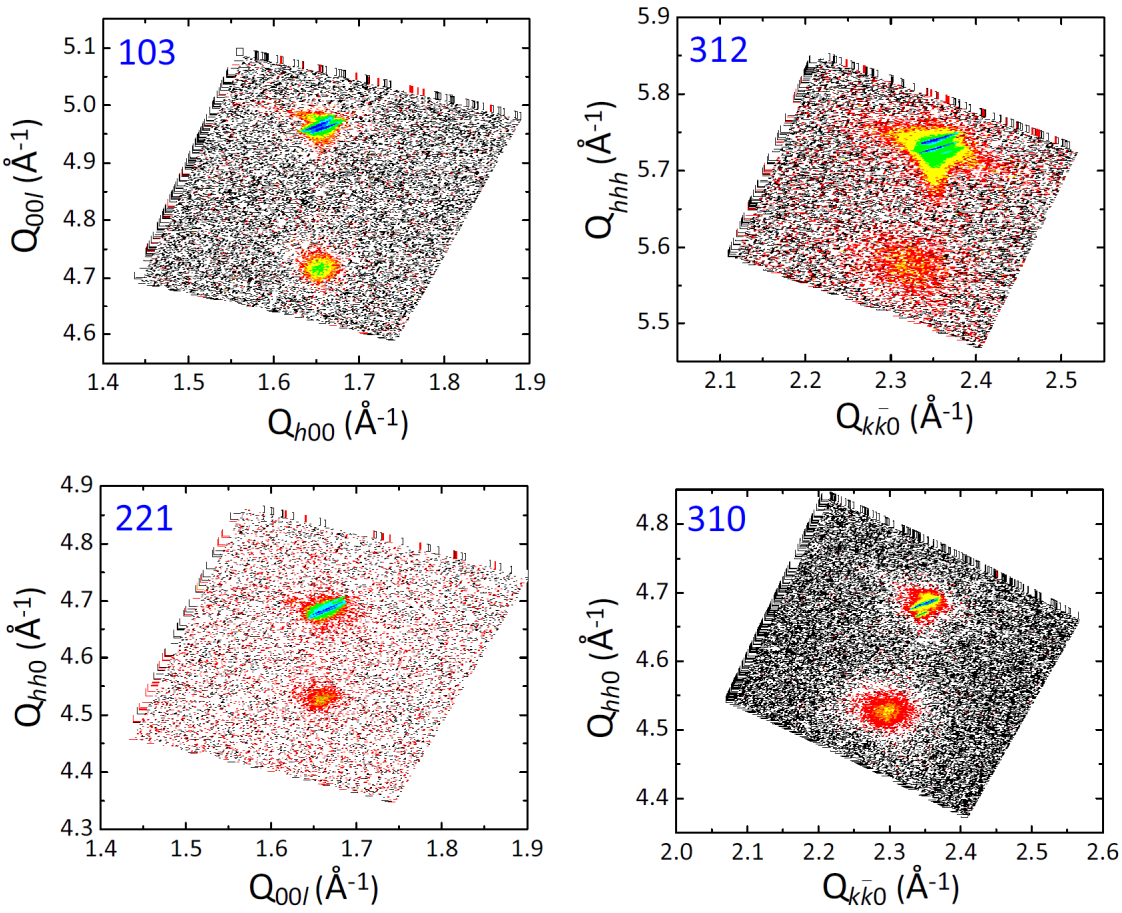

Figure 5.6. Antisymmetric (ω ≠ 2θ/2) x-ray diffraction scans of the (a) 103 reflection of the (001) film, (b) the 312 reflection of the (111) film, (c) the 221, and (d) 310 reflections of the (110) film. Reciprocal space coordinates Q is defined as 2π divided by real space distance.

$$\boldsymbol{\varepsilon}^{(110)} = \begin{bmatrix} 0.31 & 0.64 & 0 \\ 0.64 & 0.31 & 0 \\ 0 & 0 & -2.32 \end{bmatrix} \%$$

which can be decomposed into

$$\boldsymbol{\varepsilon}^{(110)} = -0.57 \begin{bmatrix} 1 & 0 & 0 \\ 0 & 1 & 0 \\ 0 & 0 & 1 \end{bmatrix} \% + \begin{bmatrix} 0.88 & 0 & 0 \\ 0 & 0.88 & 0 \\ 0 & 0 & -1.75 \end{bmatrix} \% + \begin{bmatrix} 0 & 0.64 & 0 \\ 0.64 & 0 & 0 \\ 0 & 0 & 0 \end{bmatrix} \%$$

and the last component represents shear strain. The breadth of the 312 reflection of the (111) film, which may be caused by low-angle grain boundaries or inhomogenous lattice relaxation, makes it difficult to extract such information about that sample. All in all, both the out-of-plane 2θ scan and the reciprocal lattice map scans do suggest that the (111) film is almost fully relaxed.

It is well known that $LaAlO_3$ crystals are not perfectly cubic; they are rhombohedral ($\alpha = \beta = \gamma \neq 90^o$) with angles between lattice vectors of roughly 90.083 to 90.096°, depending on reference source [47,48]. X-ray diffraction shows that $La_{2/3}Sr_{1/3}MnO_3$ films on $LaAlO_3$ can be coherently or partially strained depending on substrate orientation; therefore, on certain substrates, the films may also have the rhombohedral symmetry and twin boundaries that result from the lowered symmetry.

Reduction of symmetry from cubic to rhombohedral, which occurs at about 800 K in bulk crystals [49], takes the form of negative shear strain represented by the following strain tensor as defined with respect to the cubic reference [48]:

$$\begin{bmatrix} 0 & -\varepsilon & -\varepsilon \\ -\varepsilon & 0 & -\varepsilon \\ -\varepsilon & -\varepsilon & 0 \end{bmatrix}$$

The rhombohedral distortion can be thought of as a shortening of the [111] axis as a result of shear strain. However, the shortened axis can be any one in the <111> family, shown in Fig. 5.7a. Two crystal domains can join to form twin boundaries, which is a common planar defect in rhombohedrally distorted crystals because there is a mirror plane symmetry element on the boundary—a symmetry element lost upon the cubic-to-rhombohedral transformation. Shown in Figs. 5.7b and 5.7c are schematics of (110) and (010) twin boundaries respectively. Different combinations of twin domains and their corresponding boundaries planes are discussed by Bueble *et al.* [48]. Despite the noncubic distortions, the Miller index directions and planes are still in reference to the pseudocubic lattice.

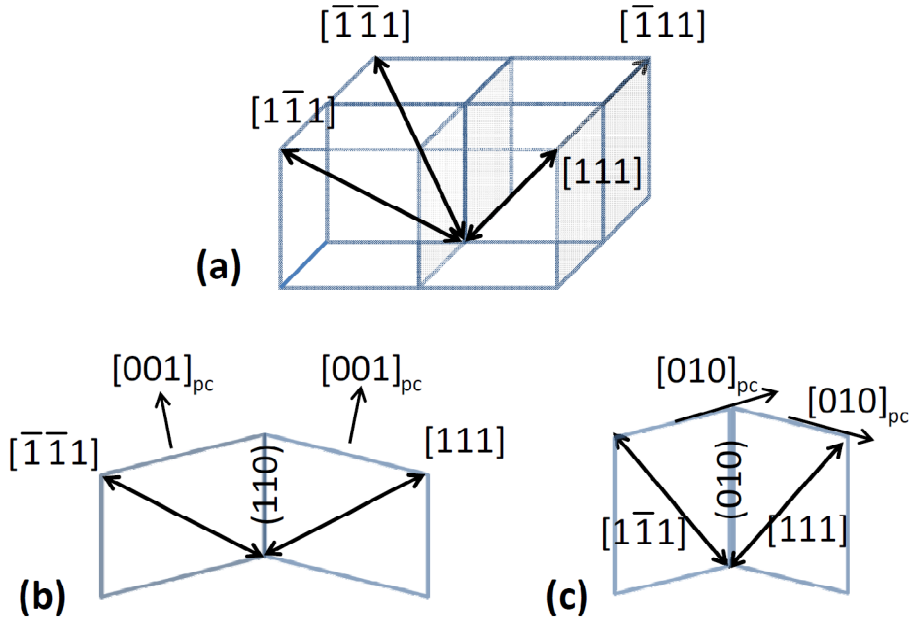

Figure 5.7. Schematics showing the (a) different possible shortened <111> axes of a rhombohedrally distorted structure and (b) (110) and (c) (010) twin boundaries formed by different rhombohedral domains. The pseudocubic (pc) Miller indices for directions and planes are kept.

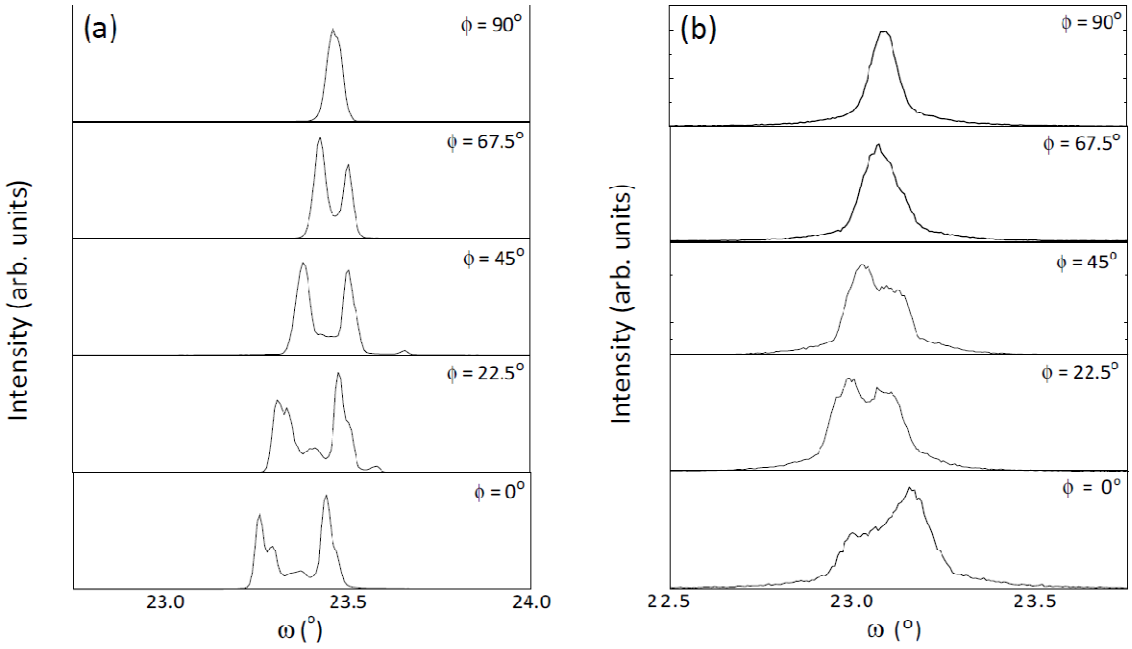

Figure 5.8. ω scans at different ϕ angles of the 002 reflection for (a) a (001) $LaAlO_3$ substrate and (b) an overlying 34 nm $La_{2/3}Sr_{1/3}MnO_3$ thin film.

Further investigation on the effects of twin boundaries in the substrates on film growth can be attained with ω scans of the 002 reflection of the (001) $La_{2/3}Sr_{1/3}MnO_3$ film along different ϕ angles, which allow for scanning different line sections of the reciprocal lattice spot. Figure 5.8 contains ω scans of both the 002 substrate and film reflections. In the scan of the substrate, the double peak observed in the substrate for $\phi = 0^o$ and the eventual disappearance for $\phi = 90^o$ are indicative the twin boundaries run mainly along one in-plane direction—[010] in the coordinate system used here—and there are two prominent reflection spots in the ω scan along the [100] direction ($\phi = 0^o$) as a result of twinning. Along intermediate ϕ values, the ω scans runs through the two reflection spots from different orientations, resulting in the gradual merging of the peaks as ϕ is increased. This observation should not be mistaken for twin boundaries of different misorientation angles along all in-plane directions. The same measurements of the 002 reflection of the film tell a similar story, revealing that the film is oriented with the substrate plane even across twin boundaries. From the scan of the substrate at $\phi = 0^o$, there are two distinct twin orientations separated by a (010) twin boundary. Calculations do show that {100} boundaries are lower in energy than {110} boundaries for $LaAlO_3$ [50].

The angle between the reflection peaks of the two twin orientations of the $LaAlO_3$ substrate is $\Delta\omega = 0.182^o = 3.2\times10^{-3}$ radians, and the corresponding shear strain element of each twin with respect to the cubic reference is 0.16%, roughly as is expected for a $LaAlO_3$ crystal. One can also consider Δω is the shear strain component across the twin boundary, from one twin to another. From the ω scan of the film at $\phi = 0^o$, it appears that $\Delta\omega = 0.155^o = 2.7\times10^{-3}$ radians, though the in-plane mosaic spread makes it difficult to ascertain an exact number. A comparison of the strain associated with the rhombohedral distortion to the heteroepitaxial strain observed in the films, quantified by magnitude of the elements in the aforementioned $\boldsymbol{\varepsilon}^{(001)}$ and $\boldsymbol{\varepsilon}^{(110)}$ tensors, suggests that indeed heteroepitaxial lattice distortions arising from the lattice mismatch between $La_{2/3}Sr_{1/3}MnO_3$ and $LaAlO_3$ should be much more important.

§ 5.5 Thin-film magnetism and magnetotransport

5.5.1 Electrical transport

One expects the hybridization of the e_g states to be extremely dependent on changes in bonding; therefore, the effects of heteroeptiaxial strain on electrical transport are investigated. The $La_{2/3}Sr_{1/3}MnO_3$ films grown on (110) and (111) substrates show metal-like temperature-dependent resistivity up to 385 K, the highest temperature measured (Fig. 5.10b); the bulk phase of this stoichiometry likewise shows a ferromagnetic metal-to-paramagnetic metal transition. However, the (001) film exhibits insulator-like

behavior at high temperatures, and the resistivity maximum at 290 K resembles that of a metal-insulator-like transition.

The transport properties at low temperatures are even more drastically different; the low-temperature resistivity of the (001) film is about an order of magnitude larger than those of the (110) and (111) films. The resistivity values at 10 K along with the resistivity ratio between the 273 and 10 K values (ρ_{273K}/ρ_{10K}) of the films are tabulated in Table 5.1. In correlation with the x-ray diffraction data, it is not surprising that the (110) film with the sharpest peak in the ω scan also has the highest resistivity ratio. However, the resistivity ratio of the (111) film, despite its broad diffraction spots, is much higher than that of the (001) film. Furthermore, the (111) is the most conductive, although atomic force microscopy images show that the (001) film is the smoothest, shown in Fig. 5.4. Therefore, microstructural defects do not appear to be the primary cause of the reduced conductivity exhibited by the (001) film. In fact according to the ω scan full-width at half-maximum values of the out-of-plane peaks, it can be concluded that the (111) film has the largest crystalline mosaic spread and hence highest degree of structural defects; yet it has the highest conductivity over the entire temperature regime measured. It appears that atomic lattice distortions in the coherently strained (001) film must reduce the electronic bandwidth of the e_g states and therefore result in lower conductivity.

5.5.2 Magnetism

As charge delocalization of e_g electrons is intimately connected to ferromagnetism in a double-exchange ferromagnet, the magnetic behavior of the films are investigated. The magnetic measurements presented here were performed along magnetically easy directions. The (001) film has an easy direction of [001], the (110) film has an easy direction of [1-10], and the (111) film has an easy plane of (111). Magnetic hysteresis loops of the samples at 7 K were taken along their respective easy directions (plane), shown in Fig. 5.9, and they reveal a larger hysteresis for the (001) film as well as a suppressed saturation magnetization of 401 emu/cm^3, or ~2.5 μ_B per Mn, at 7 K. Saturated moment values in units of μ_B per Mn of the different samples are tabulated in Table 5.1. The competition between magnetoelastic and shape anisotropy contributes to the larger coercivity in the (001) film compared to the (110) and (111) films. Although epitaxial strain yields an out-of-plane easy axis, the film still has to overcome the magnetostatic energy of $\mu_0 M_S^2/2$ before complete out-of-plane magnetization is attained—energy required for domain wall motion and moment rotation. M_S is the saturated magnetization in units of emu/cm^3, and μ_0 is the permeability of free space. The anisotropy energy due to magnetostatics, or the shape effect, of the 34 nm (001) film as 7 K is 8.14×10^4 J/m^3 or 8.14×10^5 erg/cm^3. The corresponding anisotropy field is 4.5 kOe. The partially strained (110) film and the nearly fully relaxed (111) film show a saturated magnetization of about 560 emu/cm^3 (~3.5 μ_B per Mn), which is close to the expected saturated magnetization of 590 emu/cm^3 (3.67 μ_B per Mn).

The temperature-dependent remnant magnetization (M_{rem}) values of the thin films normalized to their values at 7 K are plotted in Fig. 5.10a. After the samples were field cooled at 10 kOe, the moments were measured at zero field. The different $La_{2/3}Sr_{1/3}MnO_3$ films show different Curie temperatures; compared to the bulk Curie temperature of 355 K, the Curie temperature is suppressed in the (001) film at 325 K, that of the (110) film is slightly suppressed at 334 K, and 347 K for the (111) film, which is closest to that of the bulk of ~355 K. A reduced Curie temperature is expected for a double exchange ferromagnetic with lower conductivity [4].

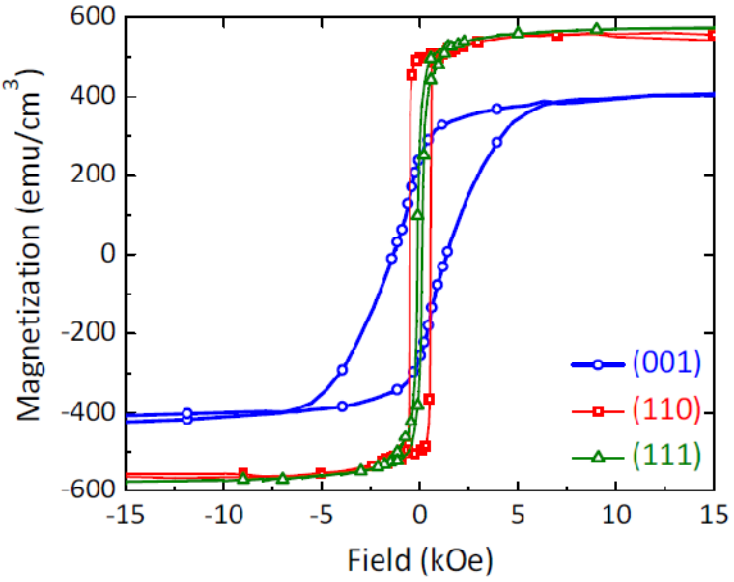

Figure 5.9. Hysteresis loops measured at 7 K of the 34 nm (001), (110), and (111) films. The expected saturation magnetization value of the bulk material is 590 emu/cm^3.

5.5.3 Magnetotransport

The substantial deviations in transport and magnetism of the coherently strained (001) film from the behavior of the bulk material motivate the study of magnetotransport. As mentioned in Section 5.2, the reduction in electronic bandwidth can lead to more pronounced metamagnetic transitions. Figure 5.10b shows the resistivity curves of the films measured in zero field and 50 kOe, applied normal to the sample plane; Fig. 5.10c shows the corresponding MR = $[R_S(50kOe)-R_S(0kOe)]/R_S(0kOe)$. Magnetization and resistivity scans of all of the samples do not exhibit temperature hysteresis. The fully relaxed $La_{2/3}Sr_{1/3}MnO_3$ film on (111) $LaAlO_3$ substrate shows a peak in MR at 351 K, near its Curie temperature of about 347 K (Figs. 5.10a and 5.10c), as observed in the bulk material of the same stoichiometry, while the (110) film exhibits a peak in MR that is 15 K below its Curie temperature. In addition, the breadth in temperature of the MR peak of the (110) film is noticeably greater than that of the (111) film.

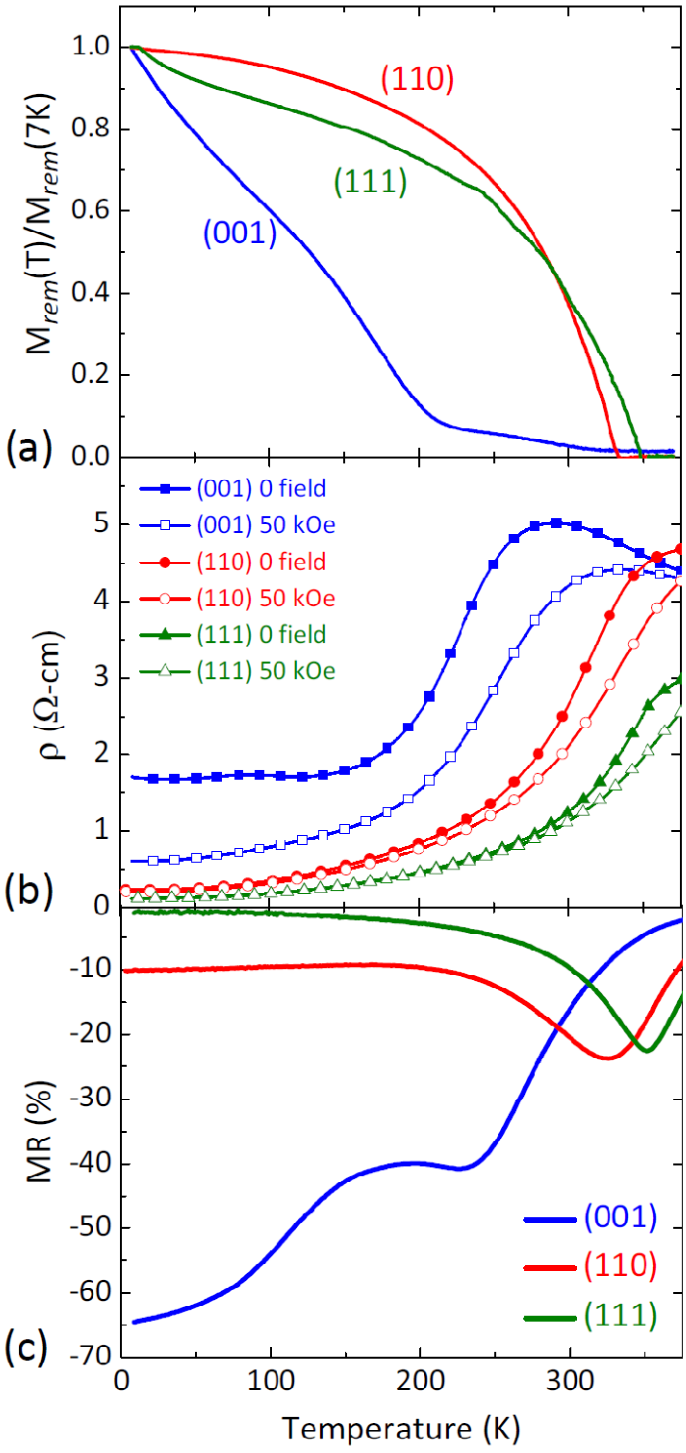

Figure 5.10. Temperature-dependent (a) remnant magnetization normalized to the value at 7 K, (b) resistivity at 0 and 50 kOe, and (c) MR measured at 50 kOe of the 34 nm (001), (110), and (111) films.

The greatest deviations in magnetotransport are seen the (001) film, which displays not only the highest MR but also over a wide temperature range; in particular, the MR is maximized at the lowest temperatures, whereas in the bulk of the same stoichiometry, the low-temperature MR is negligible. The local MR peak for the (001) film near 230 K seems to correlate with neither the Curie temperature nor the resistivity maximum; however, it does seem to coincide with the increase in magnetization observed below ~210 K (Figs. 5.10a and 5.10c). Despite being much lower in magnitude, the low-temperature MR of the (110) film is fairly substantial at about -10%, a phenomenon not observed in the bulk material of the same stoichiometry. The MR at 10 K and 50 kOe are given in Table 5.1 for the three films.

As opposed to the bulk material of the same stoichiometry, in the more distorted thin films, the magnetic transition no longer corresponds to kinks in their resistivity curves or peaks in their MR curves. Certainly the effects are most visible when comparing the magnetization, temperature-dependent resistivity, and MR curves of the coherently strained (001) film (Fig. 5.10). This observation is in contrast to the near coincidence of the MR peak and magnetic transition in the case of the almost fully relaxed (111) film.

For a single-phase double-exchange ferromagnet, a peak in MR near its Curie temperature and negligible MR at low temperatures are expected. The transfer integral of e_g electrons from site i to a neighboring site j is given as $t_{ij} = t|\cos(\theta_{ij}/2)|$, where θ_{ij} is the angle between the moments on sites i and j, and t is the transfer integral for $\theta_{ij} = 0^o$. Near the magnetic transition, though there is coupling among moments, the thermal energy is high enough to cause substantial randomization and therefore the adjacent moments cannot be aligned parallel. However, a magnetic field induces improved alignment of moments along the direction of the field, decreasing the angle between adjacent moments. Therefore, there is a large electrical response upon the application of a magnetic field, and the conductance increases. However, as the temperature becomes much higher than the Curie temperature and the thermal randomization of moments increases, a magnetic field of the same magnitude does not improve the alignment of moments as it would closer to the transition. Therefore, the MR decreases at higher temperatures. At very low temperatures, the thermal fluctuations are small, and the adjacent moments are already well aligned to one another; consequently, the gains in transfer integral by an applied field are slight, leading to negligibly low MR at low temperatures. Thermally excited magnons scatter carriers at this temperature range. It is possible that a magnetic field at low temperatures can suppress carrier-magnon scattering, but the resulting MR is small, as they are in conventional elemental magnets such as Fe, Ni, and Co below their magnetic transitions [51]. All in all, the MR features of the (111) film are fully consistent with those expected in a double-exchange ferromagnet, and the MR exhibited is not truly "colossal."

The relationship between magnetization and transport can be further emphasized by studying the MR dependence on magnetic field, shown in Fig. 5.11 for the (001) film at 7 K with the field applied out of plane. The sample was first heated to 380 K, above its Curie temperature, to achieve a fully demagnetized state, and subsequently cooled to 7 K at zero field before the scan was taken. All of the resistivity and MR versus magnetic

field plots were taken in this manner. Starting from zero, the field was first ramped up to positive fields, then lowered and switched to negative fields, before tracing a hysteresis back to positive fields, as indicated in Fig. 5.11. The local maxima in resistivity near ±3 kOe are likely attributed to carrier scattering at magnetic domain walls, and they occur fairly near the coercive field of 1.4 kOe. However, suppressing carrier scattering at or reduced kinetic energy across domain walls likely do not account for all (or even much) of the MR observed in Fig. 5.11. Such high MR is unexpected at such low temperatures, and the resistivity versus field curve with a hysteresis that fails to close even in a field of 70 kOe is likewise surprising.

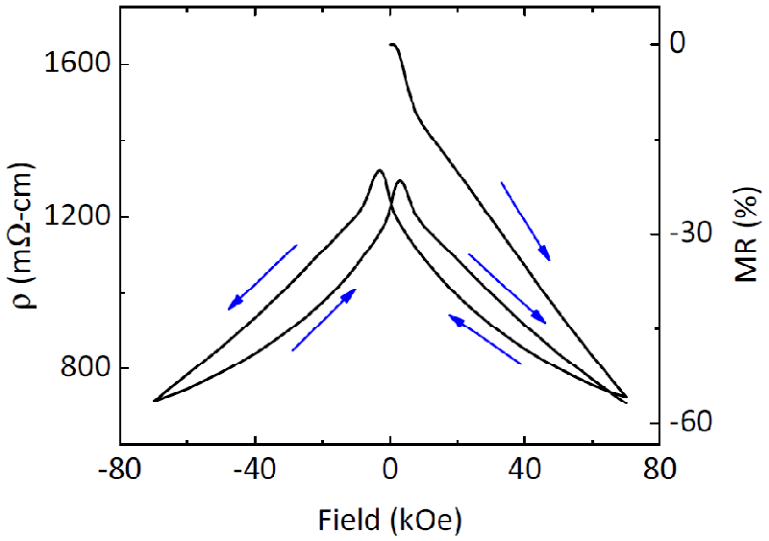

Figure 5.11. Magnetic field dependence of the out-of-plane MR of the 34 nm (001) film at 7 K. The arrows show the sequence of field sweeping.

With the same procedure as for the (001) film, the field dependence of MR of the (110) film was taken at 7 K for fields applied both out of plane and along the in-plane magnetically easy in-plane [1-10] direction, shown in Fig. 5.12. Figure 5.12 also includes a difference in the two curves ($MR_{IP} - MR_{OOP}$), which can be thought of as the anisotropic MR. The anisotropic MR saturates to roughly -1% with an applied field of 8 to 10 kOe, expected to be approximately the total anisotropy field of out-of-plane magnetization of this film. Although the sign of the anisotropy in MR is different from normally observed elemental magnets such as Fe, Ni, and Co [51], it is consistent with previous studies on $La_{2/3}Sr_{1/3}MnO_3$ films [52]. Here, the focus is not on the anisotropic component of MR since it represents a relatively small fraction of the total MR. Resistivity versus field curves at other temperatures were taken only with the field applied along the in-plane easy [1-10] direction.

Shown in Fig. 5.13 are field-dependent MR scans taken at 7, 75, and 225 K, temperatures well below the Curie temperature of 334 K. There is remnant magnetization at each of the measured temperatures, but only the curve at 7 K shows an

initial zero-field resistivity higher than the zero-field value after a field of 70 kOe is applied. The lack of a field hysteresis of the resistivity curves at 75 and 225 K suggests that the hysteresis is not attributed to just suppressed carrier scattering of magnetic domain walls in the remnant state as compared to the initial demagnetized state. Note the phenomenological similarities between the low-temperature curves of the (001) and (110) films, despite their differences in magnitude of MR.

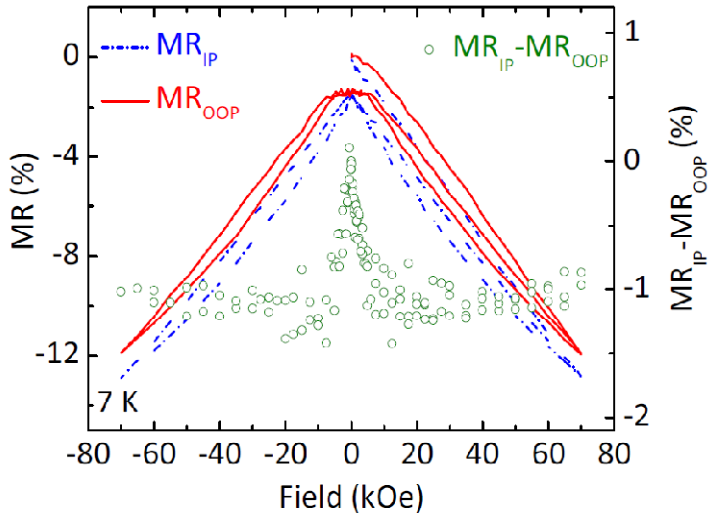

Figure 5.12. The in-plane (IP) and out-of-plane (OOP) MR as well as the difference between the two for the (110) film at 7 K. For the in-plane measurement, the field was applied along the [1-10] direction—the magnetically easy direction.

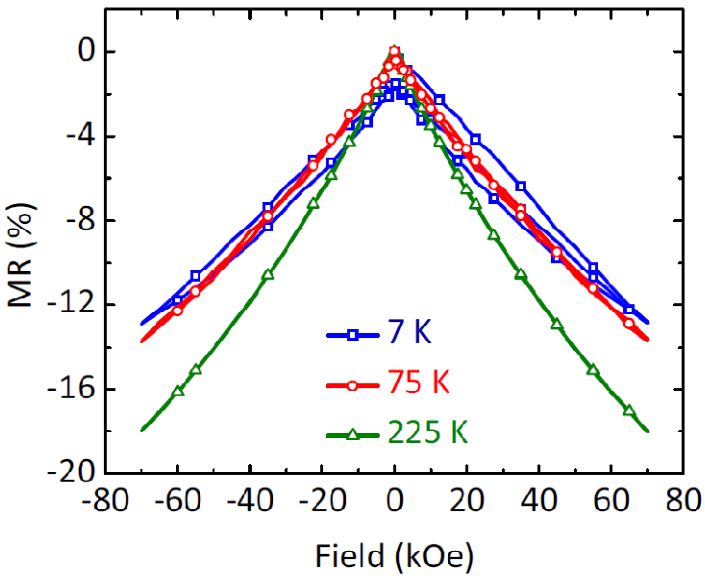

Figure 5.13. The in-plane MR of the (110) film at various temperatures. For the in-plane measurement, the field was applied along the [1-10] direction.

§ 5.6 The significance of strain coherency in (001) films

The importance of epitaxial strain can be further exemplified by comparing a coherently strained (001) film with a partially relaxed one. A partially relaxed 45 nm (001) film, thicker than the coherently strained 34 nm (001) film, can be grown under the same deposition conditions. As shown in Fig. 5.14, the reciprocal lattice map of the 103 reflection of the 45 nm $La_{2/3}Sr_{1/3}MnO_3$ film shows that it is neither coherently strained nor fully relaxed. From the 103 film reflection, the in-plane and out-of-plane lattice parameters of the film can be determined to be 3.83 and 3.92 Å, respectively. Furthermore, the strain tensor can be calculated to be

$$\boldsymbol{\varepsilon} = -0.52\begin{bmatrix}1 & 0 & 0\\ 0 & 1 & 0\\ 0 & 0 & 1\end{bmatrix}\% + \begin{bmatrix}-0.77 & 0 & 0\\ 0 & -0.77 & 0\\ 0 & 0 & 1.20\end{bmatrix}\%$$

Both the volume contraction and tetragonal distortion components are smaller than those of the 34 nm (001) and (110) films. Therefore, it is expected that this film behaves more similarly to the bulk and the nearly fully relaxed (111) film.

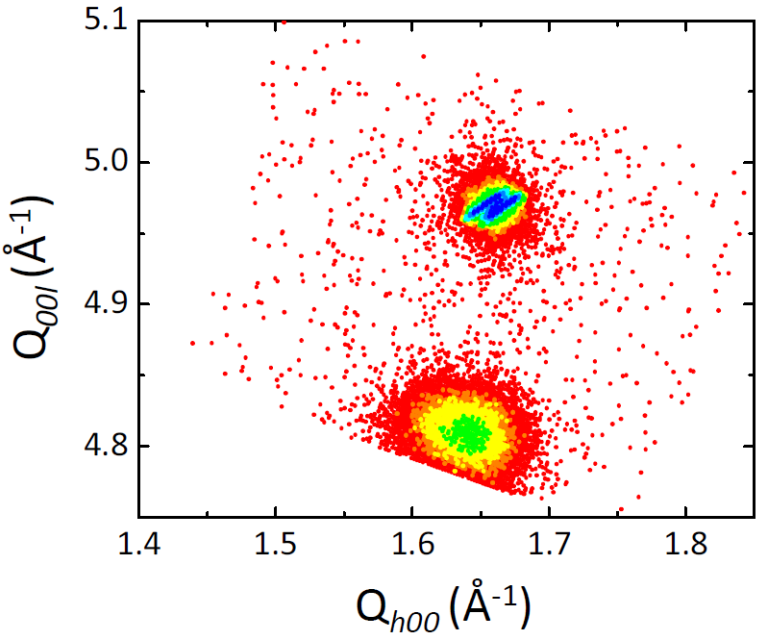

Figure 5.14. An asymmetric 2θ-ω map of the 103 reflection of the partially relaxed 45 nm $La_{2/3}Sr_{1/3}MnO_3$ film on a (001) $LaAlO_3$ substrate.

Figure 5.15 shows the temperature-dependent MR at 50 kOe of the partially relaxed 45 nm (001) film. As determined by a magnetization versus temperature scan (not shown), its Curie temperature is 343 K, close to its peak in MR at 341 K. It is similar to the 34 nm (111) film in that its MR peaks near the magnetic transition, but it also exhibits non-negligible MR at low temperature of roughly -3%. The low-

temperature resistivity of the partially relaxed 45 nm (001) film, 75 μΩ-cm at 10 K, is lower than even the relaxed 34 nm (111) film (see Table 5.1). The ω scan of the 002 reflection of the 45 nm (001) film shows that its full-width at half-maximum value is 0.25° (data not shown), smaller than that of the (111) film of 33°. Therefore, one can deduce that in these epitaxial $La_{2/3}Sr_{1/3}MnO_3$ films, both the atomic lattice structures and microstructures can affect electrical transport.

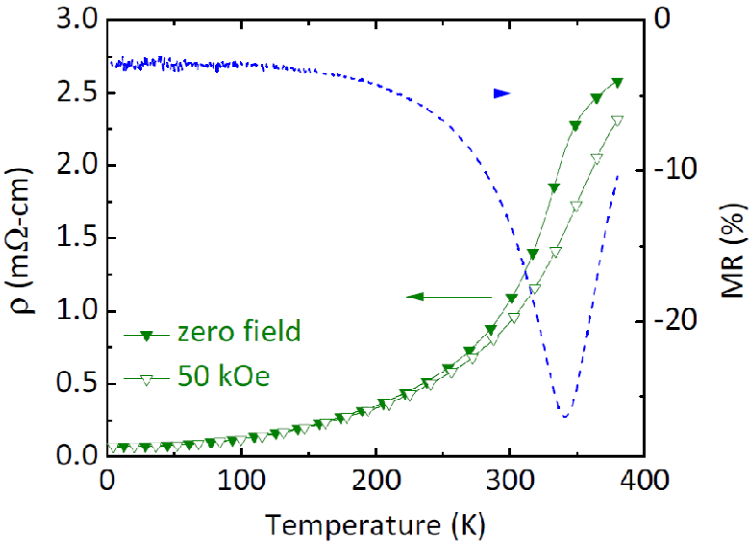

Figure 5.15. Plots of resistivity at zero and 50 kOe applied field and the corresponding MR of the partially relaxed 45 nm $La_{2/3}Sr_{1/3}MnO_3$ film on (001) $LaAlO_3$.

§ 5.7 On the possibility of strain-induced phase separation

The 29% lower saturated magnetization and roughly ten-fold higher resistivity of the coherently strained 34 nm (001) film as compared to the (111) film at low temperatures (Table 5.1) can be attributed to one of two possibilities: (1) a single "ferromagnetic" phase with a canted moment structure, i.e. two sublattices of different canting orientations, thus giving rise to reduced conductance, or (2) two-phase coexistence of a ferromagnetic metallic phase and an insulating, possibly antiferromagnetic, phase. The observation of large low-temperature MR values in the (001) film in itself does not rule out either possibility since the applied magnetic field can reduce canting in the first scenario and induce an insulator-metal transition as well as a metamagnetic transition in the second scenario to account for increased conductivity. However, in a single-phase material, one would expect a stronger MR signature near the magnetic transition of the (001) film, a feature not observed in its MR curve (Fig. 5.10c). Furthermore, the discussion in Section 5.2 does suggest the propensity of the manganites toward two-phase separation, whether or not it is associated with carrier phase separation. On the

other hand, there is a peak in MR at 351 K in the (111) film, very close to its Curie temperature, and it is hence believed that the (111) film is characteristic of a single-phase ferromagnetic material. There is reason to speculate that the lower magnetization, increased resistivity, and enhanced magnetoresistance—most markedly at low temperatures—together suggest that coexistence of insulating, likely antiferromagnetic, and ferromagnetic metallic phases in the coherently strained (001) film.

In bulk manganites, insulating/metallic or antiferromagnetic/ferromagnetic phase competition has been heavily investigated. Several different variables can be modified to toggle between the different low-temperature states. A schematic of the canonical phase diagram of the manganites is shown in Fig. 5.16. The different variables that can be experimentally controlled on the horizontal axes are hole doping and average A-site radius. In a *gedanken* or a computational experiment, electronic bandwidth or antiferromagnetic exchange energy can also be adjusted. Taking disorder into account, the low-temperature transition along the horizontal axis goes through a two-phase region [8]. It is certainly reasonable that the lattice strain is likewise an appropriate thermodynamic variable for the horizontal axis. The effect of lattice deformation on the disorder parameter remains an untapped area of research, but lattice effects on magnetic ordering have been systematically studied in the computational study of Colizzi *et al.* [53].

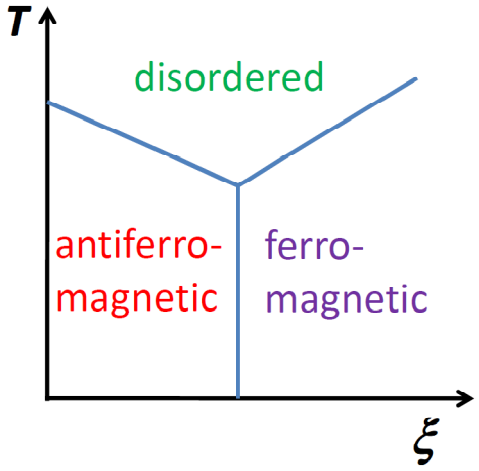

Figure 5.16. Canonical phase diagram of the manganites manifested by the competition between double exchange and superexchange. The disordered phase occurs at high temperatures (*T*), and the equilibrium ordered phase (antiferromagnetic or ferromagnetic) also depends on another thermodynamic variable (ξ), which can be average A-site cation radius, hole doping, electronic bandwidth, relative strengths of double exchange and superexchange, and so on.

The (110) film has a lower degree of tetragonal distortion compared to the (001) film as well as some shear strain. The pronounced MR peak of the (110) film occurs at a temperature more removed from its Curie temperature and is much broader as compared to the (111) film. Furthermore, the sizeable low-temperature MR of about -10% observed in the (110) film suggests that it may also be near a single phase/two phase coexistence

boundary. It may already contain some regions of an insulating low-temperature phase that can account for the MR observed at the lowest temperatures measured. The resistivity versus field hysteresis loops of the (001) and (110) films at 7 K (Figs. 5.11 and Fig. 5.12) which do not appear close up to a field of 7 K may be linked to a gradual metamagnetic transition. The (110) film exhibits similar behavior as the (001) film at the lowest temperatures measured despite their opposite signs in their respective tetragonal strain tensors. Therefore, in general, it can be concluded that any lattice distortion that acts to reduce the overlap integral of the e_g states in the manganites effectively makes the ferromagnetic state less stable with respect to a low-temperature insulating state; this low-temperature insulating phase undergoes phase instability upon application of a magnetic field. The observations presented here are also consistent with previous studies that have shown that insulating (001) $La_{2/3}Sr_{1/3}MnO_3$ thin films can be achieved through both in-plane biaxial compression [42] and tension [36].

Unfortunately, the effects of the shear strain components of the magnetic, electrical, and magnetotransport properties of $La_{2/3}Sr_{1/3}MnO_3$ cannot be fully examined in this study. Appendix A.2 shows that in coherently strained (111) films, there is only volume dilation and shear strain but no tetragonal distortions. The main roadblock is the inability of stabilizing sufficient shear strain in (111) films of reasonable thicknesses for reliable magnetization measurements.

Higher resistivity signifies the system is shifted toward a more insulating state. The relevant competing mechanisms are superexchange antiferromagnetism between electrons of adjacent hall-filled t_{2g}^3 states that favors localization of the e_g electrons and double exchange ferromagnetism that favors charge itinerancy of the e_g electrons. Possible temperature-activated Jahn-Teller distortions may also important, but would not account for the low-temperature MR. Regardless, the tetragonal strain components imposed by the substrate can dually decrease hybridization and lift the degeneracy of e_g states—both of which help stabilize a more insulating state.

The work presented here on enhancing the magnetoresistive properties of $La_{2/3}Sr_{1/3}MnO_3$ films by reducing sample conductivity is limited to effects arising from atomic lattice distortions. For example, though the relaxed (111) film exhibits higher resistivity than the partially strained 45 nm (001) film, the low-temperature MR of the (111) is smaller. Presumably, its higher resistivity is attributable mainly to microstructural defects, exemplified by a relatively large full-width at half-maximum value in its ω scan (Fig. 5.5b and Table 5.1). A comparison of the relaxed (111) and the partially strained (001) films reveals that in these epitaxially films, attempts to increase the resistivity by microstructural means do not necessarily bring about enhanced MR. This is in contrast to enhanced MR over a wide range of temperatures in polycrystalline bulk samples [54] and films deposited on polycrystalline substrates [55]. Low-angle grain boundaries that likely exist in the (111) film do not lead to much improvement in magnetoresistive properties; it appears transport across high-angle grain boundaries is very sensitive to an applied magnetic field, but that topic is not within the scope of this work.

§ 5.9 Can phase separation be tuned?

In this work, the electronic properties of $La_{2/3}Sr_{1/3}MnO_3$ films are modified through atomic lattice distortions. In order to exploit the microscopic phenomenon of phase separation in tuning the macroscopic property of MR, the characteristic length scale, volume fraction, and morphology of the different phases must be controllable. This work focuses exclusively on the macroscopic magnetotransport properties of thin films. A recent report made possible by the development of microwave impedance microscopy presents an interesting opportunity to directly study the morphology of electronic phase-separated materials [14]. Microwave impedance microscopy appears to be a means to yield optical (frequency-dependent) conductivity with spatial resolution on the order of 50 nm by employing an atomic force microscope tip. For the imaging of phase-separated samples, it may be more versatile and the data may be more direct than scanning tunneling microscopy. Lai *et al.* observed field-dependent changes in volume fraction and morphological texturing in their $Nd_{1/2}Sr_{1/2}MnO_3$ films, a compound known to exhibit mesoscopic phase separation even in the bulk [14].

If the morphology of the phases of a manganite sample is known, patterning and nanostructuring of the sample can allow one to take advantage of the inhomogeneous, possibly mesoscale regions [13,56]. It would be ideal if the samples can be structured in a way such that it is very close to a percolation threshold, which can be traversed upon the application of a preferably small magnetic field or carrier injection.

§ 5.10 Conclusions and outlook

Though there has been much work on strain effects on Ca-based manganite thin films and the possible connection to phase separation [13,43,57,58], bulk Ca-based manganites are already very susceptible to phase separation. Furthermore, the MR behavior of compounds near the 50:50 rare-earth/Ca composition is dramatic, likely owing to the stability of a commensurate charge-ordered phase. However, this is not the case for the larger-electronic-bandwidth $La_{1-x}Sr_xMnO_3$. In addition, at the $La_{2/3}Sr_{1/3}MnO_3$ composition the strength of double exchange is optimized in the bulk material. Therefore, this material is an ideal reference system to study the possibility of inducing a more insulating low-temperature state for enhancing the thin-film magnetoresistive properties over a broad temperature range.

The data presented on the coherently strained (001) and partially strained (110) $La_{2/3}Sr_{1/3}MnO_3$ films on $LaAlO_3$ substrates suggest thin-film electronic transitions are indeed possible in mixed-valent systems. Lattice strain is another variable that can be exploited along with stoichiometry to change the properties and the low-temperature ordered states of manganites. For these films, it appears the vital component is the competition between superexchange charge localization and double exchange charge itinerancy—as they can be modified through lattice deformation.

Mathieu *et al*. suggested that CMR may emerge for manganites even without phase separation [59]. They studied $Eu_{1/2}Ba_{1/2}MnO_3$ and $Sm_{1/2}Ba_{1/2}MnO_3$, small bandwidth systems with large Attfield parameters—which they claimed to be the two essential ingredients for CMR with or without phase separation. The Attfield parameter of $Sm_{1/2}Ba_{1/2}MnO_3$ is 3.42×10^{-2} Å^2 based on the 12-coordinated Shannon radii of Sm^{3+} and Ba^{2+}. The Shannon radii are used, because the Pauling radius for Sm^{3+} is unavailable. For a fair comparison, based on the Shannon radii, the Attfield parameter for $La_{2/3}Sr_{1/3}MnO_3$ is 1.42×10^{-3} Å^2. An interesting, unanswered issue is the effect of epitaxial lattice distortions on the site-to-site bond and magnetic fluctuations. Undoubtedly the different microscopic ingredients for the phenomenology of CMR will be further explored. Strain in thin films should provide for a unique platform to investigate lattice-induced electronic bandwidth changes as well as atomic site disorder.

The work in this and in the previous chapter demonstrates the possibilities of strain-controlled electronic transitions in perovskite oxide thin films. The next chapter focuses on an interface-induced electronic transition in $LaAlO_3/SrTiO_3$ heterojunctions.

Chapter 6

Disorder, Magnetotransport, and Spin-Orbit Interaction at $LaAlO_3/SrTiO_3$ Heterointerfaces

6.1. Discovery of and work on metallic (001) $LaAlO_3/SrTiO_3$ interfaces 86
6.2. Interfacial carrier gases in semiconductor heterostructures 89
6.3. Growth and structure of $LaAlO_3$ films on $SrTiO_3$ substrates 91
6.4. Temperature- and $LaAlO_3$ thickness-dependent electrical transport 92
6.5. Low-temperature quantum correction to conductance 96
6.6. Magnetotransport and its anisotropy 97
6.7. Possible origin of disorder and spin-orbit interaction 102
6.8. Exploiting spin-orbit interaction 108
6.9. Conclusions and outlook 110

The previous chapters have considered systems in which thin-film heteroepitaxial lattice distortions induce electronic transitions. Through the formation of a heterojunction, electrons must move from one material to the other in order to equilibrate the electron chemical potential. The transfer of electrons at the interface can likewise induce an electronic transition. Such effects can be very large in polar and ionic materials such as transition-metal oxides. A model system that has received much interest is the metallic (001) $LaAlO_3/SrTiO_3$ heteroinference. Recent experiments have suggested that under a range of thin-film deposition conditions, metallicity is caused by the intrinsic interfacial polarity, rather than crystal defects, and that it is spatially confined. Reported here, magnetotransport studies reveal that at low temperatures the thickness of the metallic electron channel on the $SrTiO_3$ side of the interface should be limited to at most one carrier mean free path. Low-temperature transport studies also uncover that localization effects are important to consider in this system wherein interfacial polarity induces an insulator-metal transition of a quasi-two-dimensional electron channel. The quasi-two-dimensional nature of the conductive channel results in anisotropy in out-of-plane versus in-plane magnetoresistance (MR). These observations will be discussed as they may relate to localization and low-temperature electron interference. In addition, the observation of strong spin-orbit interaction may prove to be a potentially functional property of this oxide heterointerface.

§ 6.1 Discovery of and work on metallic (001) $LaAlO_3/SrTiO_3$ interfaces

Since the discovery of the metallic $LaAlO_3/SrTiO_3$ heterointerface [1,2], there have been a remarkable number of subsequent experimental [2-9] as well as theoretical [10-13] studies in effort to understand the origins of metallicity. Typical samples are composed of single $LaAlO_3$ films deposited on TiO_2-terminated (001) $SrTiO_3$ substrates. The original explanation proposed is that polarity arising at the (001) heterojunction formed by charge neutral (002) planes of $SrTiO_3$ and alternately charged (002) planes of $LaAlO_3$ results in an unstable build-up of electric potential with increasing $LaAlO_3$ film thickness, shown in Fig. 6.1 [1,2]. Whereas the so-called *n*-type $(LaO)^+/TiO_2$ interface is metallic, the $(AlO_2)^-/SrO$ remains insulating.* The discussion here will be mainly kept to *n*-type $(LaO)^+/TiO_2$ interfaces, in which an insulator-metal transition is induced. Owing to polar electronic instability, an interfacial metallic channel forms spontaneously once a critical thickness of $LaAlO_3$ thin film is reached in order to relieve the electric potential—i.e. electronic reconstruction. In the original report by Ohtomo and Hwang, they surmised that exactly half an electron per interface unit cell should be transferred to the $SrTiO_3$ side, forming a one-unit-cell thick metallic channel [1]. It can be seen that adding such a density of electrons to the TiO_2 layer at the interface in Fig. 6.1 would "solve" the divergence problem. But the origin of these electrons was not explicitly

* The ionic limit is taken to label the formal charges of the (002) planes.

addressed. Furthermore, attempts to directly measure the thickness of the metallic channel suggest that it is closer to ~10 nm [14,15].

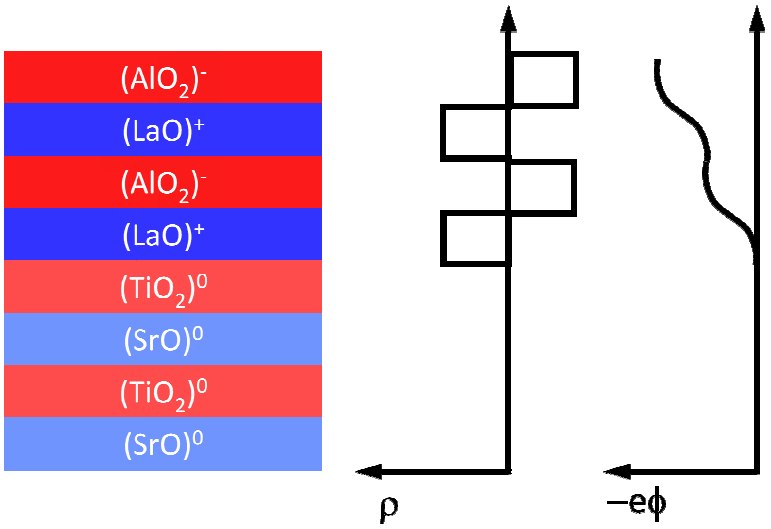

Figure 6.1. Schematic a (001) $LaAlO_3/SrTiO_3$ heterojunction showing the (002) planes and the corresponding spatial dependence of ionic charge density (ρ) and electric potential energy ($-e\phi$).

Some early experimental studies proposed oxygen vacancies, known be to donors [16,17], in the $SrTiO_3$ substrates as the cause of metallicity in the heterojunctions [4-6], but several other experimental observations suggest that metallicity is driven intrinsically by interfacial polarity. First, the *p*-type $(AlO_2)^-/SrO$ interface, fabricated by first depositing a layer of SrO on a TiO_2-terminated (001) $SrTiO_3$ substrate before the deposition of a $LaAlO_3$ thin film, was shown to be electrically insulating [1]. Nakagawa *et al*. argue that the reason for metallic *n*-type interfaces and insulating *p*-type interfaces is that whereas electron reconstruction "heals" polar instability in *n*-type interfaces, ionic reconstruction (interdiffusion) "heals" polar instability in *p*-type interfaces [2]. Regardless, it is unlikely that the creation of oxygen vacancies is dependent on interface termination. Second, Thiel *et al*. found that a critical thickness of four unit cells of $LaAlO_3$ film is necessary before an interfacial insulator-metal transition is induced [3]. If the deposition conditions in themselves create a substantial amount of oxygen vacancies, one would not expect to see a critical $LaAlO_3$ thickness of the onset of metallicity. Third, the same samples grown by oxide molecular beam epitaxy have produced similar results to samples grown by pulsed-laser deposition [18]. This finding is important because it was believed that ion bombardment from the plume of ablated material onto substrates can enhance the formation of crystal defects in the substrates, which then cause metallicity [4,5]. These observations suggest that it is indeed possible to deposit samples

whose electrical transport properties are not dominated by oxygen vacancies in the $SrTiO_3$ substrates.

In $LaAlO_3/SrTiO_3$ heterointerfaces, interface polar instability leads to "on" channels in as-grown samples. If they cannot be turned off, they would be of little engineering value. Advancements in semiconductor devices and heterostructures can be invariably attributed to the high level of engineering control. On the one hand, a metallic channel created by a polar interface between two nominally undoped constituent insulators has served as a great model system in generating new materials properties through changing the charge degree of freedom. On the other hand, Kroemer in his 2000 Nobel lecture specifically addressed the *problem* of interface polarity [19], which was first considered by Harrison in (001) Ge/GaAs heterojunctions [20]. The *warning* is that interface polarity results in drastic charge redistribution of potentially both carriers and ions that would ultimately lead to difficulties in achieving precise control; fluctuating potentials due to "residual charges, with deleterious consequences for any device application" would likely occur [19].

Despite the challenges to engineer precise carrier densities at polar interfaces, interfacial electronic instability creates a wealth of unexpected and rich electrical transport phenomena that may be exploited if understood properly. Moreover, although there have not been successful reports of turning off as-grown metallic interfaces, it has been shown that carrier concentration and the superconducting transition temperature of the heterointerfaces can be modulated by gate voltages [21-24], despite differing interpretations between Schneider *et al*. [21] and Bell *et al*. [22] on the principle mechanism that causes the modification of superconducting transition temperatures. In some cases, data suggest the existence of a quantum superconductor-metal-insulator transition that can be traversed by the application of a gate voltage [21], but room-temperature gate-control remains challenging.

However, it has been demonstrated that nanostructures can be written on $LaAlO_3$ films on $SrTiO_3$ substrates using an atomic force microscopy (AFM) tip with a positive voltage when the deposited film is slightly thinner than a $LaAlO_3$ critical thickness of 4 unit cells, i.e. between 3 and 4 unit cells [25,26]. As grown, the sample is in an "off," high-resistance state. With patterned sources and drains, Cen *et al*. used an AFM tip to write channels, hence turning "on" the device, and showed that the switching is nonvolatile; however, the application of sufficient negative voltage can turn turn "off" the metallic state [25]. The switching mechanism is not fully agreed upon yet. It has been speculated that a positive voltage on the AFM tip can ionize water molecules and upon desorption of OH^- ions, the remaining H^+ on the surface of the $LaAlO_3$ result in band bending in $SrTiO_3$ and therefore the creation of an electron channel in $SrTiO_3$ near the heterointerface [25]. Turning off the device requires the application of a negative voltage on the AFM tip to remove H^+. It has been shown that this technique can be used to draw structures with nanometer spatial resolution.

Besides striving to achieve engineering control of the heterointerface, many research groups have conducted studies to investigate the properties of the metallic state

induced by polar instability, with particular emphasis on functionalities unique from bulk electron-doped $SrTiO_3$.[†] As in *n*-type $SrTiO_3$ bulk crystals, a superconducting state can be attained over a range of carrier densities [7,21-24,27,28,29]. However, there are some groups who have claimed the indirect observation of long-range magnetism [8,28] and magnetic inhomogeneities [30] based on MR and Hall effect measurements. The origins of any possible magnetic ordering remain unclear to this day.

The primary purpose of this study is to investigate the properties of the metallic state of the interfacial electron channel; careful documentation of the characteristics of the metallic as-grown samples is necessary for pursuing better control. Many of the experiments here were initially motivated by studying the effects of disorder at low temperatures in a quasi-two-dimensional electron system, and in the process, strong spin-orbit interaction was found. Emphasis will be put on features that may not be readily attainable in conventional semiconductor heterojunctions.

§ 6.2 Interfacial carrier gases in semiconductor heterostructures

As much of the work on oxide heterojunctions is motivated by and can be related to semiconductor counterparts, a brief survey of semiconductor heterojunctions is presented.

The successful design and engineering of semiconductor heterojunctions have enabled many electronic and optoelectronic advances. In 2000, H. Kroemer and Z. I. Alferov shared half of a Nobel Prize[‡] for their contributions in band offset engineering that allows for the steering of electrons and holes with "quasi-electric fields" [19]. For example, heterointerfacial band offset-induced quasi-electric fields are exploited in quantum well structures that localize both electrons and holes in the wells, a feature useful for the design of lasers.

While quantum well light emitters were perhaps one of the earliest successful realizations of band offset engineering, Kroemer's original intention was to find new approaches for enhancing carrier mobility. In 1978 the seminal achievement of modulation-doped *n*-$Al_{1-x}Ga_xAs$/*i*-GaAs heterostructures was the attainment of metallic conduction and high carrier mobility in the intrinsic GaAs side of the interface. Figure 6.2a is a schematic of *n*-doped $Al_{1-x}Ga_xAs$[§] and intrinsic GaAs showing the band offsets. Upon creation of the junction, the Fermi levels must be equilibrated, and the band offsets must still be maintained (Fig. 6.2b). Band bending manifested in the transfer of electrons, in this case from *n*-$Al_{1-x}Ga_xAs$ to intrinsic GaAs, is required to satisfy the criteria above. Though GaAs is not chemically doped, metallic conduction ultimately

[†] Successful electron doping of $SrTiO_3$ can be achieved by oxygen vacancies, La substitution of the Sr site, and Nb substitution of the Ti site.

[‡] The other half of the Nobel Prize in physics that year was given to J. S. Kilby for the invention of integrated circuits.

[§] For a schematic illustration, the exact composition of the (Al,Ga)As alloy need not be specified.

occurs on the GaAs side. The formation of the interface creates impurity donors that remain ionized at cryogenic temperatures on the $Al_{1-x}Ga_xAs$ side, and an electron gas confined by conduction band bending on the GaAs side. The advantage of this structure is that free conduction band electrons can be introduced and are spatially separated from the ionized donors. Coulomb scattering between the positively charged localized impurities and carrier electrons is partially shielded by the interface because of spatial separation, hence resulting in reduced scattering rates. However, the early modulation-doped structures were limited to a peak mobility of roughly ~15,000 cm^2/Vs [31]. An approach to enhance low-temperature mobility was to place the scattering scatters, i.e. ionized donors in the *n*-$Al_{1-x}Ga_xAs$, away from the interface—farther from the free electrons in the intrinsic GaAs. Dramatic enhancement of mobility in these high-mobility heterojunctions was realized only after the careful introduction of an undoped buffer layer and precise control of carrier transfer [32]. In clean, precisely controlled interfaces, the temperature-dependent mobility values correspond to calculated ones [33].

Likewise, one of the initial hopes of polarity-induced metallicity at oxide interfaces was to achieve higher carrier mobilities as compared to the bulk by injecting carriers into $SrTiO_3$ while not introducing impurities. However, heterointerfaces thus far have generally exhibited lower mobility values as compared to commonly reported ones for bulk $SrTiO_3$ [16]. The issues of carrier scattering, particularly at low temperatures, will be discussed extensively in this work.

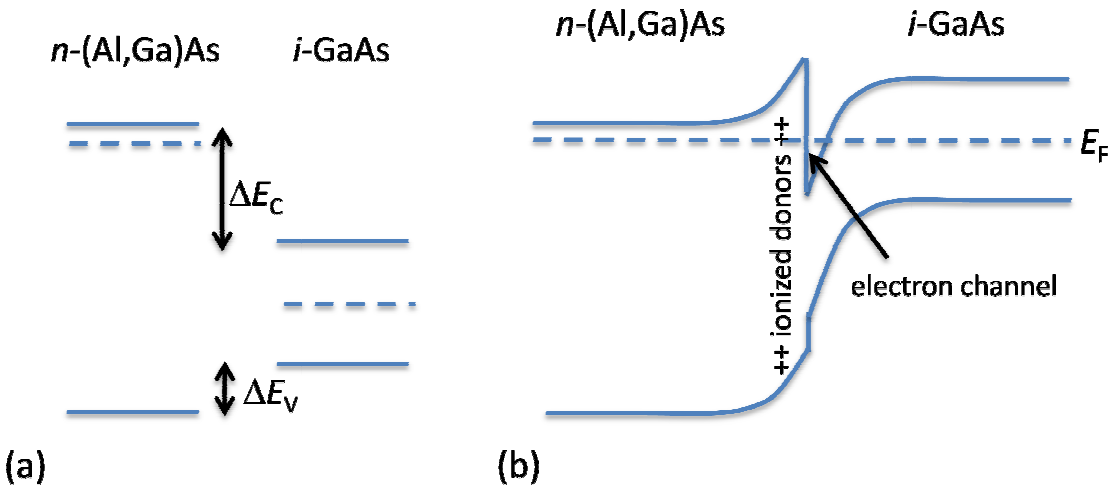

Figure 6.2. Schematics of the valence and conduction band edges of *n*-(Al,Ga)As and *i*-GaAs (a) prior to the formation of the heterointerface showing the band offsets and (b) after the formation of the heterointerface including the appropriate band bending to accommodate the band offsets and equilibrate the Fermi level.

Creating two-dimensional gases at polar interfaces is nothing new. In fact, it has been shown that at (0001) wurtzite AlGaN/GaN heterointerfaces, both electron gases

and hole gases can be formed depending on the termination plane of the underlying GaN film [34]. Likewise, the polarization along that [0001] direction[**] is thought be the dominant mechanism for the generation of carriers, as there are no intentional dopants incorporated [34]. Although both Al and Ga have nominal valence states of 3+, bond covalency and their difference in electronegativity can be sufficient for interfacial polarity. Furthermore, the piezoelectric response of strained layers can add a electric field near the interface to induce more carrier accumulation [35,36]. The possible effects of piezoelectric response in strained $LaAlO_3$ films deposited onto $SrTiO_3$ have yet to be considered, and will only be briefly mentioned in this work.

Similarly, a two-dimensional electron gas can be formed at (0001) $ZnO/Mg_xZn_{1-x}O$ heterointerfaces, in which both orientational polarization and piezoelectricity of ZnO are believed to contribute to metallicity [37]. Zn^{2+} has a completely filled 3*d* shell, so the conduction band of ZnO is expected to be *s*-like. The reported carrier electron effective mass is $0.32m_0$, where m_0 is the bare electron mass; this value is roughly an order of magnitude lower than that of $SrTiO_3$. Moreover, relatively clean $ZnO/Mg_xZn_{1-x}O$ heterointerfaces can be made using molecular beam epitaxy. Together a fairly low electron effective mass and long carrier scattering times makes it possible to realize the quantum Hall state [37].[††] Although the observation of the quantum Hall effect remains a benchmark of the quality of quasi-two-dimensional conductive systems, the work reported in this study will show that perhaps pursuing other phenomena in $LaAlO_3/SrTiO_3$ heterointerfaces not easily attainable in conventional semiconductor heterojunctions is even more promising. Any effect reliant on Landau quantization will be inherently limited by the rather large conduction band effective mass of $SrTiO_3$. On the other hand, the possible ground states and dynamics of interfacially confined quasi-two-dimensional electron gases of *d*-like carriers have been a largely unexplored area, and completely new properties may emerge.

§ 6.3 Growth and structure of $LaAlO_3$ films on $SrTiO_3$ substrates

$LaAlO_3$ films were grown at 700 °C, 2 Hz pulse frequency, ~180 J/cm^2 laser fluence, and in an oxygen pressure of 2.5×10^{-5} Torr on TiO_2-terminated (001) $SrTiO_3$ substrates. To achieve the correct surface termination, the substrates were first sonicated in deionized water for ten minutes and then submerged into 50:1 buffered hydrofluoric acid solution. They were then annealed in ambient at 1000 °C for 2 hours to achieve smoother step edges on the surfaces. An atomic force microscopy image of a

[**] (0004) planes of a wurtzite structure such as GaN alternate between Ga and N planes.

[††] The criteria for a quantum Hall state is $\hbar\omega_c = \hbar eB/m > k_B T$ and $\omega_c\tau > 1$, where ω_c is cyclotron frequency, B is magnetic field, m is electron effective mass, T is temperature, and τ is mean free scattering time. The first criterion ensures the discrete Landau levels are not smeared out by temperature, and the second criterion ensures that the electrons can undergo full cyclotron orbits before they scatter.

representative 10 nm $LaAlO_3$ film on a TiO_2-terminated and annealed substrate is shown on Fig. 6.3a. Although most of the samples reported here were not grown with *in-situ* monitoring of a grazing incidence reflective high energy electron diffraction pattern, Fig. 6.3b shows the oscillations of a diffracted beam; the oscillations reveal that despite the lattice mismatch (a = 3.79 Å for $LaAlO_3$ and 3.905 Å for $SrTiO_3$), smooth layer-by-layer thin-film growth can be achieved. Each oscillation peak represents the point in which a full unit-cell layer is deposited across the substrate. Figure 6.3c is an out-of-plane 2θ scan of the 00*l* reflections, and Fig. 6.3d is an ω scan of the 002 reflection of the film, whose peak has a full-width at half-maximum value of 0.09°. X-ray diffraction shows single-phase and single-orientation growth of the perovskite film on the perovskite substrate. The relatively narrow peak in the ω scan reveals the high in-plane crystalline quality of the film. The 2θ scan shows that by 10 nm of $LaAlO_3$ film, its out-of-plane lattice parameter relaxes to that of the bulk. It is also seen that heterointerface samples with strained, thinner $LaAlO_3$ films can also be metallic; therefore, any possible piezoelectric response of $LaAlO_3$ is not the sole or primary cause of metallic conduction in the samples shown here. Films of thicknesses from 2 to 14 nm were grown. The film thicknesses and stoichiometry were checked by Rutherford backscattering spectrometry and x-ray reflectivity.

§ 6.4 Temperature- and $LaAlO_3$ thickness-dependent electrical transport

Although Thiel *et al.* suggest that beyond the critical thickness of four unit cells of $LaAlO_3$ the interfacial metallicity does not change appreciably with increasing film thickness [3], it is found here that there is a thickness-dependent evolution of electrical transport. Temperature-dependent carrier concentration and mobility values for samples with a 5 nm and an 11 nm film can be extracted from Hall measurements and are shown in Fig. 6.4. The carrier concentration of the sample with a 11 nm film is larger than that of the sample with a 5 nm film for the entire temperature range measured, but the mobility values of the lower carrier concentration sample are higher, particular at low temperatures—in which the dominant mechanism limiting carrier mean free path is elastic scattering with defects. In this chapter, any elastic scattering center will be referred to as *disorder*. In addition, at the highest temperatures measured (up to 300 K), while the carrier concentration of the heterointerface with the thicker film continues to increase gradually with temperature, that of the thinner film appears to saturate.

The expected sheet carrier concentration according to the arguments presented in Refs. [1,2] is about 3.3×10^{14} cm^{-2}, and no temperature dependence is expected. However, in addition to being temperature dependent, the sheet carrier concentration values measured generally are considerably lower over the temperature range between 2 and 300 K than their "expected" value.

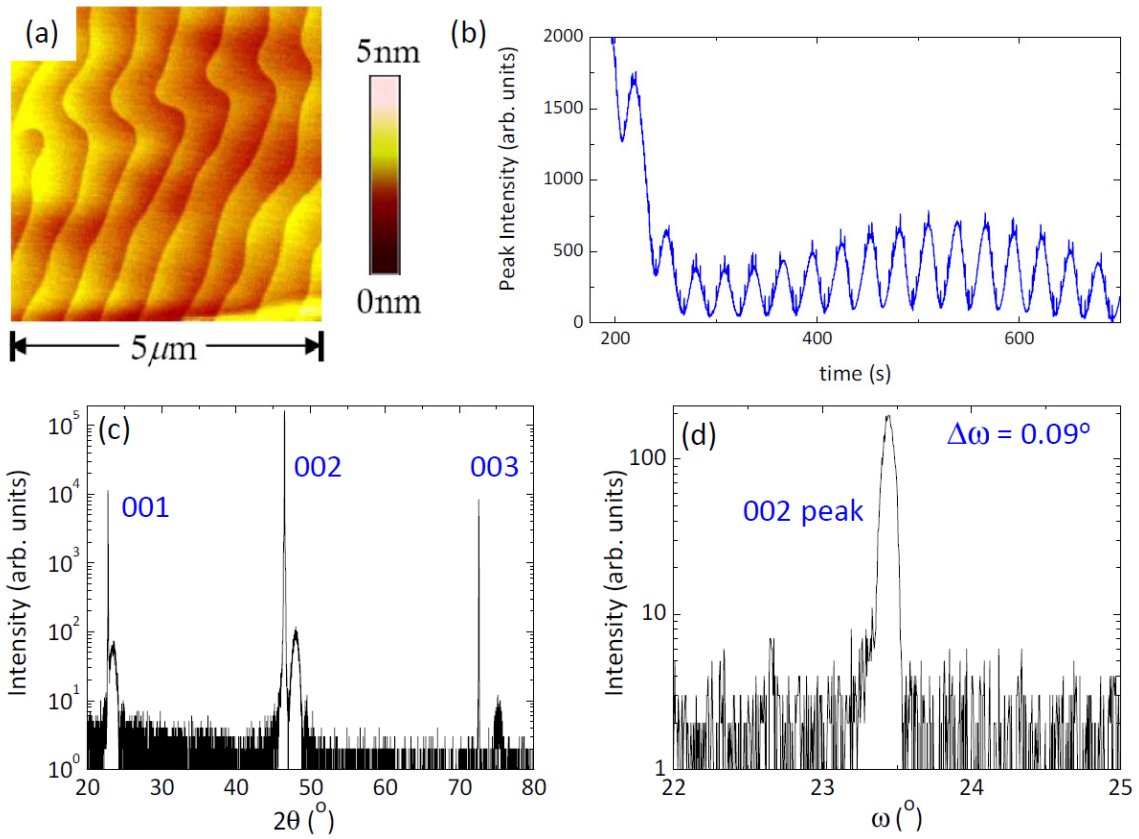

Figure 6.3. (a) Atomic force microscopy image of a typical $LaAlO_3$ film grown on a TiO_2-terminated (001) $SrTiO_3$ substrate. (b) Oscillations of a reflective high energy electron diffraction spot during the growth a representative 8 nm $LaAlO_3$ film on a TiO_2-terminated $SrTiO_3$ substrate. (c) Out-of-plane 2θ scan and (d) ω scan of the 002 reflection of a 10 nm $LaAlO_3$ film.

Both the samples show higher carrier concentration at higher temperatures (Fig. 6.4a), and the most dramatic increase occurs between 20 and 120 K; this temperature range corresponds to that in which the dielectric permittivity of $SrTiO_3$ changes drastically [38]. To create a conductive channel confined to an interface, it is not surprising that band bending at the heterointerface—strongly affected by the dielectric constant—should be important. So the correspondence of carrier concentration and dielectric constant further suggests that metallicity is an intrinsic interfacial phenomenon, rather than conduction in bulk $SrTiO_3$ as had been previously suggested [4,5]. In degenerately doped bulk $SrTiO_3$,[⌗] the carrier density does not show this temperature correspondence [16]. Lightly doped $SrTiO_3$ can exhibit a temperature-dependent carrier freeze-out behavior [17], but it is noticeably different from the behavior observed in the transport features reported here, in which the carrier

[⌗] Tufte *et al.* showed degenerately doping of $SrTiO_3$ by both Nb substitution in the Ti site and oxygen vacancies [16]. Nb doping resulted in higher carrier mobility.

concentration from 2 to 300 K changes by a factor less than 5. Therefore, the metallicity should be understood as a $LaAlO_3/SrTiO_3$ heterointerfacial conductive channel and not as just a doped bulk material.

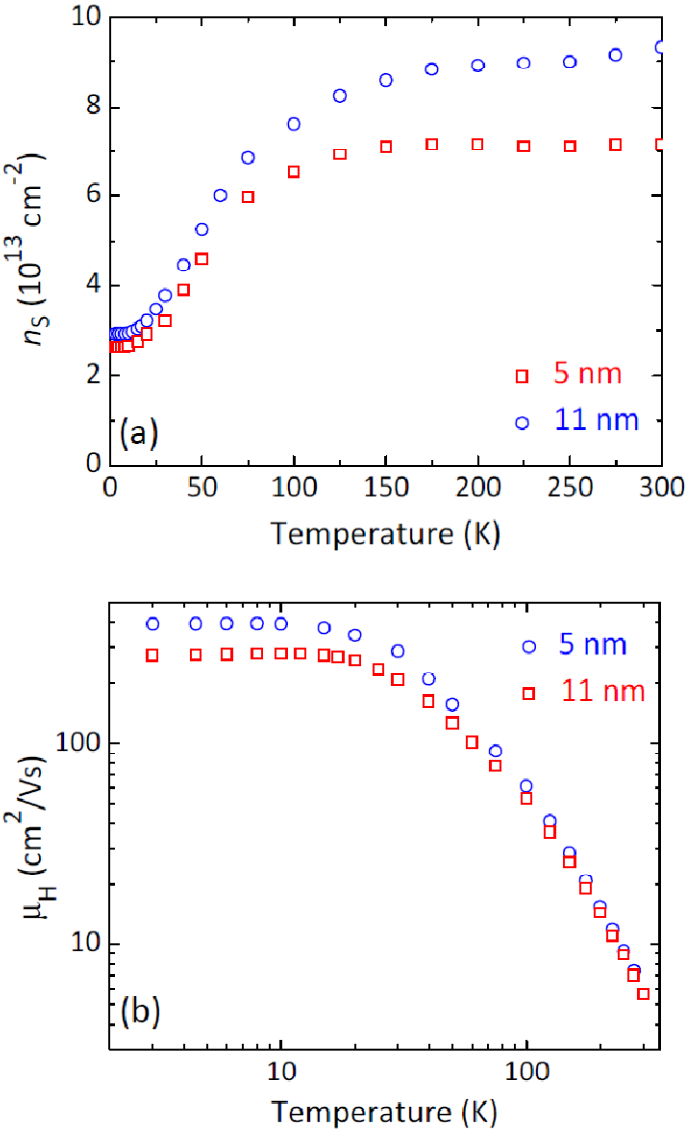

Figure 6.4. Temperature dependence of the (a) sheet carrier concentration and (b) mobility of heterointerfaces formed by a 5 nm and an 11 nm $LaAlO_3$ film on $SrTiO_3$ substrates.

Neglecting the possibility of electron correlations, the two most important parameters of a metallic state are carrier concentration and disorder. Different $LaAlO_3$ film thicknesses can be used to achieve samples with varying sheet carrier concentration values. Figure 6.5 shows the sheet carrier concentration at 275 K of different samples as a function of film thickness. The thinner films generally have lower sheet carrier

(electron-like) concentration for $LaAlO_3$ film thickness values up to 5-6 nm, above which the sheet carrier concentration does not seem to have an obvious trend with film thickness.

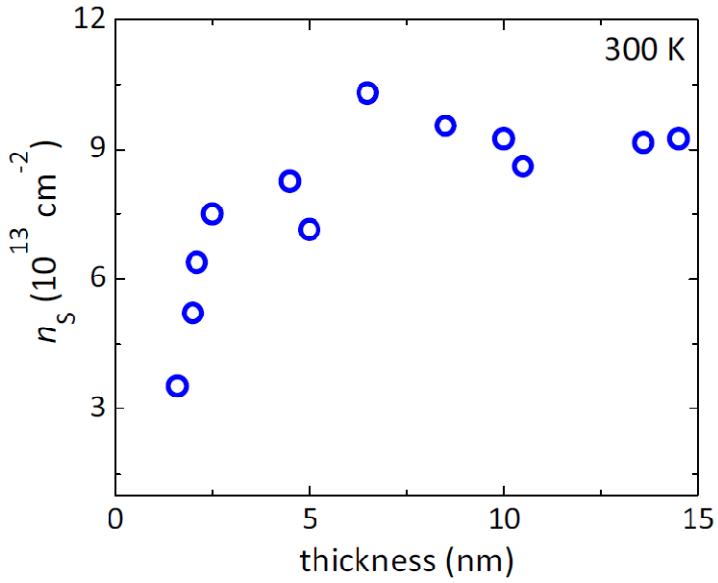

Figure 6.5. Sheet carrier concentration values at 275 K for heterointerfaces of different $LaAlO_3$ film thickness.

There is special emphasis on low-temperature transport behavior, because of its sensitivity to disorder. Electrical transport data at 3 K show a general trend of decreasing electron mobility with increasing interfacial sheet carrier concentration (Fig. 6.6). At low temperatures where inelastic scattering is minimized, the mobility is a measure of the degree of disorder associated with static elastic scattering sites. The mobility values reported here are comparable to those observed by other groups [7,8,21-24,27,28,29]. These values are considerably less than those of electron-doped $SrTiO_3$ crystals, ranging from ~1,000 to 5,000 cm^2/Vs for oxygen vacancy doping and ~3,000 to 20,000 cm^2/Vs for Nb doping [16]. Due to the high permittivity of $SrTiO_3$ at low temperatures, carriers can exhibit respectable mobility values, despite not being "clean" by electronic materials standards. Nevertheless, the implication of Ohtomo and Hwang's proposal was to mimic modulation doping in semiconductor heterostructures through polar instability [1]. Therefore, it should not be overlooked that heterointerface mobility values are in fact lower than those routinely attained in bulk crystals forty years ago. Presumably, the crystal quality of today's commercial substrates is better. The lower interfacial mobility values obtained in the $LaAlO_3/SrTiO_3$ heterointerfacial metallic channels suggest that the origins and effects of disorder must be investigated.

The increase in sheet carrier concentration that is coincident with a decrease in mobility, and hence an increase in disorder, suggests that the generation of carriers is

associated with a greater density of scattering centers or enhanced scattering. Because the combination of carrier concentration and mobility, not the film thickness, governs the features of low-temperature electrical transport, the samples herein are labeled by their carrier concentration and mobility values and not their film thicknesses. The focus is specifically on four samples (A to D), whose transport parameters are listed in Table 6.1.

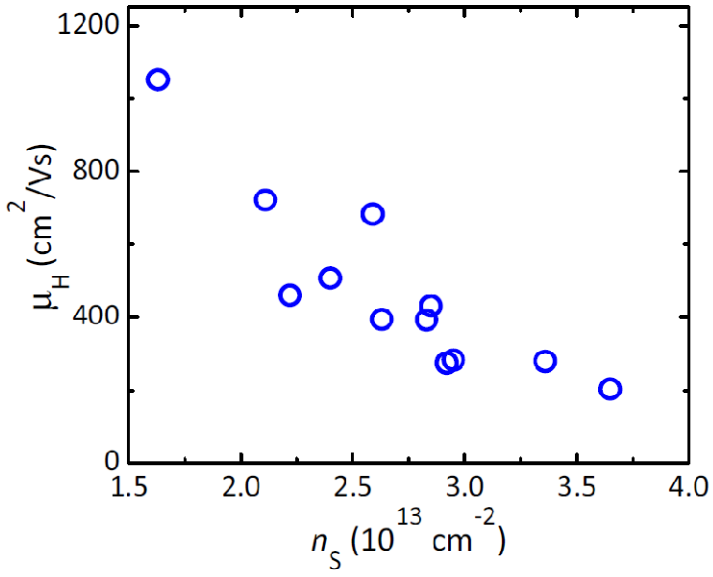

Figure 6.6. Mobility versus sheet carrier concentration at 3 K for the different samples.

Table 6.1. Transport properties of samples A to D at 3 K: sheet carrier concentration n_S, Hall mobility μ_H, electron diffusivity D, carrier mean free path l, and $LaAlO_3$ film thickness t.

Sample	n_S (cm^{-2})	μ_H (cm^2/Vs)	D (cm^2/s)	l (nm)	t (nm)
A	3.65×10^{13}	203	5.92	20.3	11
B	2.92×10^{13}	273	6.37	24.4	13.5
C	2.63×10^{13}	393	8.27	33.3	5
D	1.63×10^{13}	1052	13.7	70.2	4

§ 6.5 Low-temperature quantum correction to conductance

Low-temperature transport data of samples A to D reveal upturns in sheet resistance that are more pronounced and occur at higher temperatures in samples with higher carrier

concentration (Fig. 6.7a). In this temperature regime, the higher carrier concentration, lower mobility samples are more resistive. Both weak localization [21] and Kondo scattering [8] have been invoked to explain the existence of such sheet resistance minima. The anisotropy in the MR data presented in the next section suggests that Kondo scattering is not the operative mechanism in the samples presented here. On the other hand, the upturn in resistance may be related to enhanced coherent backscattering, which can be treated as a quantum correction to the Drude conductance. See Appendix A.2 for details. Localization effects are typically more pronounced for lower dimensional systems, such as heterointerfacial conducting channels. The resistance upturn can be converted to conductance correction values, using the minimum sheet resistance R_S^{min} as a reference: $\Delta\sigma = [R_S^{min}-R_S(T)]/R_S^{min}R_S(T)$ (Fig. 6.7b). In a sheet resistance versus temperature plot, the best estimate of the Drude component is the minimum resistance value. Whereas the sheet resistance values and the magnitude of the sheet resistance upturn appear to vary substantially from sample to sample, the values for the correction to conductance of all of the samples are on the order of $pe^2\ln 10/\pi h = 5.7 \times 10^{-5}\ \Omega^{-1}$ per decade for $p = 2$. The inelastic scattering time τ_{in} scales with an inverse power law with respect to temperature T, $\tau_{in} \propto T^{-p}$, and $p = 2$ corresponds to a Fermi liquid. This is not an unexpected state for electron-doped $SrTiO_3$ at low temperatures. Although the curves of the quantum correction to conductance do not have a strict logarithmic dependence with temperature, as would be expected for weak localization, localization phenomena cannot be completely dismissed in describing the low-temperature electrical transport data. In fact, electron-electron correlation, spin-orbit interaction, and possible long-range ordering may account for the deviation from a purely logarithmic temperature dependence.

§ 6.6 Magnetotransport and its anisotropy

Magnetotransport measurements provide additional insight into the role of disorder and localization effects. Unlike in Chapter 5, in which MR is a desired functionality, here magnetotransport is utilized solely as a means to study the effects of coherent backscattering and disorder in the metallic regime of a quasi-two-dimensional system at low temperatures. Figure 6.8a shows the MR curves of samples A to D at 3 K with the magnetic field applied normal to the sample plane. A closer examination of the out-of-plane MR of sample A, with the highest carrier concentration, reveals that at lower temperatures, e.g. 2 K as shown in Fig. 6.8b, a cusp at lower fields emerges, and it disappears at 12 K.

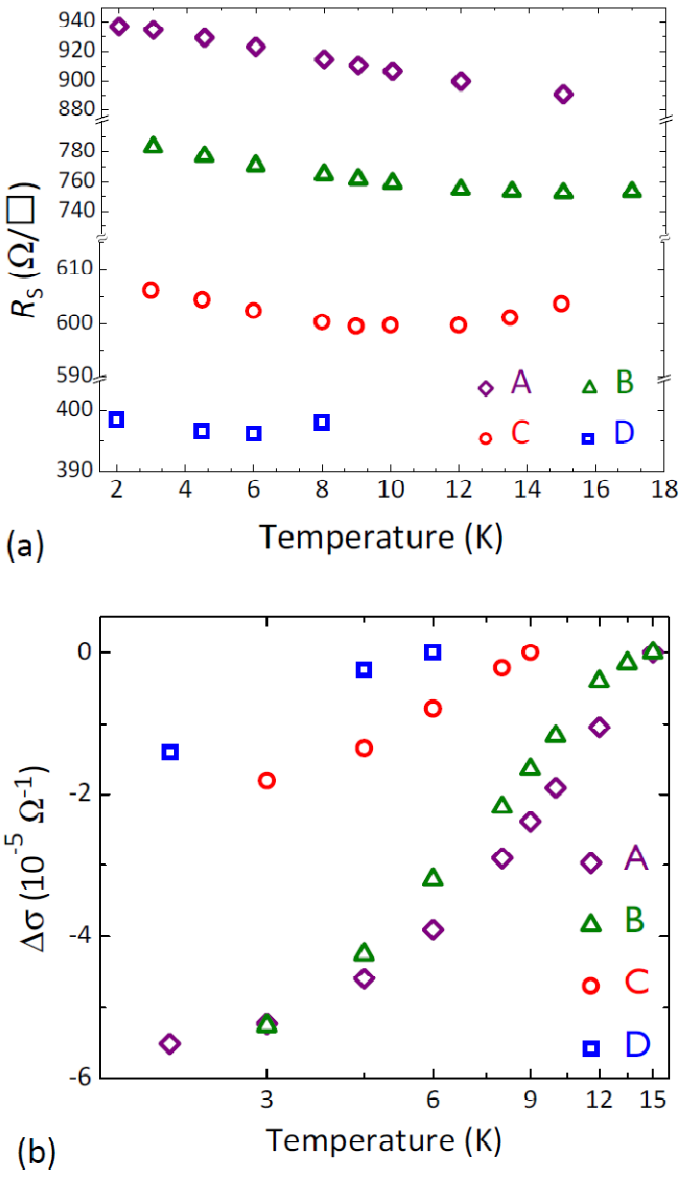

Figure 6.7. (a) Sheet resistance and (b) corresponding conductance correction of samples A to D in a range of low temperatures.

In contrast, sample D does not show any similar low-field cusplike behavior. The positive MR as seen in sample D is attributed to orbital motion of carriers, often called "ordinary MR." Ordinary MR arises from the semiclassical effect of electrons being deflected away from their paths due to the Lorentz force of the applied magnetic field on moving charged particles. Ordinary MR follows Kohler's rule: MR = $F(H/\rho) \approx F'(\mu H)$, where H is the magnetic field, ρ is the resistivity, and F and F′ are monotonic functions

that increase with μH. Electrons travel along their cyclotron orbits until they scatter and then restart their paths along the direction of the electric field. Therefore, scattering events limit the magnitude of ordinary MR. A higher magnetic field induces tighter orbits.[§§] Indeed the positive MR is higher with increasing fields and in higher mobility samples.

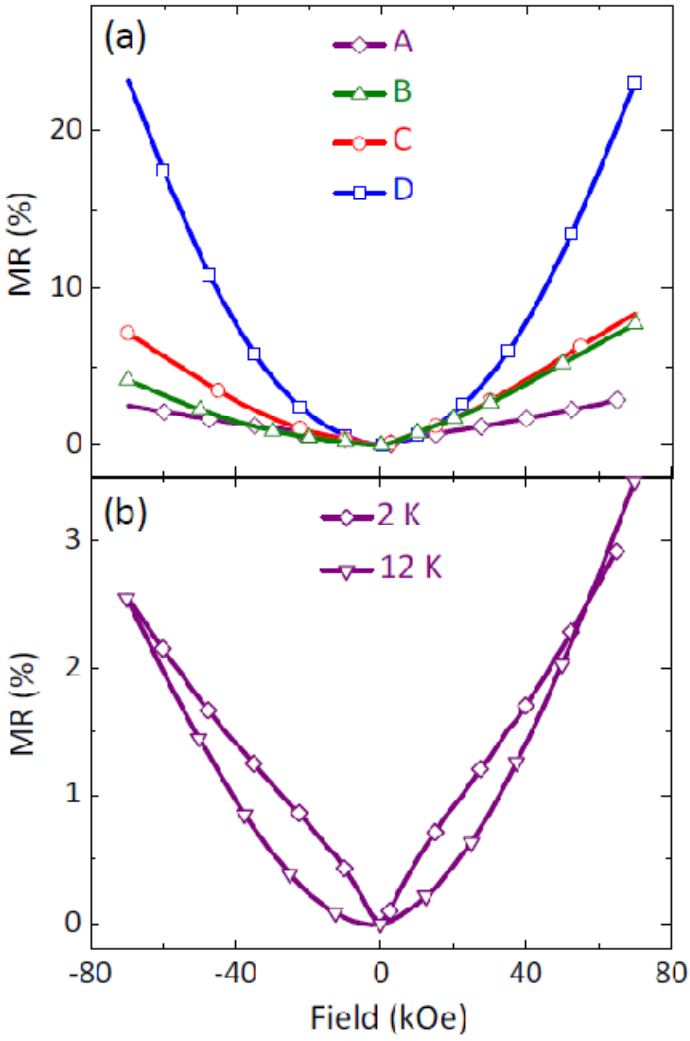

Figure 6.8. (a) Out-of-plane MR of samples A to D at 3 K and (b) of sample A at 2 and 12 K.

The functional dependence of MR on μH is examined. Because the asymmetry of the MR in positive and negative fields (can be seen in Fig. 6.8) is due to geometric and

[§§] In the limiting case of extremely clean samples and at very low temperatures, carrier scattering rates are very low; the application of a magnetic field can generate a quantum Hall state of no dissipation yet no electrical conduction through the bulk.

not intrinsic effects, averaged MR values for corresponding positive and negative fields (MR_{ave} = ½ [MR(H) + MR(-H)]) were used to construct a Kohler plot for sample D at 3 K and 60 K (Fig. 6.9a). Despite the seemingly high fields applied, $\omega_c\tau = \mu_H\mu_0 H < 1$, corresponding to the low-field limit. If only ordinary MR is present, one expects the Kohler plot data of the two temperatures to lie on the same line, as ordinary MR should be only a function of μH; the function behaves the same if the field were increased or if the mobility were increased by the same amount due to the lowering of temperature. Therefore, the data in Fig. 6.9a suggest that there must be other temperature-dependent contributions to MR. Experimentally, MR is commonly found to be of the form $\kappa(\mu_H\mu_0 H)^\beta$. In the high-field limit, the determination of the sample orientation dependence of β is often used to map out the topology of the Fermi surfaces of metals, but there is no universal low-field value for β [39]. Likewise, there is no universal prefactor κ, particularly in the low-field limit [39]. To be as general as possible, we allow both κ and β to be fitting parameters for field-dependent resistivity curves measured at different temperatures. Fits were performed on the MR data from 20 to 70 kOe. At 3 K, κ = 0.49 and β = 1.98, whereas at 60 K, κ = 1.00 and β = 1.89. At higher temperatures, the MR values are so low that fits are not as reliable. A low-field-limit exponent β close to 2 can be theoretically calculated assuming a two-carrier model [39]. However, in the $LaAlO_3/SrTiO_3$ metallic heterointerface, it is unclear whether there are two relevant carriers that contribute to electrical conduction. Therefore, in this case, the fitted exponents are taken just as phenomenological parameters.

The temperature dependences of the phenomenological κ and β values (Fig. 6.9b) have to be rationalized, as they suggest that the out-of-plane MR in this system is not governed by just changing mobility values. In contrast to metallic thin films, the carrier concentration and therefore the Fermi level of the interfacial $LaAlO_3/SrTiO_3$ metallic channel is dependent on temperature, as shown in Fig. 6.4a. As the carrier concentration increases with increasing temperature, though the electron scattering rate increases, so does the Fermi velocity. This effect may explain higher κ values at higher temperatures. Another reason for temperature dependences of the fitting parameters is the contribution to MR from localization effects at lower temperatures, as will be discussed in the next section. The temperature dependence of the β values, which typically are slightly less than 2, is relatively weak. Nonetheless, the scaling of out-of-plane MR with sample mobility and applied field suggests that while ordinary orbital effects are not the only contribution, they are the most dominant one.

It is shown that the out-of-plane MR of even the highest mobility sample (sample D) may be affected by disorder-induced weak localization. Lower mobility samples exhibit more pronounced effects. The cusplike MR feature of sample A in Fig. 6.8b is believed to be a signature of disorder. However, the ordinary MR component overwhelms other contributions.

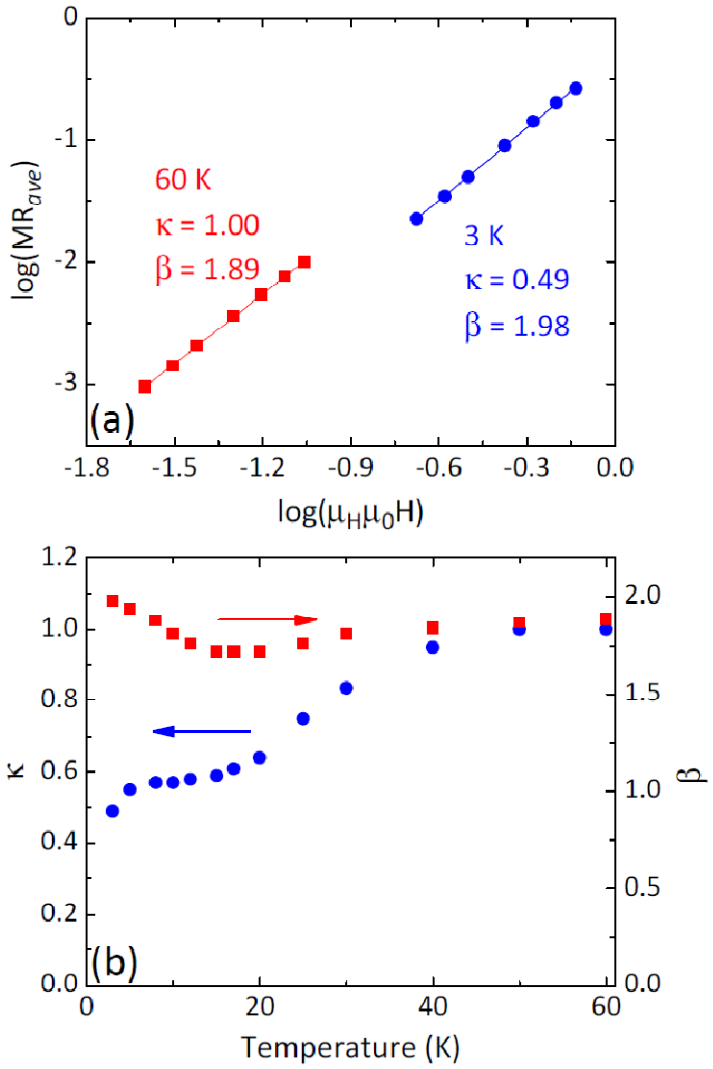

Figure 6.9. (a) Kohler plots of the out-of-plane MR of sample D at 3 and 60 K and their corresponding fitting parameters. (b) Temperature dependence of the fitting parameters of the out-of-plane MR = $\kappa(\mu_H\mu_0 H)^{\beta}$.

Magnetotransport with applied fields parallel to the interface allows for separating out orbital effects from the MR. In-plane MR measurements were performed in the van der Pauw geometry, with the field applied 45° with respect to both the in-plane [100] and [010] directions. In this geometry, there appears to be no ordinary MR contribution (Fig. 6.10a) for all of the samples, because the Lorentz force for a field applied in plane cannot send electrons into cyclotron orbits as a field applied out of plane does. The ability to suppress the ordinary MR contribution in in-plane measurements suggests that the thickness of the interfacial metallic layer is within one carrier mean free path. This finding is consistent with the work of Basletic *et al.* [15]. Using an isotropic, parabolic band approximation, the mean free path of sample A, for example, is

estimated to be 20.3 nm (Table 6.1). The electron mean free path l can be calculated from the measured mobility μ and sheet carrier concentration n_S values,

$$l = \frac{\mu\hbar}{e}\sqrt{2\pi n_S}$$

for a quasi-two-dimensional system. The mean free paths of the other samples can be likewise computed, and they are given in Table 6.1. All in all, the MR anisotropy illustrates the quasi-two-dimensional nature of metallicity at the $LaAlO_3/SrTiO_3$ interface. The MR curves of Fig. 6.10a reveal two distinct regimes, a positively sloped MR portion in lower fields and negatively sloped in higher fields, resulting in a local MR maximum. Note that the low-field positive component is barely visible in sample D, with the lowest carrier concentration. Fig. 6.10b shows that the positive MR contribution increases with decreasing temperature and is most likely linked to the cusp observed in sample A at 2 K (Fig. 6.8b). Similar to the cusplike feature of the out-of-plane MR as shown in Fig. 6.8b, Fig. 6.10b shows that the positively sloped portion of the in-plane MR is a low-temperature phenomenon that gradually disappears at higher temperature. The field corresponding to the positive local maximum in MR is referred to as H^*, and a temperature dependence plot of H^* explicitly shows the disappearance of a contribution to the MR at higher temperatures (Fig. 6.10c).

§ 6.7 Possible origin of disorder and spin-orbit interaction

Both the resistivity upturn and the negative MR components are reminiscent of localization effects arising from disorder. Disregarding electron-electron interaction for the moment, the two key parameters to keep track of are electron concentration and disorder. A higher-density sea of electrons results in greater kinetic energy and electronic bandwidth. Physically, one can imagine that the electrons in a higher carrier density sample have larger velocities because of better screening. In terms of disorder, fluctuations of potential as compared to that of a perfect lattice perturb the Bloch electron waves and can give rise to carrier localization. A metal-insulator transition that comes about through reduced carrier concentration is called a Mott transition, and one that comes about through increased disorder is called an Anderson transition. In the case of doped semiconductors, impurities and carriers are introduced concurrently; therefore, carrier concentration and mobility tend to have an inverse relationship. It will be shown that in the case of metallic $LaAlO_3/SrTiO_3$ electron channels induced by interfacial polarity, carrier concentration and disorder likewise cannot be decoupled. It will be argued that carriers and charged scattering centers are introduced concomitantly through interfacial polar instability.

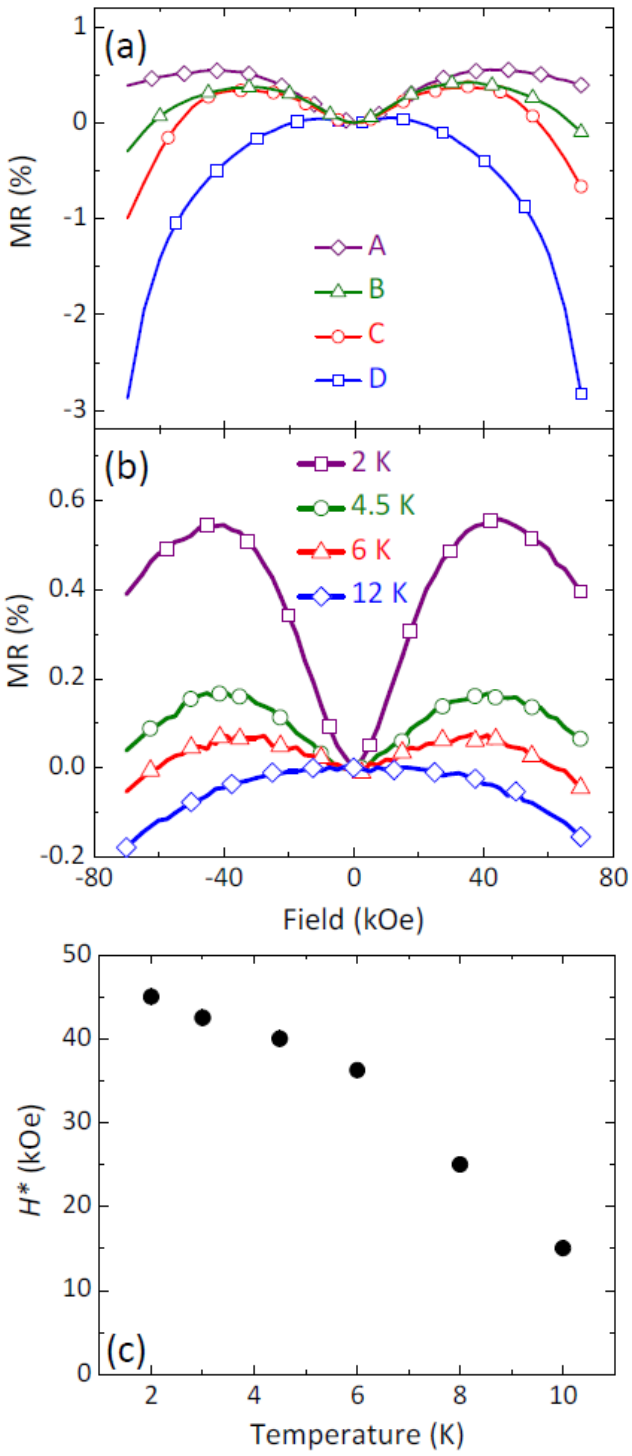

Figure 6.10. (a) In-plane MR of samples A to D at 2 K. (b) In-plane MR of sample A at various temperatures. (c) Temperature-dependent crossover field, as defined in the text, in the in-plane MR of sample A.

First off in the perfect two-dimensional materials, Abrahams *et al*. have shown that there can be no true metallic low-temperature state [40].*** However, Abrahams *et al.* consider a system of spinless, noninteracting electrons at 0 K. Moreover, in the temperature regime of interest, strong localization is not yet in effect, and weak localization can be treated as a perturbation to metallic conductance—hence the quantum correction to the Drude conductance in Fig. 6.7b.

The quasi-two-dimensional nature of *n*-type metallic conduction as suggested by the anisotropy in magnetotransport requires interfacial band bending that provides for electron confinement, i.e. downward bending of the conduction band of $SrTiO_3$ near the interface. The lowering of the conduction band of $SrTiO_3$ may be related to interfacial bonding [41] or strain/interfacial-induced polar distortions [42]. These possibilities are similar to the proposed mechanisms for metallicity in nitride heterojunctions [34-36]. However, the possibility of trapped point-like positive interface charges on the $LaAlO_3$ side of the heterojunction and their origin are considered. Beyond the critical $LaAlO_3$ film thickness of four unit cells for an insulator-metal transition [3], the $LaAlO_3$ valence band edge becomes higher in energy than the conduction band edge of $SrTiO_3$, and electrons tunnel to the $SrTiO_3$ side, where they can become mobile. The energy band configuration is shown schematically in Fig. 6.11, and the band offsets reported by Lee and Demkov were used [13]. The dielectric constant of $LaAlO_3$ is $\sim 25\varepsilon_0$. If the charge density on the $LaAlO_3$ side as shown in Fig. 6.1 is assumed to alternate between $\pm e/2a^2$ were a is the lattice constant of $SrTiO_3$, an insulator-metal transition at 4 unit cells can be calculated. Since the conjecture is that the valence band of $LaAlO_3$ supplies electrons to $SrTiO_3$, there should be holes in $LaAlO_3$. In this work, a second conjecture is made: the holes in $LaAlO_3$ are immobile, and rather than being carriers themselves, they act as scattering centers for electrons in $SrTiO_3$. The speculation of immobile holes is plausible. First, the formation of hole polarons has been considered and thought to be likely in related oxides [12]. Second, the author is not aware of any successful incorporation of electrically active dopants (neither *n*- nor *p*-type) in $LaAlO_3$. Localized holes in $LaAlO_3$ near the interface, starting from 4 unit cells away, can enhance band bending at the heterojunction, thus confining the electron channel to be quasi-two-dimensional. A possible band alignment situation is shown in Fig. 6.12. At the same time, these holes can also act as scattering centers that limit the magnitude of low-temperature carrier mobility and may be the relevant form of disorder here.

Despite the simplicity of the band alignment arguments presented, they are fully consistent with the experimental results in this study as well as other published data. Before discussing the results here, brief mention of other works will be made. The band alignment description holds for a *p*-type $(AlO_2)^-/(SrO)^0$-terminated $LaAlO_3/SrTiO_3$ heterointerface except for that the electrons will be in $LaAlO_3$ and holes in $SrTiO_3$. To date, there has been no successful electrically active *p*-type doping of $SrTiO_3$ at room temperature or lower temperatures; therefore, despite the similar electronic instability-

*** A true metallic state is defined as having finite conductance at a temperature of absolute zero, whereas an insulator state has zero conductance.

induced interfacial charge redistribution, the *p*-type interface remains insulating. Furthermore, there has been a very recent report of electron-like metallicity in $LaGaO_3/SrTiO_3$ heterointerfaces [43]. The dielectric constant of $LaGaO_3$ is ~$26\varepsilon_0$ [44] and its band gap is ~5 eV, though there is no widely accepted value. Under the same deposition conditions, Perna *et al.* found that $LaGaO_3/SrTiO_3$ interfaces have even higher conductivity than $LaAlO_3/SrTiO_3$ interfaces. It is possible that higher conductivity is a result of lower lattice mismatch; the pseudocubic lattice parameter of $LaGaO_3$ is 3.89 Å [45], that of $SrTiO_3$ is 3.905 Å, and that of $LaAlO_3$ is 3.79 Å. They also showed that despite the nominally identical valence state, $LaMnO_3/SrTiO_3$ interfaces are not metallic. As mentioned in Section 5.2, $LaMnO_3$ is a Mott insulator with a considerably smaller gap. From the schematic of polar interface electronic instability shown in Fig. 6.11, it can be deduced that the band offsets and band gaps are crucial to forming a metallic channel in $SrTiO_3$ through interfacial polarity. The criterion should be that the conduction band edge of the other insulator must be higher in energy than that of $SrTiO_3$.

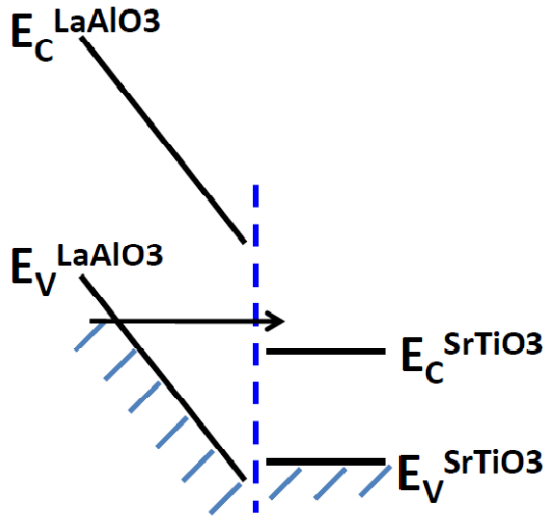

Figure 6.11. Schematic of the increase in electronic energy as the $LaAlO_3$ layer becomes thicker. Eventually, the valence band electrons in $LaAlO_3$ can tunnel to the conduction band of $SrTiO_3$.

The assumption of localized holes in $LaAlO_3$ being the source of carriers at the interface as well as elastic scattering centers accounts for the observed trend of higher carrier concentration accompanied by reduced low-temperature mobility in thicker films (Figs. 6.5 and 6.6). Localized holes constitute the dominant source of disorder. When the film thickness becomes larger than the physical extent of band bending on the $LaAlO_3$ side, the carrier concentration levels off with further increase in film thickness; this explains the saturation of carrier concentration for film thicknesses greater than

about 5-6 nm (Fig. 6.5). It is emphasized that other forms of interfacial charges and any interfacial bonding effects [41,42] can also directly influence interfacial band bending and can readily be incorporated into this description.

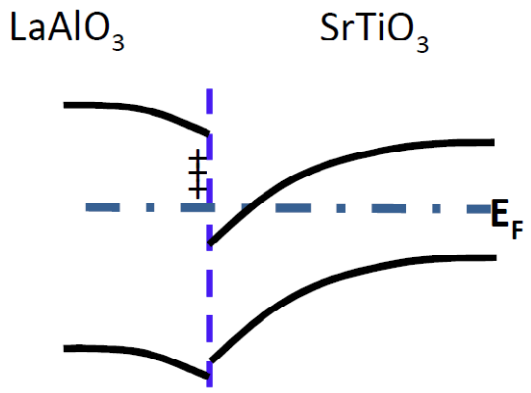

Figure 6.12. Schematic of a possible band bending situation after the generation of metallicity on the $SrTiO_3$ side of the heterointerface.

In the localization problem of interest, both of the relevant parameters—carrier density and degree of disorder—are higher in samples of thicker $LaAlO_3$ films. It is not obvious, *a priori*, whether this quasi-two-dimensional system is approaching or moving away from the localized regime with increased carrier concentration. The lower conductance values exhibited in the samples with the thicker films suggest that the stronger scattering has a greater effect than the higher carrier concentration.

The upturn in sheet resistance and the in-plane MR features may be explained by weak localization effects. We speculate the negative MR observed in sample D, for example, to be attributed to weak localization, to which all two-dimensional materials with any degree of disorder are susceptible. This negative component to MR may be related to the smaller κ in the fit to the ordinary MR component of the out-of-plane MR at 3 K compared to that at 60 K. The positive ordinary component to MR conceals but is reduced by the negative contribution due to localization effects, thus leading to smaller κ values at lower temperatures (Fig. 6.9b). However, the temperature variation of β is still unaccounted for. The visibility of localization features indicates the in-plane magnetic fields can still dephase carriers, signifying there is definitely some finite thickness to the metallic channels. While out-of-plane positive MR is easily measureable at 60 K, in-plane MR disappears above roughly 20 K for sample D, suggesting that the in-plane MR features are indeed dominated by electron coherence effects that are suppressed in the presence of temperature-activated inelastic scattering, and the out-of-plane MR curves are not.

As the carrier concentration increases from sample D to sample A, a positive MR component gradually emerges (Fig. 6.10a). A crossover from positively to negatively sloped MR similar to that exhibited by sample A below 12 K has been observed in a number of two-dimensional disordered metals with crossover fields as high as 8 kOe in Bi films [46] and above 25 kOe in Au films [47]. This feature is attributed to antilocalization effects owing to increasing spin-orbit interaction [48,49] from sample D to A. A discussion of the contribution of spin-orbit interaction in low-temperature magnetoresistance in disordered materials can be found in Appendix A.2. Whereas $SrTiO_3$ does not contain particularly heavy elements, spin-orbit interaction can be strengthened by heterointerfacial and surface electric fields [50,51]. For the polar $LaAlO_3/SrTiO_3$ heteroinference, the interfacial electric field is enhanced by the accumulation of mobile electrons on the $SrTiO_3$ side and trapped holes on the $LaAlO_3$ side. Cavigilia *et al*. reported similar H^* values over a range of gate voltages at 1.5 K [23]; since the mobility value, as deduced from the reported electron diffusivity, of their sample at zero bias is comparable to that of sample A and they performed measurements at a similar temperature, the spin-orbit scattering times τ_{so} should likewise be comparable. For two-dimensional conduction and with an isotropic, parabolic band approximation, electron diffusivity D and mobility μ are related by:

$$D = \frac{\hbar^2 \pi n_s \mu}{em}$$

where m is the conduction band effective mass of $SrTiO_3$. The diffusion coefficients of sample A to D are listed in Table 6.1. Treating electron transport as a diffusion problem and using diffusivity as the key transport parameter, one can see that indeed the localization effects are more pronounced in the higher carrier concentration interfaces. For conduction band electrons in $SrTiO_3$, m is estimated to be $3m_0$, three times the bare electron mass; the same estimation is made by Caviglia *et al*. [23]. Weak (anti)localization is treated in terms of an electron diffusion problem in Appendix A.2.

Quantitative extraction of τ_{so} and the electron dephasing time τ_ϕ of our samples is complicated by the lack of a precise measurement of the exact metallic channel thickness [46]. Regardless, the temperature dependence of MR allows for comparison of the relative rates of spin-orbit and inelastic scattering. We expect the dominant carrier dephasing mechanism to be inelastic scattering. As mentioned before, $\tau_{in} \propto T^{-p}$, where $p = 2$ for a Fermi liquid and $p = 5$ for a nearly free electron gas scattered by acoustic phonons. Antilocalization effects in sample A are visible when τ_{so} is less than τ_{in}, and therefore disappear at higher temperatures, as in Fig. 6.10b. Physically, when $\tau_{in} < \tau_{so}$ an electron loses phase coherence before it undergoes a spin-flip scattering event; therefore, antilocalization effects are lost. In sample A, this crossover occurs at about 12 ± 2 K, below which the spin-orbit scattering rate $1/\tau_{so}$ is higher.

The interdependent generation of carriers on the $SrTiO_3$ side and disorder near the interface appears to be a defining feature for intrinsic polarity-induced interfacial metallicity. The results present here show an inverse relationship between carrier

concentration and mobility, thus suggesting that among these samples the higher sheet carrier concentration metallic channels either are thinner spatially or contain more scattering centers. The hypothesis of localized interfacial holes can be reconciled with both possibilities. The trend reported here is in sharp contrast to gate-voltage modulated carrier concentration studies reported by Bell *et al*. [22] and Caviglia *et al*. [23]; in those samples, the disorder is held constant and carriers become more mobile as the density increases. However, the dependence of the dielectric constant of $SrTiO_3$ on carrier concentration and interface electric field [38] cannot be ignored and needs to be examined for a more complete description.

In summary, the comparative study of different samples whose interfacial conductivity is induced purely by interfacial polar instability suggests the concomitant generation of carriers and disorder in $LaAlO_3/SrTiO_3$ heterointerfaces. In fact, Caviglia *et al*. reported very recently high mobility channels ($\mu \sim 5000$ cm^2/Vs) can be achieved only in considerably lower carrier density samples ($n_S \sim 5\times10^{12}$ cm^{-2}) [29]. While the materials control of these samples has not reached the point of precise engineering of carrier concentration from sample to sample, the clear relationship of carriers and disorder sheds light on the origins and potential tunability of interfacial metallicity.

§ 6.8 Exploiting spin-orbit interaction

In 1990, Datta and Das proposed a field-effect spin modulator tunable with gate-controlled spin-orbit interaction, now commonly referred to as a spin transistor, and it still remains a heavily pursued device structure [52]. Phenomenologically, spin-orbit interaction of carriers is best exemplified by the spin Hall effect: as a result of a current flowing along a particular direction, a spin imbalance along a transverse direction is induced, because the probability of a scattering event with a certain change of momentum vector of the carrier depends on its spin. The spin Hall effect can have both intrinsic and extrinsic components [53]. It is believed that the dramatic spin-orbit interaction features shown in the data reported in this study and in other works [23,24] are intrinsic in that they are attributed into the band structure of $SrTiO_3$ coupled with the large electric fields at the interface. Detailed studies of the band structure effects on spin-orbit interaction in $SrTiO_3$ and related oxide materials have yet to be performed, but the triple degeneracy at its conduction band edge (at the Γ point)[†††] is a characteristic ingredient for strong spin-orbit coupling.

Spin-orbit interaction is both a blessing and curse for spintronic applications. There has been much investigation on low atomic number nanomaterials such as carbon nanotubes specifically to avoid spin-orbit coupling for spin-preserving electron transport over long distances [57]. Strong spin-orbit interaction renders spin a poor quantum

[†††] $SrTiO_3$ has an indirect band gap. The conduction band edge is at the Γ point, and the valence band edge is at the R point [54,55]. The indirect band gap can be measured optically [56].

number, and makes the total angular momentum with both spin and orbital contributions the more relevant quantum number. More physically, as carrier electrons evolve in time, their spin states can be preserved over only extremely short times, limited to τ_{so}. On the flip side, if one wants to direct the flow of electrons depending on their spin states, spin-orbit interaction is absolutely necessary.

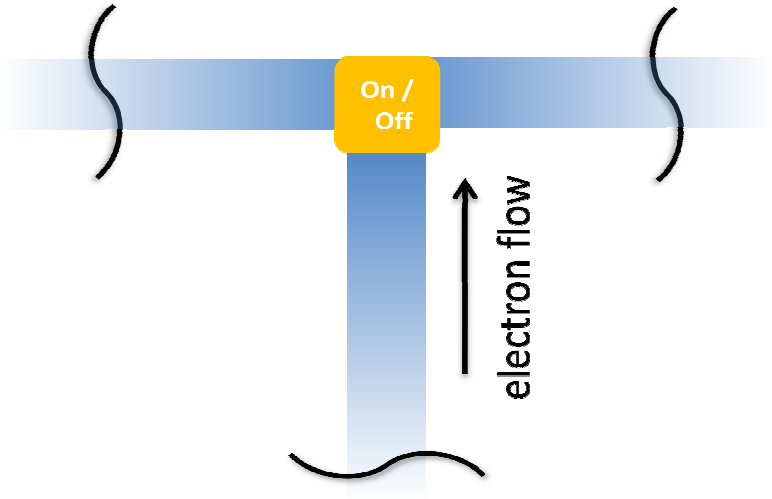

Figure 6.13. Schematic of a juncture structure that may exploit the effects of tunable spin-orbit interaction at the juncture.

It would be optimal to take advantage of a spin Hall-like effect by specifically designing the location of tunable spin-orbit coupling and elastic scattering. This section ends with a proposal of a structure that can exploit spin-orbit scattering. If there is a T-juncture structure (Fig. 6.13), the current-carrying electrons that have a net momentum along the straight segment will have to, on average, change their momenta to the left or right when they reach the juncture. Weak spin-orbit interaction along the straight segment allows for the preservation of spin until they reach the juncture. If at and near the juncture the spin-orbit coupling is strong, carriers of one spin can preferentially be sorted to one direction—creating a spin imbalance between the left and right sides. If one can inject a spin-polarized current, then a voltage difference will result between the left and right sides—often referred to as the inverse spin Hall effect. Conversely, if the spin-orbit coupling at the juncture can be turned off, no spin imbalance will result. The key is tunability specifically at the juncture. Caviglia *et al.* have demonstrated viability of using a gate voltage for tuning the strength of spin-orbit scattering [23]. In the spirit of using AFM tip to sketch structures on $LaAlO_3/SrTiO_3$ samples as reported by Cen *et al.* [25], it would be also interesting to place impurity atoms or create local electric fields at select locations where junctures structures can be directly sketched; the designed placement of

impurity atoms would take advantage of the extrinsic spin Hall effect [53]. This type of structure would be optimal if carrier spins flip primarily due to the Elliot-Yafet mechanism. The relevant spin-flip mechanisms in $LaAlO_3/SrTiO_3$ heterointerfaces need to be further investigated.

§ 6.9 Conclusions and outlook

A comparative study of samples of different mobility values has allowed for a reasonable speculation of the origin of carrier electrons at $LaAlO_3/SrTiO_3$ heterointerfaces, which had not been appropriately addressed. The concurrent introduction of carriers and disorder suggests that there may be localized holes in $LaAlO_3$ that both spatially confine the electron channel in $SrTiO_3$ as well as act as scattering centers. The realization of enhanced mobility may be contingent upon increasing the separation between these scattering centers and the carriers.

Based on polar interfacial instability, a metallic channel of carriers experiencing strong spin-orbit interaction is created. The level of materials control in oxide heterostructures definitely cannot yet compete with that of semiconductor heterostructures; hence, carrier mobility in itself is not what makes $LaAlO_3/SrTiO_3$ heterointerfaces attractive. However, there has been much evidence of strong spin-orbit interaction effects, which may related to a combination of the heterointerfacial electric field and the structure of the conduction band of $SrTiO_3$. Such strong spin-orbit coupling cannot be easily attained in conventional semiconductor heterojunctions. In addition to the prospects of engineering spin transport of carriers as speculated in the previous section, recent theoretical proposals have suggested the possibility of a superconducting triplet pairing state that can be achieved in $LaAlO_3/SrTiO_3$ interfaces with high enough spin-orbit interaction [58,59]. Likely there are still many properties in interfacially confined *d*-valent quasi-two-dimensional systems yet to be fully explored.

It is shown that the formation of a polar heterointerface between two nominally undoped wide band gap oxide insulators, $LaAlO_3$ and $SrTiO_3$, can create a quasi-two-dimensional metallic channel. This approach represents a form of band offset engineering and can be further pursued in ionic oxides. If the desired state is a metallic channel, $SrTiO_3$ is a natural material of choice because doping studies of bulk $SrTiO_3$ have demonstrated that it can host free electrons. This cannot be said for many correlated Mott insulators. Band offset engineering of Mott insulators will more difficult to categorize in general terms because band lineups of the upper and lower Hubbard bands of two Mott insulators are not a sufficiently studied topic. Furthermore, the structures of the Hubbard bands depend heavily on the number of *d* electrons, which changes upon interfacial charge transfer. Therefore, many of the implicit assumptions of independent quasiparticle band theory will not hold. Despite the complexity, there is certainly great potential in pursuing interfacial phenomena in correlated systems, wherein new ordered states can arise. For example, there have been interesting results

for generating interfacial ferromagnetism at the interface between two nonferromagnetic oxides [60]. Regardless, to date band offset engineering remains a much more mature approach for materials that are less correlated. In addition to $SrTiO_3$, $KTaO_3$ may be a material of choice because when doped, its carriers (electrons) can also be highly mobile [61]. Incorporating a compound whose conduction band has 5*d* transition-metal character may yet produce many more novel, unexpected phenomena.

Afterword

This dissertation surveyed the work on heterostructures of a single-valent $3d^1$ system ($LaTiO_3$), a mixed valent $3d^{3.67}$ oxide ($La_{2/3}Sr_{1/3}MnO_3$), and a system that does not have $3d$ band electrons its undoped state ($LaAlO_3/SrTiO_3$). Though upon the creation of any heterointerface there surely will be electronic reconstruction, in heteroepitaxial thin films of Mott insulators that contain $3d$ electrons, strain effects may play an even more dominant role. This is the case for strained $LaTiO_3$ and $La_{2/3}Sr_{1/3}MnO_3$ thin films. On the other hand, in transition-metal oxides that start out without $3d$ electrons, interfacial charge transfer can indeed play the most prominent role. This is the case for $SrTiO_3$. Many of the ideas explored in this dissertation can be generally applied to other correlated oxides. Although many such oxides are rather *old* materials, advances in heterostructure growth have opened *new* avenues for investigation.

The pursuit of Mott transistors has motivated much research on electronic phase transitions in oxides. The "off" state of the transistor would be Mott insulating, and the "on" state would be metallic. The temperature-activated insulator-metal transition in VO_2 has been heavily studied [1]. Like $LaTiO_3$, VO_2 is a $3d^1$ material and should be considered as a Mott insulator at low temperatures. However, just above room temperature, it undergoes an insulator-metal transition, and the metallic state is orders of magnitude more conductive. Furthermore, Cao *et al*. demonstrated that as a function of applied stress on VO_2 nanobeams, the transition temperature can be tuned and two-phase metal/insulator coexistence can be stabilized [2]. Strain-induced electronic transitions are expected to be widely applicable to many correlated materials. What was learned from Chapter 4 on strained $LaTiO_3$ thin films is that systems that are not exactly half-filled are susceptible to orbital disorder and metal-insulator transitions. Although this dissertation is an investigation on just perovskite oxides, the possibilities of tuning electronic transitions in orbital disordered Mott insulators should be more general. In addition, Chapter 5 on strained $La_{2/3}Sr_{1/3}MnO_3$ thin films explores how magnetic interactions and the spin state of a material can be linked to metal-insulator transitions. Heteroepitaxial strain can be used as a platform to investigate electronic transitions in

many other oxides. The ability to tune such a transition within a single sample at or near room temperature can be technologically important.

On the interfacial phenomena front, I believe that the progress in complex oxide heterostructure research will be instrumental in extending our understanding of heterointerfaces of correlated electron systems, which is still crude today. $SrTiO_3$ is often categorized as a band insulator, which in its name implies that correlation effects are weak or nonexistent. The rationale behind such a categorization is that we do not need to invoke correlations to explain the insulating state of undoped $SrTiO_3$, because it has no electrons in the 3*d*-like bands. However, such an argument is hardly convincing enough to claim that correlations do not play a role in the conduction band states of $SrTiO_3$—or more precisely, the excited states of $SrTiO_3$. The ability to incorporate electrically active dopants in $SrTiO_3$ and the fact that free electrons in doped $SrTiO_3$ are rather mobile are other "pieces of evidence" suggesting the minor role of correlation effects. Nevertheless, recent scanning tunneling microscopy experiments on metallic $LaAlO_3/SrTiO_3$ interfaces point to the importance of including correlation effects* in explaining the spectroscopic features observed [3]. Moreover, Ariando *et al*. have reported room-temperature magnetism characteristics and claimed electronic phase separation in their $LaAlO_3/SrTiO_3$ samples—suggesting that electron correlations may be very important [4].

The experimental techniques and the fabrication and synthesis tools available today enable more detailed exploration of complex oxides, particularly in thin-film heterostructures. The goals of controlling complexity and wielding electron correlations to tune functionalities in condensed matter systems certainly pose great challenges, but at the same time hold great promise.

* Correlation effects are accounted for by Breitschaft *et al*. using a local density approximation + *U* calculation [4].

Appendix

A.1. Heteroepitaxial strain in thin films 115
A.1.1. Strain and stress as thermodynamic conjugate pairs 115
A.1.2. Physical interpretation of the strain and stress tensors 116
A.1.3. Matrix representation 119
A.1.4. Heteroepitaxial lattice distortions 120
A.2. Disorder and localization in two-dimensional systems 122
A.2.1. Coherent backscattering in electronic systems 123
A.2.2. The competition of disorder and carrier density in localization . . . 124
A.2.3. Quantum correction to conductance 125
A.2.4. Effect of applied magnetic fields on weak (anti)localization 126
A.3. Ferromagnetic coupling through superexchange interaction 128

§ A.1 Heteroepitaxial strain in thin films

The properties of many complex oxides are sensitive to the materials' lattice degree of freedom. Through heteroepitaxy, it is possible to impose the in-plane structure of the substrate onto the thin film, and consequently, the film's lattice state is different from that of the bulk. We are interested in how heteroepitaxial strain can not only modify materials properties, but also alter the ground state of the thin-film material as compared to the bulk.

A.1.1 Strain and stress as thermodynamic conjugate pairs

The ground state of the system is determined by a minimization of energy. The internal energy (E) governs the thermodynamics of a closed system—a system that does not interact with its surroundings. A change in energy (dE) can arise from incremental heat flowing into (δq) or work done on (δw) a system. Heat is given by $\delta q = T dS$, where T is temperature and S is entropy. For the purposes of this section, we will consider only mechanical work $\delta w = V_0 \sigma d\varepsilon - P dV$, where σ is stress, ε is strain, P is pressure, V is volume, and V_0 is the reference volume at atmospheric pressure (1 atm = 101.3 kPa).[*] Hence, the change in energy of the system is given by

$$dE = \delta q + \delta w = TdS + V_0 \sigma d\varepsilon - PdV$$

The natural variables of E are S, ε, and V; T, σ, P are their conjugate forces, respectively. However, a materials system of interest is rarely ever closed; most systems interact with their environments. For example, the temperature of a room sets the temperature of objects inside the room. Systems of interest in materials science often have diathermal and deformable walls; they allow T, σ, and P to be imposed onto the system. Such a system is governed by its free energy function G' that has T, σ, and P as its natural variables. An incremental change in free energy (dG') can be determined by the appropriate Legendre transformation and is given by[†]

$$dG' = -SdT - V_0 \varepsilon d\sigma + V_0 dP \qquad \text{(Eqn. A.1)}$$

The conditions for stability are $dG' = 0$ and $d^2G' > 0$.[‡] We all are familiar with the ice-water transition, which can be traversed by changing the temperature. In Eqn. A.1, σ has

[*] P will be set to the atmospheric pressure, 1 atm = 101.3 kPa. We can account for added pressure in σ. This treatment is useful for the consideration of elastic solids.

[†] G' resembles the Gibbs free energy (G), but in standard texts, G typically does not include σ. Eqn A.1 also explicitly restricts P to atmospheric pressure.

[‡] Stability here refers to *local stability*. True equilibrium refers to *global stability*.

an analogous role to T, and hence σ should also be treated as a tuning parameter that can potentially induce the transition from one material phase to another. Fig. A.1 shows that as a function of T, the equilibrium phase is the one with lower G'; this is likewise the case when one replaces T with σ. In thin films, stress can be imposed by the substrate and induce a phase transition on the film.

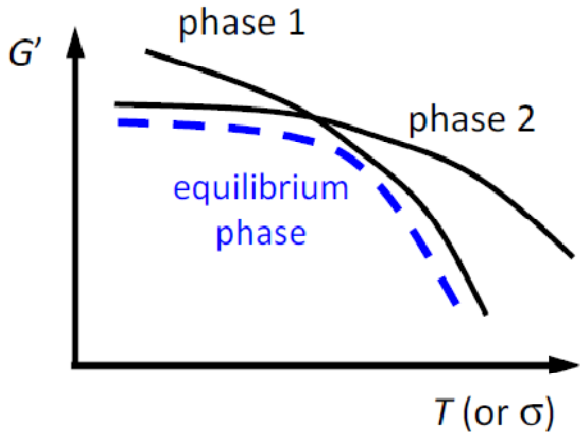

Figure A.1. Schematic of the change in free energy as a function of temperature or stress.

A.1.2 Physical interpretation of the strain and stress tensors

Whereas S and T are scalar quantities, $\boldsymbol{\varepsilon}$ and $\boldsymbol{\sigma}$ are second-order tensors. The physical interpretation of strain can be achieved by first considering the definition of a displacement tensor element e_{ij}:

$$e_{ij} = \frac{u_i}{l_j}$$

for $i, j = 1, 2, 3$, where u_i is the displacement along the i direction, and l_j is the reference length along the j direction. Typically, crystal lattice parameters will be taken as reference lengths. The physical deformation associated with e_{22} and e_{33} is illustrated in Fig. A.2a, and that of e_{23} and e_{32} in Fig. A.2b. We observe in Fig. A.2b that for small displacements, e_{23} and e_{32} can be interpreted as rotation angles θ_{23} and θ_{32} about the x_1 axis. See Ref. [1] for detailed discussions. Since rigid-body rotations, which do not change the shape of the material, cannot possibly change the energy of the system, the strain tensor $\boldsymbol{\varepsilon}$ does not include the portion of $\boldsymbol{e}$ that corresponds to shape-preserving rotations, as illustrated in Fig. A.3. The strain tensor $\boldsymbol{\varepsilon}$ is therefore defined as the symmetric part of $\boldsymbol{e}$:

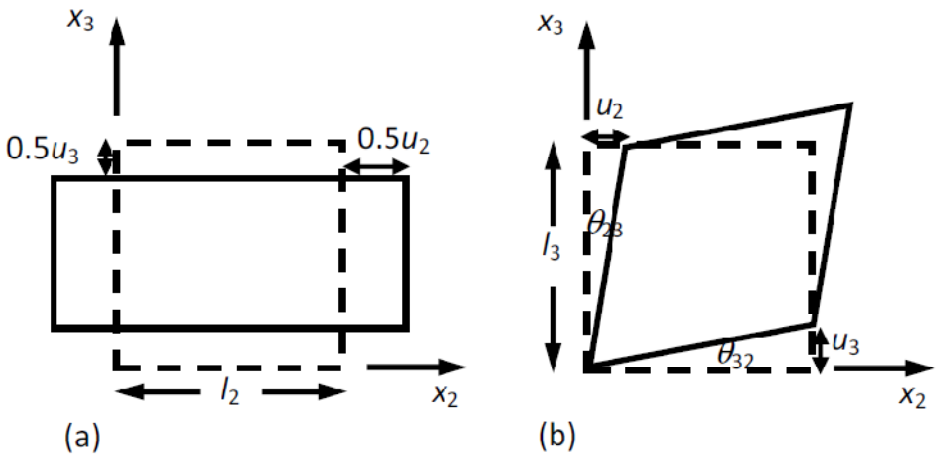

Figure A.2. Physical interpretations of (a) e_{22}, e_{33}, (b) e_{23}, and e_{32}. The dotted lines show the initial shapes and the solid lines show the final distorted shapes.

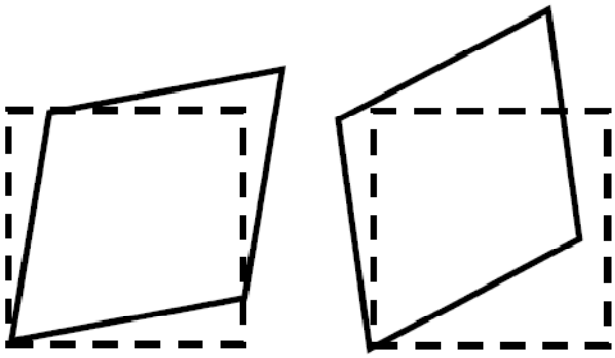

Figure A.3. Initial shape is shown with dashed lines. The final configurations (solid lines) of the left and right schematics have the same shape, and thus the same energy.

$$\varepsilon_{ij} \equiv \frac{1}{2}\left(e_{ij} + e_{ji}\right) \; : \; \begin{bmatrix} \varepsilon_{11} & \varepsilon_{12} & \varepsilon_{13} \\ \varepsilon_{12} & \varepsilon_{22} & \varepsilon_{23} \\ \varepsilon_{13} & \varepsilon_{23} & \varepsilon_{33} \end{bmatrix} \equiv \begin{bmatrix} e_{11} & \frac{1}{2}(e_{12}+e_{21}) & \frac{1}{2}(e_{13}+e_{31}) \\ \frac{1}{2}(e_{12}+e_{21}) & e_{22} & \frac{1}{2}(e_{23}+e_{32}) \\ \frac{1}{2}(e_{13}+e_{31}) & \frac{1}{2}(e_{23}+e_{32}) & e_{33} \end{bmatrix}$$

Note that the indices of the elements $\varepsilon_{ij} = \varepsilon_{ji}$ explicitly show that $\boldsymbol{\varepsilon}$ is a symmetric tensor. To show the physical meaning of each matrix component, the strain tensor is often decomposed into tensors representing the volume dilation, orthorhombic distortion, and pure shear strain [2]:

$$\boldsymbol{\varepsilon} = \begin{bmatrix} \varepsilon_{11} & \varepsilon_{12} & \varepsilon_{13} \\ \varepsilon_{12} & \varepsilon_{22} & \varepsilon_{23} \\ \varepsilon_{13} & \varepsilon_{23} & \varepsilon_{33} \end{bmatrix}$$
$$= \frac{1}{3}\begin{bmatrix} \varepsilon_{11}+\varepsilon_{22}+\varepsilon_{33} & 0 & 0 \\ 0 & \varepsilon_{11}+\varepsilon_{22}+\varepsilon_{33} & 0 \\ 0 & 0 & \varepsilon_{11}+\varepsilon_{22}+\varepsilon_{33} \end{bmatrix}$$
$$+ \frac{1}{3}\begin{bmatrix} 2\varepsilon_{11}-\varepsilon_{22}-\varepsilon_{33} & 0 & 0 \\ 0 & 2\varepsilon_{22}-\varepsilon_{11}-\varepsilon_{22} & 0 \\ 0 & 0 & 2\varepsilon_{33}-\varepsilon_{11}-\varepsilon_{22} \end{bmatrix}$$
$$+ \begin{bmatrix} 0 & \varepsilon_{12} & \varepsilon_{13} \\ \varepsilon_{12} & 0 & \varepsilon_{23} \\ \varepsilon_{13} & \varepsilon_{23} & 0 \end{bmatrix}$$

(Eqn. A.2)

Let us now turn to the stress tensor. Stress is a force per unit area; because both the force and the unit area element[§] can be in any direction in three-dimensional space, stress is likewise a second-order tensor. For crystals, the area element is taken on a relevant atomic plane. We will define the stress element σ_{ij} as the force in the *i* direction applied on a plane in the *j* direction, as illustrated in Fig. A.4a. As a translation of a material does not change its energy, there is an equal and opposite forces on opposite planes, as drawn along the x_1 axis projection in Fig. A.4b. Forces that cause translation are not included in the stress tensor. Also, because the strain tensor does not include shape-preserving rotations, the stress tensor for static equilibrium is likewise symmetric ($\sigma_{ij} = \sigma_{ji}$).

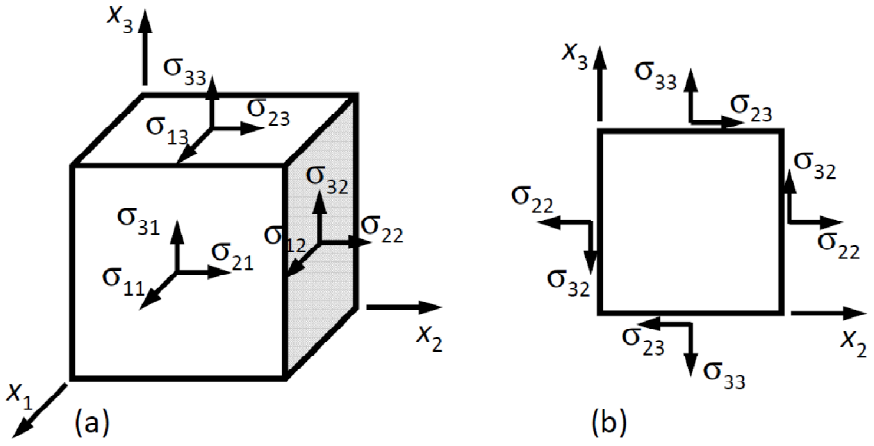

Figure A.4. Schematics (a) defining each σ_{ij} element and (b) showing the projection along the x_1 axis.

[§] The direction of a unit area vector is defined to be that of its normal vector.

For a particular stress field applied to a material, we need to know how much it will strain. The property of concern is elasticity, particularly the compliance ***s***, which is defined as the differential strain per differential stress. Since both strain and stress are second-order tensors, ***s*** is a property tensor with a rank of 4 and is given by

$$s_{ijkl} = \frac{\partial \varepsilon_{ij}}{\partial \sigma_{kl}} = -\frac{1}{V_0}\frac{\partial^2 G'}{\partial \sigma_{kl}\partial \sigma_{ij}}$$

A.1.3 Matrix representation

When the strain is small, we can take the linear approximation

$$\varepsilon_{ij} = s_{ijkl}\sigma_{kl}$$

(Eqn. A.3)

Although Eqn. A.3 accurately expresses the tensor aspects of elasticity, the index dyad notation is often cumbersome for calculations. Using the following recipe, calculations of elastic deformation can be performed by matrix multiplication. The strain and stress tensors are rewritten as vectors:

$$\begin{bmatrix} \varepsilon_{11} & \varepsilon_{12} & \varepsilon_{13} \\ \varepsilon_{12} & \varepsilon_{22} & \varepsilon_{23} \\ \varepsilon_{13} & \varepsilon_{23} & \varepsilon_{33} \end{bmatrix} = \begin{bmatrix} \varepsilon_1 & \frac{1}{2}\varepsilon_6 & \frac{1}{2}\varepsilon_5 \\ \frac{1}{2}\varepsilon_6 & \varepsilon_2 & \frac{1}{2}\varepsilon_4 \\ \frac{1}{2}\varepsilon_5 & \frac{1}{2}\varepsilon_4 & \varepsilon_3 \end{bmatrix} \rightarrow \begin{bmatrix} \varepsilon_1 \\ \varepsilon_2 \\ \varepsilon_3 \\ \varepsilon_4 \\ \varepsilon_5 \\ \varepsilon_6 \end{bmatrix}$$

$$\begin{bmatrix} \sigma_{11} & \sigma_{12} & \sigma_{13} \\ \sigma_{12} & \sigma_{22} & \sigma_{23} \\ \sigma_{13} & \sigma_{23} & \sigma_{33} \end{bmatrix} = \begin{bmatrix} \sigma_1 & \sigma_6 & \sigma_5 \\ \sigma_6 & \sigma_2 & \sigma_4 \\ \sigma_5 & \sigma_4 & \sigma_3 \end{bmatrix} \rightarrow \begin{bmatrix} \sigma_1 \\ \sigma_2 \\ \sigma_3 \\ \sigma_4 \\ \sigma_5 \\ \sigma_6 \end{bmatrix}$$

The compliance tensor is transformed using the following rules (m, n = 1, 2,…, 6 are as defined above):

$s_{ijkl} = s_{mn}$ when m and n are 1, 2, or 3
$2s_{ijkl} = s_{mn}$ when either m or n (not both) is 4, 5, or 6
$4s_{ijkl} = s_{mn}$ when both m and n are 4, 5, or 6

The reader is referred to Ref. [1] for a detailed discussion on the reindexing of subscripts of the compliance tensor. Using the matrix notation, Eqn. A.3 can be rewritten as

$$\varepsilon_i = s_{ij}\sigma_j$$

(Eqn. A.4)

Taking into account all of the symmetry elements, we can write Eqn. A.4 for a cubic crystal as

$$\begin{bmatrix}\varepsilon_1\\ \varepsilon_2\\ \varepsilon_3\\ \varepsilon_4\\ \varepsilon_5\\ \varepsilon_6\end{bmatrix} = \begin{bmatrix}s_{11} & s_{12} & s_{12} & 0 & 0 & 0\\ s_{12} & s_{11} & s_{12} & 0 & 0 & 0\\ s_{12} & s_{12} & s_{11} & 0 & 0 & 0\\ 0 & 0 & 0 & s_{44} & 0 & 0\\ 0 & 0 & 0 & 0 & s_{44} & 0\\ 0 & 0 & 0 & 0 & 0 & s_{44}\end{bmatrix}\begin{bmatrix}\sigma_1\\ \sigma_2\\ \sigma_3\\ \sigma_4\\ \sigma_5\\ \sigma_6\end{bmatrix}$$

(Eqn. A.5)

Though Eqn. A.4 hides some of the tensor aspects associated with elasticity, it is useful for calculations. In fact, elastic constants are generally measured and tabulated as s_{ij} rather than s_{ijkl}.

It is often convenient to express the stress field tensor in different coordinate systems. A change-of-coordinates transformation allows for the mapping of one coordinate system to another. The transformation is given by

$$\sigma_{ij} = \alpha_{im}\alpha_{jn}\sigma'_{mn}$$

(Eqn. A.6)

which transforms the stress tensor from the primed to unprimed coordinate system and $\alpha_{ij} = \cos\beta_{ij}$ (direction cosines), where β_{ij} is the angle between the x_i and x_j' axes. The strain tensor can be transformed similarly. Though we could have applied coordinate transformation to the compliance tensor, it is not common. Because compliance is a property tensor of the material, we often stick with a specific set of crystalline axes as the basis rather than an arbitrary one.

A.1.4 Heteroepitaxial lattice distortions

We will now consider the case of (001) heteroepitaxial strain on cubic crystals. x_1, x_2, and x_3 are [100], [010], and [001], respectively. Through heteroepitaxy, biaxial in-plane stress is applied onto the thin film and is given by:

$$\boldsymbol{\sigma} = \begin{bmatrix}\sigma_0 & 0 & 0\\ 0 & \sigma_0 & 0\\ 0 & 0 & 0\end{bmatrix}$$

Using Eqn. A.5, we can see that the resulting strain tensor is

$$\boldsymbol{\varepsilon}^{(001)} = \begin{bmatrix}\varepsilon_{11} & 0 & 0\\ 0 & \varepsilon_{11} & 0\\ 0 & 0 & \varepsilon_{33}\end{bmatrix}$$

(Eqn. A.7)

where

$$\varepsilon_{11} = (s_{11} + s_{12})\sigma_0, \qquad \varepsilon_{33} = 2s_{12}\sigma_0$$

A priori we would not know the magnitude of the stress applied, and to an extent, we do not care about that value in itself. We are primarily interested in the structure and symmetry of the resulting strain tensor. The most important aspect is we see that upon application of only σ_{11} and σ_{22}, a distortion along an orthogonal direction ε_{33} results as well—referred to as the Poisson effect. However, elasticity for a cubic crystal is anisotropic, and the "Poisson ratio" is direction-dependent. Furthermore, in comparison with Eqn. A.2, we see that (001) heteroepitaxy brings about volume dilation and a tetragonal distortion.

We now move to the case of (110) heteroepitaxy. The stress applied in the (110) plane can be decomposed to principal stresses long the [1-10] and [001] directions. Let us define a primed coordinate system, where x_1' = [1-10], x_2' = [110], and x_3' = [001] and an unprimed coordination system, where x_1 = [100], x_2 = [010], and x_3' = [001]. Here, the unprimed coordinate system is reserved to have basis lattice vectors as the basis vectors. Then the direction cosine values are as follow:

$$\alpha_{11} = \frac{1}{\sqrt{2}}, \alpha_{12} = \frac{1}{\sqrt{2}}, \alpha_{13} = 0, \alpha_{21} = \frac{-1}{\sqrt{2}}, \alpha_{22} = \frac{1}{\sqrt{2}}, \alpha_{23} = 0, \alpha_{31} = 0, \alpha_{32} = 0, \alpha_{33} = 1$$

The stress tensor in the primed coordinate system is

$$\boldsymbol{\sigma}' = \begin{bmatrix} \sigma_a & 0 & 0 \\ 0 & 0 & 0 \\ 0 & 0 & \sigma_b \end{bmatrix}$$

According to the second-order tensor transformation formula of Eqn. A.6, the stress components in the unprimed coordinate system are

$$\sigma_{11} = \alpha_{11}\alpha_{11}\sigma_{11}' = \frac{1}{2}\sigma_a$$

$$\sigma_{22} = \alpha_{21}\alpha_{21}\sigma_{11}' = \frac{1}{2}\sigma_a$$

$$\sigma_{33} = \alpha_{33}\alpha_{33}\sigma_{33}' = \sigma_b$$

$$\sigma_{12} = \alpha_{11}\alpha_{21}\sigma_{11}' = -\frac{1}{2}\sigma_a$$

The other stress components are zero. With Eqn. A.5, it can be shown that the strain tensor in this case has the form:

$$\boldsymbol{\varepsilon}^{(110)} = \begin{bmatrix} \varepsilon_{11} & \varepsilon_{12} & 0 \\ \varepsilon_{12} & \varepsilon_{11} & 0 \\ 0 & 0 & \varepsilon_{33} \end{bmatrix}$$

(Eqn. A.8)

where

$$\varepsilon_{11} = \frac{1}{2}s_{11}\sigma_a + s_{12}\left(\frac{1}{2}\sigma_a + \sigma_b\right), \qquad \varepsilon_{33} = \frac{1}{2}s_{11}\sigma_b + s_{12}\sigma_a, \qquad \varepsilon_{12} = -\frac{1}{4}s_{44}\sigma_a$$

Therefore, it can be seen that coherent (110) heteroepitaxy brings about volume dilation, tetragonal distortion, and a shear component. This situation represents a monoclinic distortion to a cubic reference.

Lastly, we can consider the case of (111) heteroepitaxy. The stress applied in the (111) plane can be decomposed to principal stresses long the [-1-12] and [1-10] directions. Let us define a primed coordinate system, where x_1' = [-1-12], x_2' = [1-10], and x_3' = [111] and an unprimed coordination system, where x_1 = [100], x_2 = [010], and x_3' = [001]. We can define the stress tensor in the primed coordinate system as

$$\boldsymbol{\sigma}' = \begin{bmatrix} \sigma_a & 0 & 0 \\ 0 & \sigma_b & 0 \\ 0 & 0 & 0 \end{bmatrix}$$

Because elasticity is isotropic on the (111) plane of a cubic crystal, $\sigma_a = \sigma_b$. As according to the aforementioned procedure, we find that the stress tensor in the unprimed coordinate system is

$$\boldsymbol{\sigma} = \begin{bmatrix} \frac{2}{3}\sigma_a & -\frac{1}{3}\sigma_a & -\frac{1}{3}\sigma_a \\ -\frac{1}{3}\sigma_a & \frac{2}{3}\sigma_a & -\frac{1}{3}\sigma_a \\ -\frac{1}{3}\sigma_a & -\frac{1}{3}\sigma_a & \frac{2}{3}\sigma_a \end{bmatrix}$$

and the strain tensor has the form:

$$\boldsymbol{\varepsilon}^{(111)} = \begin{bmatrix} \varepsilon_{11} & \varepsilon_{12} & \varepsilon_{12} \\ \varepsilon_{12} & \varepsilon_{11} & \varepsilon_{12} \\ \varepsilon_{12} & \varepsilon_{12} & \varepsilon_{11} \end{bmatrix} \qquad \text{(Eqn. A.9)}$$

where

$$\varepsilon_{11} = \frac{1}{3}(2s_{11} + 4s_{12})\sigma_a, \qquad \varepsilon_{12} = -\frac{1}{6}s_{44}\sigma_a$$

Therefore, it can be seen that (111) heteroepitaxy brings about volume dilation and shear, but no tetragonal distortion. This situation represents a rhombohedral distortion.

The structure and symmetry of the strain tensors of Eqns. A.7-A.9 tell us coherent thin-film heteroepitaxy on substrates of the same material but of different orientations can result in different strain components.

§ A.2 Disorder and localization in two-dimensional systems

Much of the experimental work in this dissertation is on electrical transport. At low temperatures, coherence of electron waves has physically measurable significance. In particular for low-dimensional disordered systems, electron coherence can easily lead to localization effects, the topic of this section.

A.2.1 Coherent backscattering in electronic systems

Wave coherence, as manifested in electromagnetic radiation and sound, is ubiquitous in nature. The superposition of waves implies the addition of their amplitudes. Because of wave-particle duality, electrons in solids can also exhibit wave interference. The observation of electron coherence relies on preservation of phase information: dephasing mechanisms destroy coherence. The phase of a traveling electron wave is $2\pi Et/h$, where E is its energy and t is the time traveled. Changes in an electron's energy therefore lead to incoherence. Any temperature-activated excitations, such as phonons, can scatter and hence alter the energy of moving electrons; thus, electron wave coherence in solids can be realized only at cryogenic temperatures.

Let us consider an arbitrary trajectory of an electron traveling from point P to P′, as shown in Fig. A.5a. As illustrated in Fig. A.5b, the trajectory is composed of connecting paths separated by elastic scattering events, which change the wave's momentum but not its energy. The average length of each segment of the trajectory is one carrier mean free path. Elastic scattering is dominant at low temperatures and allows for the preservation of electron phase.

We now will explore the consequences of wave coherence of an electron traveling from point P to P'. The electron can take many possible trajectories, each of which is associated with an amplitude, labeled A_1, …, A_i, …, A_j, … (Fig. A.6a). The probability density of a coherent superposition is given by

$$\sum_i {A_i}^2 + \sum_{i,j} A_i {A_j}^*$$

The first term represents the semiclassical result, i.e. addition of the intensity of each trajectory, and the second term arises from coherence. When points P and P′ are spatially separated, the lengths of the various trajectories differ, leading to phase differences. Consequently, in this scenario the second term averages to zero. On the other hand, in the special case in which points P and P′ coincide, for every trajectory there is a corresponding time-reversed one, shown in Fig. A.6b, which has the same path length and phase. The amplitudes of the forward and time-reversed waves are equal, $|A_1| = |A_2| = A$. Here, the intensity doubles from the semiclassical result of $2A^2$ to what is often called the quantum mechanical result of $4A^2$ by taking into account the second term representing coherence. By this argument, we can deduce that coherent electron interference ultimately results in the two-fold enhancement of backscattering events, in which the electron returns to the same location—known as coherent backscattering. Compared to the semiclassical result in which the electrons are treated as particles, they have an increased probability of being localized at a position.

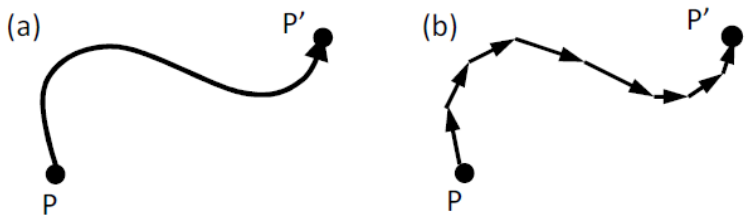

Figure A.5. (a) Schematic of an electron trajectory from point P to P′, (b) showing the elastic scattering processes that occur along such a trajectory. On average, the electron travels one mean free path before it scatters and goes in a different direction.

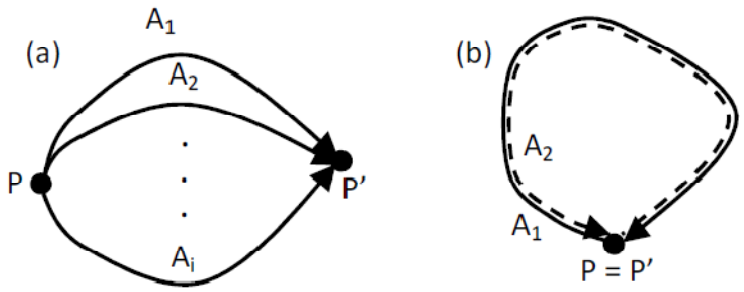

Figure A.6. (a) Schematic of different trajectories from point P to P′, and each trajectory corresponds to an amplitude A_i. (b) In the case when P and P′ coincide, the amplitude of one trajectory can be labeled as A_1 and that of the reversed trajectory as A_2. $|A_1| = |A_2| = A$.

A.2.2 The competition of disorder and carrier density in localization

Coherent backscattering is enabled by successive elastic scattering events. We categorize any elastic scattering center as disorder, which can also be thought of as a degree of randomness in electronic potentials embedded in a lattice. Static variations in the potential landscape, or disorder, compared to a completely periodic one in a perfect crystal perturb the Bloch-like behavior of carriers, thereby increasing the likelihood of localization. In addition to disorder, carrier density is another important parameter that affects carrier itineracy or localization. When an electronic system condenses to form a Fermi gas, carrier electrons attain kinetic energy and delocalize. Systems with higher carrier concentrations have more kinetic energy because of a greater amount of electronic overlap. The competition between disorder and carrier concentration governs metal-insulator transitions. If localization is brought about strictly by increased disorder, it is known as an Anderson transition [3], whereas if it is brought about by reduced carrier density, it is known as a Mott transition [4].

The problem of localization for non-interacting, spinless electron systems was explored using scaling analysis [5]. The readers are referred to Abrahams *et al.*'s original paper, but details of the scaling approach will be not discussed here. The most surprising result found is that a two-dimensional electronic system can never be truly metallic, i.e. it can never possess finite conductance at 0 K, as long as some degree of disorder is present. Abrahams *et al.*'s analysis highlights both the importance of and susceptibility to localization in low-dimensional materials. In this work, strong localization will not be considered; rather, weak localization is relevant within the temperature regime of the performed electrical transport measurements, and it is treated as a perturbation to metallic conductance (Chapter 6).

A.2.3 Quantum correction to conductance

In systems that follow Mattheissen's rule, at low temperatures in which thermally activated scattering mechanisms are suppressed, the resistivity is expected to remain constant due to scattering with defects and boundaries of the samples. However, such an approximation ignores the effects of the interference of electron waves. The approach is to add a correction term to the Drude conductivity to account for coherent backscattering.

As shown in Section A.2.1, electron coherence causes a two-fold increase in backscattering probability, resulting in reduced conductance and weak localization. Though coherent backscattering is a manifestation of the wave-like nature of electrons, we can model the effect as a classical particle diffusion problem by utilizing the previously established quantum mechanical contribution. The condition for weak localization is that the carrier dephasing time τ_φ is much greater than the elastic scattering time τ_e, which is roughly equal to the net scattering time τ; an electron can undergo many elastic scattering events to allow for returning to the original location before the lost of phase information.

After time t for random-walk diffusion, a classical particle can be found at a distance r from the origin with a probability of

$$\Pi(r,t) = \frac{e^{-r^2/4Dt}}{(4\pi Dt)^{d/2}} \tag{A.10}$$

where D is the electron diffusivity and d is the dimensionality of the system. We are particularly interested in the return probability. We know from the discussion on coherent backscattering that the return probability at a given time, i.e. $\Pi(r=0,t)$, is increased two-fold because of electron interference; therefore, as shown in Fig. A.7, we can envisage that there is a two-fold enhanced peak in electron probability at the origin that has to be compensated by reduced electron probability density farther away. This

scenario exemplifies the decrease in effective electron diffusivity, or increase in resistivity, as compared to the Drude value. At exceedingly low temperatures, it takes a long time for a temperature-induced inelastic scattering event that dephases carriers to occur; enhanced coherent backscattering therefore can affect electrons that travel even longer return paths. Therefore, conductance is reduced at lower temperatures. It can be shown that the two-dimensional conductivity (sheet conductance) has the following temperature dependence owing to enhanced backscattering [6]

$$\sigma = \sigma_{Drude} + \Delta\sigma = \sigma_{Drude} - \frac{pe^2}{\pi h} ln\left(\frac{T_0}{T}\right)$$

where T is the temperature, p is defined as $\tau_{in} \propto T^{-p}$, and T_0 ($>T$) is a constant temperature. At $T = T_0$, the conductance is just the Drude expression. At the temperature range of consideration for weak localization, the Drude conductance is approximately constant.

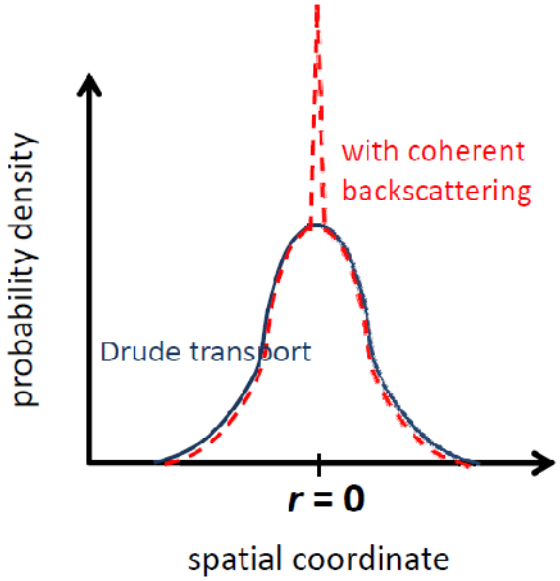

Figure A.7. Schematic of electron density profile at time t of an electron that started at $r = 0$ at time $t = 0$. The profile corresponding to just Drude transport is compared to that of after taking coherent backscattering into account.

A.2.4 Effect of applied magnetic fields on weak (anti)localization

When an electron wave travels from position r_0 to r_1 in the presence of a magnetic field, its wavefunction changes from $\psi(r_0)$ to

$$\psi(r_1) = \psi(r_0) exp\left(\frac{i2\pi}{h} \oint q\vec{A} \cdot d\vec{r}\right)$$

where **A** is the vector potential. A magnetic field *B* alters the phase of electron waves, and reduces the τ_φ (inversely proportional to *B*) for a given temperature. As electron wave coherence becomes more prominent at lower temperatures, the negative magnetoresistance should also become greater in magnitude, as shown by Bergmann in Mg thin films [7].

In the previous discussion, we consider the self-interference of only a single electron without taking into account its spin. We now will incorporate the case of a pair of electrons with spins into the discussion. The two electrons can form either a spin antisymmetric, spatially symmetric singlet or a spin symmetric, spatially antisymmetric triplet. The spin-orbit scattering time τ_{so} is defined to be the average time interval between successive carrier spin-flip processes. When spin-orbit coupling is weak, the electrons act as individual, independent particles. In the presence of stronger spin-orbit coupling, there is an increased probability that a singlet scatters into a triplet state and vice versa. Because of the singlet and triplet states are spatially antisymmetric to each other, spin flipping causes the destruction of backscattering events [4,8]. Interference in this case results in reduced electron return probability compared to the semiclassical Drude result; hence, strong spin-orbit interaction ($\tau_\varphi \gg \tau_{so} > \tau$) leads to what is known as antilocalization. If the return paths, as shown in Fig. A.6b, are long enough such that there is a high probability of spin-orbit scattering, the return probability is negated due to destructive electron interference, i.e. antilocalization. Only the shorter return paths survive to interfere constructively without a spin-orbit scattering event, and continue to contribute to weak localization. Therefore, if spin-orbit scattering is strong enough, there can be positive magnetoresistance.

In low fields (magnetic time $\tau_B = \hbar/eDB > \tau_{so}$), the magnetic field, as does inelastic scattering, limits the length of phase-preserving return paths in Fig. A.6b that can contribute to weak antilocalization; hence, the effects of weak antilocalization are suppressed, and positive magnetoresistance results. In higher fields, when $\tau < \tau_B < \tau_{so}$, spin-flip events become irrelevant, because electrons dephase before they can undergo a spin-orbit scattering event. Further increases in magnetic field result in the disruption of the constructive interference of the shorter return paths; hence the effects of weak localization are suppressed, and negative magnetoresistance results. All in all, the magnetoresistance of systems with strong spin-orbit interaction has positively and negatively sloped segments; this situation is schematically shown in Fig. A.8. The boundaries as shown are not sharp.

Bergmann conducted an elegant experiment in which he varied the fractional monolayer coverage of Au atoms, which are a source of strong spin-orbit interaction, deposited onto Mg thin films [9]. Indeed, more pronounced antilocalization effects were observed in Mg films with greater amount of Au coverage.

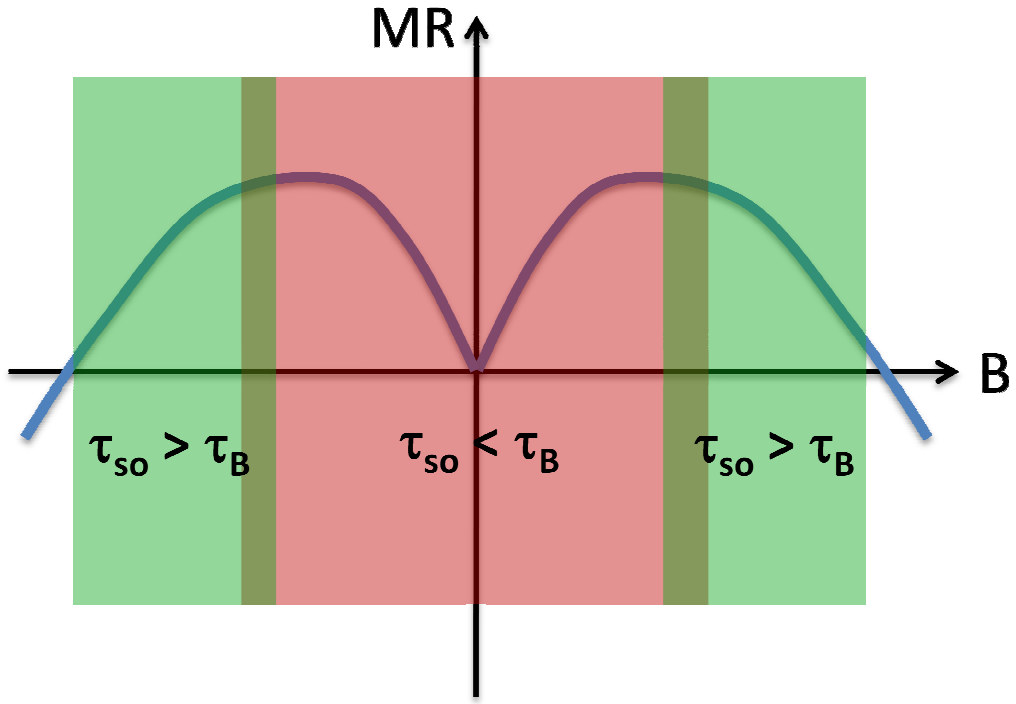

Figure A.8. Schematic of a magnetoresistance (MR) curve of a sample with strong spin-orbit scattering; τ_{so} is the spin-orbit scattering time, and τ_B is the magnetic time.

§ A.3. Ferromagnetic coupling through superexchange interaction

The following model calculation follows the same approach as found in Ref. [10] for superexchange between two half-filled, single-orbital sites. The Hubbard interaction Hamiltonian can be generalized for the case of a multiorbital system:

$$H\hat{} = -\sum_{i,p,j,p',\sigma} t_{ipjp'}\left(c^{\dagger}_{ip\sigma}c_{jp'\sigma} + c^{\dagger}_{jp'\sigma}c_{ip\sigma}\right) + \sum_{i,p} U_{ip}n_{ip\uparrow}n_{ip\downarrow} + \sum_{i,p,p'\neq p} J_i^H\left(n_{ip\uparrow}n_{ip'\downarrow} + n_{ip\downarrow}n_{ip'\uparrow}\right) + \sum_{i,p,p'\neq p,\sigma,\sigma'} \upsilon_i\, n_{ip\sigma}n_{ip'\sigma'}$$

where i and j are indices of the sites; p and p' are indices of orbitals within a particular site; n, c^{+}, and c are the electron number, creation, and annihilation operators; t is the site-to-site transfer integral; U is the on-site potential energy penalty for two electrons to occupy the same orbital; J^H is the energy penalty for not maximizing the total spin of a site; and υ is the energy penalty associated with disobeying charge ordering that acts to localize electrons within each site for a multiorbital system. Here, we consider a two-site

(1 and 2) system, and each site has two orbitals (*a* and *b*). Furthermore, the system has (on average) one electron per site. Suppose that $t_{1a2a} = t$ and all of the other transfer integrals are 0. Furthermore, we will impose that orbital *b* of site 2 is always occupied. As discussed in Section 5.2, such conditions are not atypical for transition-metal perovskite oxides.

For this example, let us assume that the double occupancy of the same orbital is forbidden and not included in the basis set of multielectron states. We can write down a multielectron state such as $|\uparrow 0,0 \uparrow>$, which refers to the state with a spin-up electron in orbital *a* of site 1 and a spin-down electron in orbital *b* of site 2; orbital *b* of site 1 and orbital *a* of site 2 are empty. $|00,\uparrow\downarrow>$ refers to the state with a spin-up electron in orbital *a* of site 2 and a spin-down electron in orbital *b* of site 2; the orbitals of site 1 are empty. Using this convention of multielectron states, we can consider a basis set of electronic states as follow:

$|\uparrow 0,0 \uparrow>$ $|\downarrow 0,0 \downarrow>$ $|\uparrow 0,0 \downarrow>$ $|\downarrow 0,0 \uparrow>$ $|00,\uparrow\uparrow>$ $|00,\downarrow\downarrow>$ $|00,\uparrow\downarrow>$ $|00,\downarrow\uparrow>$

The choice of the basis set is consistent with there always being one electron in orbital *b* of site 2. We have three relevant energy terms: the kinetic energy of hopping *t* of one electron from orbital *a* of site 1 to that of site 2, Hund energy J^H for maximizing spin, and a charge ordering term υ that disfavors electron occupation of both orbitals *a* and *b* of the same site. The on-site (on-orbital) energy term *U* does enter into the interaction Hamiltonian matrix in this particular case because of the exclusion of any multielectron state with double occupancy of a single orbital from our basis set. The interaction Hamiltonian H^ matrix can be written as:

$$\begin{bmatrix} 0 & 0 & 0 & 0 & -t & 0 & 0 & 0 \\ 0 & 0 & 0 & 0 & 0 & -t & 0 & 0 \\ 0 & 0 & 0 & 0 & 0 & 0 & -t & 0 \\ 0 & 0 & 0 & 0 & 0 & 0 & 0 & -t \\ -t & 0 & 0 & 0 & \upsilon & 0 & 0 & 0 \\ 0 & -t & 0 & 0 & 0 & \upsilon & 0 & 0 \\ 0 & 0 & -t & 0 & 0 & 0 & \upsilon + J^H & 0 \\ 0 & 0 & 0 & -t & 0 & 0 & 0 & \upsilon + J^H \end{bmatrix}$$

The eigenvalues are

$$E_{1,2} = \frac{1}{2}\left[\upsilon \pm \upsilon\sqrt{1 + \frac{4t^2}{\upsilon^2}}\right]$$

$$E_{3,4} = \frac{1}{2}\left[(\upsilon + J^H) \pm (\upsilon + J^H)\sqrt{1 + \frac{4t^2}{(\upsilon + J^H)^2}}\right]$$

Each eigenenergy state has a degeneracy of 2. We will consider E_2 and E_4. In the case of $t \ll \upsilon$ and J^H, those eigenenergies can be approximated as

$$E_2 \approx -\frac{t^2}{\upsilon}$$

$$E_4 \approx -\frac{t^2}{J^H + \upsilon}$$

The eigenfunctions associated with E_2 can then be approximated as

$$\Psi_{2A} \propto |\uparrow 0,0\uparrow> + \frac{t}{\upsilon}|00,\uparrow\uparrow>$$

$$\Psi_{2B} \propto |\downarrow 0,0\downarrow> + \frac{t}{\upsilon}|00,\downarrow\downarrow>$$

representing states with ferromagnetic coupling. Because $t \ll \upsilon$, this wavefunction is consistent with the stated preference for orbital *a* of site 1 to be filled and orbital *b* of site 1 to be empty.

Likewise the eigenfunctions associated with E_4 can be approximated as

$$\Psi_{4A} \propto |\downarrow 0,0\uparrow> + \frac{t}{\upsilon + J^H}|00,\downarrow\uparrow>$$

$$\Psi_{4B} \propto |\uparrow 0,0\downarrow> + \frac{t}{\upsilon + J^H}|00,\uparrow\downarrow>$$

representing states with antiferromagnetic coupling. If we want to rewrite H^ to explicitly show the magnetic interaction such that it has the form of

$$H_{ex} = J\vec{S}_1 \cdot \vec{S}_2$$

where $\boldsymbol{S}_1$ and $\boldsymbol{S}_2$ are the total spin in sites 1 and 2, respectively, then we get

$$2J \approx E_2 - E_4 = -\frac{t^2 J^H}{\upsilon(J^H + \upsilon)}$$

Here, a negative *J* value corresponds to a ferromagnetic ground state. Therefore, we can indeed see that ferromagnetic coupling in a Mott insulator can directly result from the Hubbard Hamiltonian of the form of H^, which includes sites of more than one orbital. Conditions of charge and orbital ordering have been imposed to achieve the ferromagnetic exchange. In Section 5.2, it is further shown how such charge and orbital states can be linked to lattice distortions.

Lastly, as written Ψ_{2A}, Ψ_{2B}, Ψ_{4A}, and Ψ_{4B} are approximated for $t \ll \upsilon$ and J^H; if conversely, $t \gg \upsilon$, J^H, it can be shown that a ferromagnetic metallic or a diamagnetic metallic state becomes the ground state, depending on whether there is orbital ordering in site 2.

References

Chapter 1

[1] N. F. Mott, The basis of the electron theory of metals, with special reference to the transition metals, Proc. Phys. Soc. A **62**, 416 (1949).

[2] *Directing Matter and Energy: Five Challenges for Science and the Imagination*, Department of Energy, Basic Energy Sciences workshop report http://www.er.doe.gov/bes/reports/files/GC_rpt.pdf

[3] A. Ohtomo, D. A. Muller, J. L. Grazul, and H. Y. Hwang, Artificial charge-modulation in atomic-scale perovskite titanate superlattices, Nature **419**, 378 (2002).

[4] S. H. Strogatz, *Sync: The Emerging Science of Spontaneous Order* (Hyperion, New York, 2003).

[5] P. W. Anderson, More is different, Science **177**, 393 (1972).

[6] M. N. Baibich, J. M. Broto, A. Fert, F. Nguyen Van Dau, F. Petroff, P. Eitenne, G. Creuzet, A. Friederich, and J. Chazelas, Giant magnetoresistance of (001)Fe/(001)Cr magnetic superlattices, Phys. Rev. Lett. **61**, 2472 (1988).

[7] A.-B. Posadas, M. Lippmaa, F. J. Walker, M. Dawber, C. H. Ahn, and J.-M. Triscone, Growth and novel applications of epitaxial oxide thin films, in *Physics of Ferroelectrics: A Modern Perspective*, edited by K. Rabe, C. H. Ahn, and J.-M. Triscone. Topics Appl. Phys. **105**, 219 (2007).

[8] R. C. Neville, B. Hoeneisen, and C. A. Mead, Permittivity of strontium titanate, J. Appl. Phys. **43**, 2124 (1972).

[9] J. H. Haeni, P. Irvin, W. Chang, R. Uecker, P. Reiche, Y. L. Li, S. Choudhury, W. Tian, M. E. Hawley, B. Craigo, A. K. Tagantsev, X. Q. Pan, S. K. Streiffer, L. Q. Chen, S. W. Kirchoefer, J. Levy, and D. G. Schlom, Room-temperature ferroelectricity in strained $SrTiO_3$, Nature **430**, 758 (2004).

[10] J. H. Lee, L. Fang, E. Vlahos, X. Ke, Y. W. Jung, L. Fitting Kourkoutis, J.-W. Kim, P. J. Ryan, T. Heeg, M. Roeckerath, V. Goian, M. Bernhagen, R. Uecker, P. C. Hammel, K. M. Rabe, S. Kamba, J. Schubert, J. W. Freeland, D. A. Muller, C.

J. Fennie, P. Schiffer, V. Gopalan, E. Johnston-Halperin, and D. G. Schlom, A strong ferroelectric ferromagnet created by means of spin-lattice coupling, Nature **466**, 954 (2010).

[11] K. von Klitzing, The quantized Hall effect, Rev. Mod. Phys. **58**, 519 (1986).

[12] C. H. Ahn, A. Bhattacharya, M. Di Ventra, J. N. Eckstein, C. D. Frisbie, M. E. Gershenson, A. M. Goldman, I. H. Inoue, J. Mannhart, A. J. Millis, A. F. Morpurgo, D. Natelson, J.-M. Triscone, Electrostatic modification of novel materials, Rev. Mod. Phys. **78**, 1185 (2006).

[13] R. Scherwitzl, P. Zubko, I. G. Lezama, S. Ono, A. F. Morpurgo, G. Catalan, J.-M. Triscone, Electric-field control of the metal-insulator transition in ultrathin $NdNiO_3$ films, Adv. Mater. **22**, 5517 (2010).

[14] X. Hong, A. Posadas, and C. H. Ahn, Examining the screening limit of field effect devices via the metal-insulator transition, Appl. Phys. Lett. **86**, 142501 (2005).

[15] A. Ohtomo and H. Y. Hwang, A high-mobility electron gas at the $LaAlO_3/SrTiO_3$ heterointerface, Nature **427**, 423 (2004).

[16] H. Kroemer, Nobel lecture: Quasielectric fields and band offsets: teaching electrons new tricks, Rev. Mod. Phys. **73**, 783 (2001).

[17] E. Yablonovitch and E. O. Kane, Reduction of lasing threshold current density by the lowering of valence band effective mass, J. Lightwave Technol. **4**, 504 (1986).

Chapter 2

[1] A.-B. Posadas, M. Lippmaa, F. J. Walker, M. Dawber, C. H. Ahn, and J.-M. Triscone, Growth and novel applications of epitaxial oxide thin films, in *Physics of Ferroelectrics: A Modern Perspective*, edited by K. Rabe, C. H. Ahn, and J.-M. Triscone. Topics Appl. Phys. **105**, 219 (2007).

[2] B. D. Cullity and S. R. Stock, *Elements of X-ray Diffraction*, 3rd ed. (Prentice-Hall, Upper Saddle River, 2001).

[3] L. J. van der Pauw, A method of measuring the resistivity and Hall coefficient of a lamellae of arbitrary shape, Philips Tech. Rev. **20**, 220 (1958).

[4] M. Lundstrom, *Fundamentals of carrier transport*, 2nd ed. (Cambridge UP, Cambridge, 2000).

Chapter 3

[1] I. D. Brown, *The Chemical Bond in Inorganic Chemistry: The Bond Valence Model* (Oxford UP, Oxford, 2002).

[2] J. B. Goodenough and J.-S. Zhou, General Considerations, in *Localized to itinerant transition in perovskite oxides*, edited by J. B. Goodenough. Struct. Bond. **98**, 17 (2001).

[3] N. W. Ashcroft and N. D. Mermin, *Solid State Physics* (Brooks/Cole, Australia, 1976).

[4] M. P. Marder, *Condensed Matter Physics* (John Wiley, New York, 2000).

[5] D. Feng and G. Jin, *Introduction to Condensed Matter Physics* (World Scientific, New Jersey, 2005).

[6] P. Y. Yu and M. Cardona, *Fundamentals of Semiconductors: Physics and Materials Properties* (Springer, Berlin, 2010).

[7] N. F. Mott, The basis of the electron theory of metals, with special reference to the transition metals, Proc. Phys. Soc. A **62**, 416 (1949).

[8] J. B. Torrance, P. Lacorre, C. Asavaroengchai, and R. M. Metzger, Why are some oxides metallic, while most are insulating? Physica C **182**, 351 (1991).

[9] J. Zaanen, G. A. Zawatzky, and J. W. Allen, Band gaps and electronic structure of transition-metal compounds, Phys. Rev. Lett. **55**, 418 (1985).

[10] T. Arima and Y. Tokura, Optical study of electron structure in perovskite-type RMO_3 (*R*=La, Y; *M*=Sc, Ti, V, Cr, Mn, Fe, Co, Ni, Cu), J. Phys. Soc. Jpn. **64**, 2488 (1995).

[11] C. Zener, Interaction between the *d*-shells in the transition metals. II. Ferromagnetic compounds of manganese with perovskite structure, Phys. Rev. **82**, 403 (1951).

[12] P. W. Anderson, Antiferromagnetism. Theory of superexchange interaction, Phys. Rev. **79**, 350 (1950).

[13] J. B. Goodenough, Theory of the role of covalence in the perovskite-type manganites [La,*M*(II)]MnO_3, Phys. Rev. **100**, 564 (1955).

[14] J. B. Goodenough, An interpretation of the magnetic properties of the perovskite-type mixed crystals $La_{1-x}Sr_xCoO_{3-\lambda}$, J. Phys. Chem. Solids **6**, 287 (1958).

[15] J. Kanamori, Superexchange interaction and symmetry properties of electron orbitals, J. Phys. Chem. Solids **10**, 87 (1959).

[16] J. B. Goodenough, *Magnetism and the Chemical Bond* (Interscience, New York, 1963).

[17] J. Stöhr and H. C. Siegmann, *Magnetism: From Fundamentals to Nanoscale Dynamics* (Springer, Berlin, 2006).

Chapter 4

[1] A. Ohtomo, D. A. Muller, J. L. Grazul, and H. Y. Hwang, Artificial charge-modulation in atomic-scale perovskite titanate superlattices, Nature **419**, 378 (2002).

[2] T. Arima, Y. Tokura, and J. B. Torrance, Variation of optical gaps in perovskite-type 3*d* transition-metal oxides, Phys. Rev. B **48**, 17006 (1993).

[3] H. Ishida and A. Liebsch, Origin of metallicity of $LaTiO_3/SrTiO_3$ heterostructures, Phys. Rev. B **77**, 115350 (2008).

[4] J. B. Goodenough and J.-S. Zhou, Transport properties, in *Localized to itinerant transitions in perovskite oxides*, edited by J. B. Goodenough, Struct. Bond. **98**, 17 (2001).

[5] M. Mochizuki and M. Imada, Orbital physics in the perovskite Ti oxides, New J. Phys. **6**, 154 (2004).

[6] J. P. Goral and J. E. Greedan, The magnetic structures of $LaTiO_3$ and $CeTiO_3$, J. Magn. Magn. Mater. **37**, 315 (1983).

[7] E. Pavarini, S. Biermann, A. Poteryaev, A. I. Lichtenstein, A. Georges & O. K. Anderson, Mott transition and suppression of orbital fluctuations in orthorhombic $3d^1$ perovskites, Phys. Rev. Lett. **92**, 176403 (2004).

[8] Y. Okimoto, T. Katsufuji, Y. Okada, T. Arima, and Y. Tokura, Optical spectra in $(La,Y)TiO_3$: Variation of Mott-Hubbard gap features with change of electron correlation and band filling, Phys. Rev. B **51**, 9581 (1995).

[9] D. A. Crandles, T. Timusk, J. D. Garrett, and J. E. Greedan, The midinfrared absorption in $RTiO_3$ perovskites (R=La, Ce, Pr, Nd, Sm, Gd): The Hubbard gap? Physica C **201**, 407 (1992).

[10] M. Mochizuki and M. Imada, Origin of G-type antiferromagnetism and orbital-spin structures in $LaTiO_3$, J. Phys. Soc. Jpn. **70**, 2872 (2001).

[11] J. Hemberger, H.-A. Krug von Nidda, V. Fritsch, J. Deisenhofer, S. Lobina, T. Rudolf, P. Lunkenheimer, F. Lichtenberg, A. Loidl, D. Bruns, and B. Büchner, Evidence for Jahn-Teller distortions at the antiferromagnetic transition in $LaTiO_3$, Phys. Rev. Lett. **91**, 066403 (2003).

[12] B. Keimer, D. Casa, A. Ivanov, J. W. Lynn, M. v. Zimmermann, J. P. Hill, D. Gibbs, Y. Taguchi, and Y. Tokura. Spin dynamics and orbital state in $LaTiO_3$, Phys. Rev. Lett. **85**, 3946 (2000).

[13] M. Itoh, M. Tsuchiya, H. Tanaka, and K. Motoya, Orbital ordering and local magnetic properties of Mott-Hubbard insulators $YTiO_3$ and $LaTiO_3$: NMR study, J. Phys. Soc. Jpn. **68**, 2783 (1999).

[14] J. Akimitsu, H. Ichikawa, N. Eguchi, T. Miyano, M. Nishi, and K. Kakurai, Direct observation of orbital ordering in $YTiO_3$ by means of the polarized netron diffraction technique, J. Phys. Soc. Jpn. **70**, 3475 (2001).

[15] Y. Tokura, Y. Taguchi, Y. Okada, Y. Fujishima, T. Arima, K. Kumagai, and Y. Iye, Filling dependence of electronic properties on the verge of metal-Mott-insulator transitions in $Sr_{1-x}La_xTiO_3$, Phys. Rev. Lett. **70**, 2126 (1993).

[16] Y. Okada, T. Arima, Y. Tokura, C. Murayama, and N. Môri, Doping- and pressure-induced change of electrical and magnetic properties in the Mott-Hubbard insulator in $LaTiO_3$, Phys. Rev. B **48**, 9677 (1993).

[17] C. Eylem, Y.-C. Hung, H. L. Ju, J. Y. Kim, D. C. Green, T. Vogt, J. A. Hriljac, B. W. Eichhorn, R. L. Greene, and L. Salamanca-Riba, Unusual metal-insulator transitions in $LaTi_{1-x}V_xO_3$ perovskite phases, Chem. Mater. **8**, 418 (1996).

[18] T. Katsufuji, Y. Taguchi, and Y. Tokura, Transport and magnetic properties of a Mott-Hubbard system whose bandwidth and band filling are controllable: $R_{1-x}Ca_xTiO_{3+y/2}$, Phys. Rev. B **56**, 10145 (1997).

[19] C. C. Hays, J.-S. Zhou, J. T. Markert, and J. B. Goodenough, Electronic transition in $La_{1-x}Sr_xTiO_3$, Phys. Rev. B **60**, 10367 (1999).

[20] T. Higuchi, D. Baba, T. Takeuchi, T. Tsukamoto, Y. Taguchi, Y. Tokura, A. Chainani, and S. Shin, On-site Coulomb energy versus crystal-field splitting for the insulator-metal transition in $La_{1-x}Sr_xTiO_3$, Phys. Rev. B **68**, 104420 (2003).

[21] D. A. Crandles, T. Timusk, J. D. Garrett, and J. E. Greedan, Mott insulator to correlated metal: Optical study of $La_{1-x}TiO_3$, Phys. Rev. B **49**, 16207 (1994).

[22] A. Ohtomo, D. A. Muller, J. L. Grazul, and H. Y. Hwang, Epitaxial growth and electronic structure of $LaTiO_x$ films, Appl. Phys. Lett. **80**, 3922 (2002).

[23] K. H. Kim, D. P. Norton, J. D. Budai, M. F. Chisholm, B. C. Sales, D. K. Christen, and C. Cantoni, Epitaxial structure and transport in $LaTiO_{3+x}$ films on (001) $SrTiO_3$, Phys. Stat. Sol. (a) **200**, 346 (2003).

[24] J. Li, F. B. Wang, P. Wang, M. J. Zhang, H. Y. Tian, and D. N. Zheng, Growth and small-polaron conduction of hole-doped $LaTiO_{3+\delta/2}$ and $NdTiO_{3+\delta/2}$ thin films, Phys. Rev. B **75**, 195109 (2007).

[25] B. Vilquin, T. Kanki, T. Yanagida, H. Tanaka, and T. Kawai, Effect of Sr doping on $LaTiO_3$ thin films, Appl. Surf. Sci. **244**, 494 (2005).

[26] B. Vilquin, T. Kanki, T. Yanagida, H. Tanaka, and T. Kawai, Control of *p*-type conductivity in Sr doped $LaTiO_3$ thin films, Solid State Comm. **136**, 328 (2005).

[27] F. Lichtenberg, D. Widmer, J. G. Bednorz, T. Williams, and A. Reller, Phase diagram of $LaTiO_x$: from 2D layered ferroelectric insulator to 3D weak ferromagnetic semiconductor, Z. Phys. B **82**, 211 (1991).

[28] J. W. Seo, J. Fompeyrine, H. Siegwart, J.-P. Locquet, Oxidation mechanism of $LaTiO_{3.5}$ thin films, Phys. Rev. B **63**, 205401 (2001).

[29] T. Tananka, T. Akahane, E. Bannai, S. Kawai, N. Tsuda, and Y. Ishizawa, Role of polar optical phonon scattering in electrical resistivities of LaB_6 and ReO_3, J. Phys. C: Solid State Phys. **9**, 1235 (1976).

[30] A. Fujimori, I. Hase, H. Namatame, Y. Fujishima, Y. Tokura, H. Eisaki, S. Uchida, K. Takegahara, and F. M. F. de Groot, Evolution of the spectral function in Mott-Hubbard systems with d^1 configuration, Phys. Rev. Lett. **69**, 1796 (1992).

[31] W. A. Harrison, *Electronic Structure and the Properties of Solids: The Physics of the Chemical Bond* (Dover, New York, 1989).

[32] J. B. Goodenough, General considerations, in *Localized to itinerant transition in perovskite oxides*, edited by J. B. Goodenough, Struct. Bond. **98**, 1 (2001).

[33] D. G. Schlom (private communication).

[34] H. D. Zhou and J. B. Goodenough, Coexistence of two electronic phases in $LaTiO_{3+\delta}$ ($0.01 \leq \delta \leq 0.12$) and their evolution with δ, Phys. Rev. B **71**, 165119 (2005).

[35] D. Olaya, F. Pan, C. T. Rogers, and J. C. Price, Superconductivity in La-doped strontium titanate thin films, Appl. Phys. Lett. **84**, 4020 (2004).

[36] H. P. R. Frederikse and W. R. Hosler, Hall mobility in $SrTiO_3$, Phys. Rev. **161**, 822 (1967).

[37] P. Pasierb, S. Komornicki, and M. Rekas, Comparison of the chemical diffusion of undoped and Nb-doped $SrTiO_3$, J. Phys. Chem. Solids **60**, 1835 (1999).

[38] T. Arima and Y. Tokura, Optical study of electronic structure in perovskite-type RMO_3 (*R*=La, Y; *M*=Sc, Ti, V, Cr, Mn, Fe, Co, Ni, Cu), J. Phys. Soc. Jpn. **64**, 2488 (1995).

[39] Y. Ren, A. A. Nugroho, A. A. Menovsky, J. Strempfer, U. Rütt, F. Iga, T. Takabatake, and C. W. Kimball, Orbital-ordering-induced phase transition in $LaVO_3$ and $CeVO_3$, Phys. Rev. B **67**, 014107 (2003).

[40] J. F. Ihlefeld, N. J. Podraza, Z. K. Liu, R. C. Rai, X. Xu, T. Heeg, Y. B. Chen, J. Li, R. W. Collins, J. L. Musfeldt, X. Q. Pan, J. Schubert, R. Ramesh, and D. G. Schlom, Optical band gap of $BiFeO_3$ grown by molecular-beam epitaxy, Appl. Phys. Lett. **92**, 142908 (2008).

[41] A. Grutter, F. Wong, E. Arenholz, M. Liberati, A. Vailionis, and Y. Suzuki, Enhanced magnetism in epitaxial $SrRuO_3$ thin films, Appl. Phys. Lett. **96**, 082509 (2010).

[42] A. T. Zayak, X. Huang, J. B. Neaton, and K. M. Rabe, Structural, electronic, and magnetic properties of $SrRuO_3$ under epitaxial strain, Phys. Rev. B **74**, 094104 (2006).

[43] K. Maiti and R. S. Singh, Evidence against strong correlation in 4*d* transition-metal oxides $CaRuO_3$ and $SrRuO_3$, Phys. Rev. B **71**, 161102(R) (2005).

[44] J. Xia, W. Siemons, G. Koster, M. R. Beasley, and A. Kapitulnik, Critical thickness for itinerant ferromagnetism in ultrathin films of $SrRuO_3$, Phys. Rev. B **79**, 140407(R) (2009).

[45] R. R. Heikes, R. C. Miller, and R. Mazelsky, Magnetic and electrical anomalies in $LaCoO_3$, Physica **30**, 1600 (1964).

[46] D. Fuchs, E. Arac, C. Pinta, S. Schuppler, R. Schneider, H. v. Löhneysen, Tuning the magnetic properties of $LaCoO_3$ thin films by epitaxial strain, Phys. Rev. B **77**, 014434 (2008).

[47] V. V. Mehta, M. Liberati, F. J. Wong, R. V. Chopdekar, E. Arenholz, and Y. Suzuki, Ferromagnetism in tetragonally distorted $LaCoO_3$ thin films, J. Appl. Phys. **105**, 07E503 (2009).

[48] J. M. Rondinelli and N. A. Spaldin, Structural effects on the spin-state transition in epitaxially strained $LaCoO_3$ films, Phys. Rev. B **79**, 054409 (2009).

Chapter 5

[1] M. McCormack, S. Jin, T. H. Tiefel, R. M. Fleming, J. A. Phillips, and R. Ramesh, Very large magnetoresistance in perovskite-like La-Ca-Mn-O thin films, Appl. Phys. Lett. **64**, 3045 (1994).

[2] S. Maekawa, T. Tohyama, S. E. Barnes, S. Ishihara, W. Koshibae, and G. Khaliullin, *Physics of Transition Metal Oxides* (Springer, Berlin, 2004).

[3] C. Zener, Interaction between the *d*-shells in the transition metals. II. Ferromagnetic compounds of manganese with perovskite structure, Phys. Rev. **82**, 403 (1951).

[4] P.-G. de Gennes, Effects of double exchange in magnetic crystals, Phys. Rev. **118**, 141 (1960)

[5] M. Yu. Kagan, D. I. Khomskii, and M. V. Mostovoy, Double-exchange model: phase separation versus canted spins, Eur. Phys. J. B **12**, 217 (1999).

[6] M. Uehara, S. Mori, C. H. Chen, and S.-W. Cheong, Percolative phase separation underlies colossal magnetoresistance in mixed-valent manganites, Nature **399**, 560 (1999).

[7] A. Moreo, M. Mayr, A. Feiguin, S. Yunoki, and E. Dagotto, Giant cluster coexistence in doped manganites and other compounds, Phys. Rev. Lett. **84**, 5568 (2000).

[8] Y. Tokura, Critical features of colossal magnetoresistive manganites, Rep. Prog. Phys. **69**, 797 (2006).

[9] A. K. Kundu, M. M. Seikh, K. Ramesha, and C. N. R. Rao, Novel effects of size disorder on the electronic and magnetic properties of rare earth manganates of the type $La_{0.7-x}Ln_xBa_{0.3}MnO_3$ (Ln = Pr, Nd, Gd or Dy) with large average radius of the A-site cations, J. Phys.: Condens. Matter **17**, 4171 (2005).

[10] T. S. Santos, S. J. May, J. L. Robertson, and A. Bhattacharya, Tuning between the metallic antiferromagnetic and ferromagnetic phases of $La_{1-x}Sr_xMnO_3$ near x=0.5 by digital synthesis, Phys. Rev. B **80**, 155114 (2009).

[11] C. Şen, G. Alvarez, and Elbio Dagotto, Competing ferromagnetic and charge-ordered states in models for manganites: The origin of the colossal magnetoresistance effect, Phys. Rev. Lett. **98**, 127202 (2007).

[12] P. G. Radaelli, R. M. Ibberson, D. N. Argyriou, H. Casalta, K. H. Andersen, S.-W. Cheong, and J. F. Mitchell, Mesoscopic and microscopic phase segregation in manganese perovskites, Phys. Rev. B **63**, 172419 (2001).

[13] T. Z. Ward, J. D. Budai, Z. Gai, J. Z. Tischler, L. Yin, and J. Shen, Elastically driven anisotropic percolation in electronic phase-separated manganites, Nature Phys. **5**, 885 (2009).

[14] K. Lai, M. Nakamura, W. Kundhikanjana, M. Kawasaki, Y. Tokura, M. A. Kelly, and Z.-X. Shen, Mesoscopic percolating resistance network in a strained manganite thin film, Science **329**, 190 (2010).

[15] M. Tokunaga, N. Miura, Y. Tomioka, and Y. Tokura, High-magnetic-field study of phase transitions of $R_{1-x}Ca_xMnO_3$ (R=Pr, Nd), Phys. Rev. B **57**, 5259 (1998).

[16] H. E. Mohottala, B. O. Wells, J. I. Budnick, W. A. Hines, Ch. Niedermayer, L. Udby, C. Bernhard, A. R. Moodenbaugh, and F.-C. Chou, Phase separation in superoxygenated $La_{2-x}Sr_xCuO_{4+y}$, Nature Mater. **5**, 377 (2006).

[17] J. T. Park, D. S. Inosov, Ch. Niedermayer, G. L. Sun, D. Haug, N. B. Christensen, R. Dinnebier, A. V. Boris, A. J. Drew, L. Schulz, T. Shapoval, U. Wolff, V. Neu, X. Yang, C. T. Lin, B. Keimer, and V. Hinkov, Electronic phase separation in the slightly underdoped iron pnictide superconductor $Ba_{1-x}K_xFe_2As_2$, Phys. Rev. Lett. **102**, 117006 (2009).

[18] J. van den Brink, G. Khaliullin, and D. Khomskii, Orbital effects in manganites, edited by T. Chatterji, *Colossal magnetoresistive manganites* (Kluwer Academic, Dordrecht 2004).

[19] J. Kanamori, Crystal distortion in magnetic compounds, J. Appl. Phys. **31**, 14S (1960).

[20] Th. Proffen, R. G. DiFrancesco, S. J. L. Billinge, E. L. Brosha, and G. H. Kwei, Measurement of the local Jahn-Teller distortion in $LaMnO_{3.006}$, Phys. Rev. B **60**, 9973 (1999).

[21] Y. Murakami, J. P. Hill, D. Gibbs, M. Blume, I. Koyama, M. Tanaka, H. Kawata, T. Arima, Y. Tokura, K. Hirota, and Y. Endoh, Resonant x-ray scattering from orbital ordering in $LaMnO_3$, Phys. Rev. Lett. **81**, 582 (1998).

[22] M. B. Salamon and M. Jaime, The physics of manganites: Structure and transport, Rev. Mod. Phys. **73**, 583 (2001).

[23] A. J. Millis, T. Darling, and A. Migliori, Quantifying strain dependence in "colossal" magnetoresistance manganites, J. Appl. Phys. **83**, 1588 (1998).

[24] A. J. Millis, Lattice effects in magnetoresistive manganese perovskites, Nature **392**, 147 (1998).

[25] A. Lanzara, N. L. Saini, M. Brunelli, F. Natali, A. Bianconi, P. G. Radaelli, and S.-W. Cheong, Crossover from large to small polarons across the metal-insulator transition in manganites, Phys. Rev. Lett. **81**, 878 (1998).

[26] M. Jaime, P. Lin, S. H. Chun, M. B. Salamon, P. Dorsey, and M. Rubinstein. Coexistence of localized and itinerant carriers near T_C in calcium-doped manganites. Phys. Rev. B **60**, 1028 (1999).

[27] A. S. Alexandrov, A. M. Bratkovsky, and V. V. Kabanov, Phase coexistence and resistivity near the ferromagnetic transition of manganites, Phys. Rev. Lett. **96**, 117003 (2006).

[28] V. B. Shenoy, D. D. Sarma, and C. N. R. Rao, Electronic phase separation in correlated oxides: The phenomenon, its present status and future prospects, Chem. Phys. Chem. **7**, 2053 (2006).

[29] T. Hotta and E. Dagotto, Theory of manganites, edited by T. Chatterji. *Colossal magnetoresistive manganites* (Kluwer Academic, Dordrecht 2004).

[30] G. Hu and Y. Suzuki, Negative spin polarization of Fe_3O_4 in magnetite/manganite based junctions, Phys. Rev. Lett. **89**, 276601 (2002).

[31] L. M. B. Alldredge, R. V. Chopdekar, B. B. Nelson-Cheeseman, and Y. Suzuki, Spin-polarized conduction in oxide magnetic tunnel junctions with magnetic and nonmagnetic insulating barrier layers, Appl. Phys. Lett. **89**, 182504 (2006).

[32] Y. Ishii, H. Yamada, H. Sato, H. Akoh, Y. Ogawa, M. Kawasaki, and Y. Tokura, Improved tunneling magnetoresistance in interface engineered $(La,Sr)MnO_3$ junctions, Appl. Phys. Lett. **89**, 042509 (2006).

[33] B. B. Nelson-Cheeseman, R. V. Chopdekar, L. M. B. Alldredge, J. S. Bettinger, E. Erenholz, and Y. Suzuki, Probing the role of the barrier layer in magnetic tunnel junction transport, Phys. Rev. B **76**, 220410 (2007).

[34] B. B. Nelson-Cheeseman, F. J. Wong, R. V. Chopdekar, E. Arenholz, and Y. Suzuki, Room temperature magnetic barrier layers in magnetic tunnel junctions, Phys. Rev. B **81**, 214421 (2010).

[35] Y. Ding, D. Haskel, Y.-C. Tseng, E. Kaneshita, M. van Veenendaal, J. F. Mitchell, S. V. Sinogeikin, V. Prakapenka, and H.-K. Mao, Pressure-induced magnetic transition in manganite ($La_{0.75}Ca_{0.25}MnO_3$), Phys. Rev. Lett. **102**, 237201 (2009).

[36] S. Mukhopadhyay, I. Das, and S. Banerjee, Colossal enhancement of mangetoresistance in $La_{0.67}Sr_{0.33}MnO_3$ thin films: Possible evidence of electronic phase separation, J. Phys.: Condens. Matter **21**, 026017 (2009).

[37] H.-U. Habermeier, Strategies towards controlling strain-induced mesoscopic phase separation in manganite thin films, J. Phys.: Condens. Matter **20**, 434228 (2008).

[38] Z. Huang, G. Gao, Z. Yin, X. Feng, Y. Chen, X. Zhao, J. Sun, and W. Wu, Control of the charge-ordering-insulating phase in epitaxial $La_{1-x}Sr_xMnO_3$ (x=0.30-0.45) thin films under the anisotropic strain, J. Appl. Phys. **105**, 113919 (2009).

[39] A. Geddo Lehmann, C. Sanna, N. Lampis, F. Congiu, G. Concas, L. Maritato, C. Aruta, and A. Yu. Petrov, Effect of the substrates ferroelastic transition on epitaxial $La_{0.7}Sr_{0.3}MnO_3$ films grown on $LaAlO_3$, Eur. Phys. J. B **55**, 337 (2007).

[40] Y. Takamura, R. V. Chopdekar, E. Arenholz, and Y. Suzuki, Control of the magnetic and magnetotransport properties of $La_{0.67}Sr_{0.33}MnO_3$ thin films through epitaxial strain, Appl. Phys. Lett. **92**, 162504 (2008).

[41] A. Tebano, A. Orsini, D. Di Castro, P. G. Medaglia, and G. Balestrino, Interplay between crystallographic orientation and electric transport properties in $La_{2/3}Sr_{1/3}MnO_3$ films, Appl. Phys. Lett. **96**, 092505 (2010).

[42] A. Biswas, M. Rajeswari, R. C. Srivastava, T. Venkatesan, R. L. Greene, Q. Lu, A. L. de Lozanne, and A. J. Millis, Strain-driven charge-ordered state in $La_{0.67}Ca_{0.33}MnO_3$, Phys. Rev. B **63**, 184424 (2001).

[43] E. S. Vlakhov, K. A. Nenkov, T. G. Donchev, E. S. Mateev, and R. A. Chakalov, Ferromagnetic and charge ordering competition in strained thin films of $La_{1-x}Ca_xMnO_3$ system, Vacuum **76**, 249 (2004).

[44] F. Tsui, M. C. Smoak, T. K. Nath, and C. B. Eom, Strain-dependent magnetic phase diagram of epitaxial $La_{0.67}Sr_{0.33}MnO_3$ thin films, Appl. Phys. Lett. **76**, 2421 (2000).

[45] P. Dey, T. K. Nath, and A. Taraphder, Effect of substrate-induced strain on transport and magnetic properties of epitaxial $La_{0.66}Sr_{0.33}MnO_3$, Appl. Phys. Lett. **91**, 012511 (2007).

[46] C. Adamo, X. Ke, H. Q. Wang, H. L. Xin, T. Heeg, M. E. Hawley, W. Zander, J. Schubert, P. Schiffer, D. A. Muller, L. Maritato, and D. G. Schlom, Effect of biaxial strain on the electrical and magnetic properties of (001) $La_{0.7}Sr_{0.3}MnO_3$ thin films, Appl. Phys. Lett. **95**, 112504 (2009).

[47] S. Geller and V. B. Bala, Crystallographic studies of perovskite-like compounds. 2. Rare-earth aluminates, Acta Cryst. **9**, 1019 (1956).

[48] S. Bueble, K. Knorr, E. Brecht, W. W. Schmahl, Influence of the ferroelastic twin domain structure on the {100} surface morphology of $LaAlO_3$ HTSC substrates, Surf. Sci. **400**, 345-355 (1998).

[49] F. Borsa, M. L. Crippa, and B. Derighetti, NMR study of the structural phase transition in lanthanum aluminate, Phys. Lett. **34A**, 5 (1971).

[50] C. H. Kim, J. W. Jang, S. Y. Cho, I. T. Kim, and K. S. Hong, Ferroelastic twins in $LaAlO_3$ polycrystals, Physica B **262**, 438-443 (1999).

[51] R. C. O'Handley, *Modern Magnetic Materials: Principles and Applications* (Wiley, New York, 2000).

[52] Y. Suzuki and H. Y. Hwang, Anisotropy of magnetoresistance in (110) $La_{0.7}Sr_{0.3}MnO_3$ thin films, J. Appl. Phys. **85**, 4797 (1999).

[53] G. Colizzi, A. Filippetti, F. Cossu, and V. Fiorentini, Interplay of strain and magnetism in $La_{1-x}Sr_xMnO_3$ from first principles, Phys. Rev. B **78**, 235122 (2008).

[54] H. Y. Hwang, S.-W. Cheong, N. P. Ong, and B. Batlogg, Spin-polarized intergrain tunneling in $La_{2/3}Sr_{1/3}MnO_3$, Phys. Rev. Lett. **77**, 2041 (1996).

[55] A. Gupta, G. Q. Gong, G. Xiao, P. R. Duncombe, P. Lecoeur, P. Trouilloud, Y. Y. Wang, V. P. Dravid, and J. Z. Sun, Grain-boundary effects on the magnetoresistance properties of perovskite manganite films, Phys. Rev. B **54**, R15629 (1996).

[56] T. Z. Ward, S. Liang, K. Fuchigami, L. F. Yin, E. Dagotto, E. W. Plummer, and J. Shen, Reemergent metal-insulator transitions in manganites exposed with spatial confinement, Phys. Rev. Lett. **100**, 247204 (2008).

[57] Yu. A. Boikov, D. Erts, and T. Claeson, Impact of granularity on transport properties of mechanically stressed $La_{0.67}Ca_{0.33}MnO_3$ films, Mater. Sci. Eng. B **79**, 133 (2001).

[58] M. C. Dekkar, A. D. Rata, K. Boldyreva, S. Oswald, L. Schultz, and K. Dörr, Colossal elastoresistance and strain-dependent magnetization of phase-separated $(Pr_{1-y}La_y)_{0.7}Ca_{0.3}MnO_3$ thin films, Phys. Rev. B **80**, 144402 (2009).

[59] R. Mathieu, D. Akahoshi, A. Asamitsu, Y. Tomioka, and Y. Tokura, Colossal magnetoresistance with phase separation: Disorder-induced spin glass state and nanometer scale orbital-charge correlation in half doped manganites, Phys. Rev. B **93**, 227202 (2004).

Chapter 6

[1] A. Ohtomo and H. Y. Hwang, A high-mobility electron gas at the $LaAlO_3/SrTiO_3$ heterointerface, Nature **427**, 423 (2004).

[2] N. Nakagawa, H. Y. Hwang, and D. A. Muller, Why some interfaces cannot be sharp, Nature Mater. **5**, 204 (2006).

[3] S. Thiel, G. Hammerl, A. Schmehl, C. W. Schneider, and J. Mannhart, Tunable quasi-two-dimensional electron gases in oxide heterostructures, Science **313**, 1942 (2006).

[4] G. Herranz, M. Basletić, M. Bibes, C. Carrétéro, E. Tafra, E. Jacquet, K. Bouzahouane, C. Deranlot, A. Hamzić, J.-M. Broto, A. Barthélémy, and A. Fert, High mobility in $LaAlO_3/SrTiO_3$ heterostructures: Origins, dimensionality, and perspectives, Phys. Rev. Lett. **98**, 216803 (2007).

[5] A. Kalabukhov, R. Gunnarsson, J. Börjesson, E. Olsson, T. Claeson, and D. Winkler, Effect of oxygen vacancies in the $SrTiO_3$ substrate on the electrical properties of the $LaAlO_3/SrTiO_3$ interface, Phys. Rev. B **75**, 121404(R) (2007).

[6] W. Siemons, G. Koster, H. Yamamoto, T. H. Geballe, D. H. A. Blank, and M. R. Beasley, Experimental investigation of electronic properties of buried heterointerfaces of $LaAlO_3$ on $SrTiO_3$, Phys. Rev. B **76**, 155111 (2007).

[7] N. Reyren, S. Thiel, A. D. Caviglia, L. Fitting Kourkoutis, G. Hammerl, C. Richter, C. W. Schneider, T. Knopp, A.-S. Rüetschi, D. Jaccard, M. Gabay, D. A. Muller, J.-M. Triscone, and J. Mannhart, Superconducting interfaces between insulating oxides, Science **317**, 1196 (2007).

[8] A. Brinkman, M. Huijben, M. van Zalk, J. Huijben, U. Zeitler, J. C. Maan, W. G. van der Wiel, G. Rijnders, D. H. A. Blank, and H. Hilgenkamp, Magnetic effects at the interface between non-magnetic oxides, Nature Mater. **6**, 493 (2007).

[9] F. J. Wong, M. Chi, R. V. Chopdekar, B. B. Nelson-Cheeseman, N. D. Browning, and Y. Suzuki, Potential barrier lowering and electrical transport at the $LaAlO_3/SrTiO_3$ heterointerface, arXiv:0809.0926.

[10] S. Gemming and G. Seifert, Acta Mater, $SrTiO_3(001)|LaAlO_3(001)$ multilayers: A density-functional investigation, Act. Mater. **54**, 4299 (2006).

[11] M. S. Park, S. H. Rhim, and A. J. Freeman, Charge compensation and mixed valency in $LaAlO_3/SrTiO_3$ heterointerfaces studied by FLAPW method, Phys. Rev. B **74**, 205416 (2006).

[12] R. Pentcheva and W. E. Pickett, Charge localization or itineracy at $LaAlO_3/SrTiO_3$ interfaces: Hole polarons, oxygen vacancies, and mobile electrons, Phys. Rev. B **74**, 035112 (2006).

[13] J. Lee and A. A. Demkov, Theoretical investigation of the band alignment at the $LaAlO_3/SrTiO_3$ interface, Mater. Res. Soc. Symp. Proc. **966**, T07-33 (2007).

[14] O. Copie, V. Garcia, C. Bödefeld, C. Carrétéro, M. Bibes, G. Herranz, E. Jacquet, J.-L. Maurice, B. Vinter, S. Fusil, K. Bouzehouane, H. Jaffrès, and A. Barthélémy, Toward two-dimensional metallic behavior at $LaAlO_3/SrTiO_3$ interfaces, Phys. Rev. Lett. **102**, 216804 (2009).

[15] M. Basletic, J. L. Maurice, C. Carrétéro, G. Herranz, O. Copie, M. Bibes, E. Jacquet, K. Bouzehouane, S. Fusil, and A. Barthélémy, Mapping the spatial distribution of charge carriers in $LaAlO_3/SrTiO_3$ heterostructures, Nature Mater. **7**, 621 (2008).

[16] O. N. Tufte and P. W. Chapman, Electron mobility in semiconducting strontium titanate, Phys. Rev. **155**, 796 (1967).

[17] C. Lee, J. Yahia, and J. L. Brebner, Electronic conduction in slightly reduced strontium titanate at low temperatures, Phys. Rev. B **3**, 2525 (1971).

[18] D. G. Schlom (private communication).

[19] H. Kroemer, Nobel lecture: Quasielectric fields and band offsets: teaching electrons new tricks, Rev. Mod. Phys. **73**, 783 (2001).

[20] W. A. Harrison, E. A. Kraut, J. R. Waldrop, and R. W. Grant, Polar heterojunction interfaces, Phys. Rev. B **18**, 4402 (1978).

[21] T. Schneider, A. D. Caviglia, S. Gariglio, N. Reyren, and J.-M. Triscone, Electrostatically-tuned superconductor-metal-insulator quantum transition at the $LaAlO_3/SrTiO_3$ interface, Phys. Rev. B **79**, 184502 (2009).

[22] C. Bell, S. Harashima, Y. Kozuka, M. Kim, B. G. Kim, Y. Hikita, and H. Y. Hwang, Dominant mobility modulation by the electric field effect at the $LaAlO_3/SrTiO_3$ interface, Phys. Rev. Lett. **103**, 226802 (2009).

[23] A. D. Caviglia, M. Gabay, S. Gariglio, N. Reyren, C. Cancellieri, and J.-M. Triscone, Tunable Rashba spin-orbit interaction at oxide interfaces, Phys. Rev. Lett. **104**, 126803 (2010).

[24] M. Ben Shalom, M. Sachs, D. Rakhmilevitch, A. Palevski, and Y. Dagan, Tuning spin-orbit coupling and superconductivity at the $SrTiO_3/LaAlO_3$ interface: A mangetotransport study, Phys. Rev. Lett. **104**, 126802 (2010).

[25] C. Cen, S. Thiel, G. Hammerl, C. W. Schneider, K. E. Andersen, C. S. Hellberg, J. Mannhart, and J. Levy, Nanoscale control of an interfacial metal-insulator transition at room temperature, Nature Mater. **7**, 298 (2008).

[26] D. F. Bogorin, C. W. Park, H. W. Jang, C. Cen, C. M. Folkman, C.-B. Eom, and J. Levy, Nanoscale rectification at the $LaAlO_3/SrTiO_3$ interface, Appl. Phys. Lett. **97**, 013102 (2010).

[27] N. Reyren, S. Gariglio, A. D. Caviglia, D. Jaccard, T. Schneider, and J.-M. Triscone, Anisotropy of the superconducting transport properties of the $LaAlO_3/SrTiO_3$ interface, Appl. Phys. Lett. **94**, 112506 (2009).

[28] M. Ben Shalom, C. W. Tai, Y. Lereah, M. Sachs, E. Levy, D. Rakhmilevitch, A. Palevski, and Y. Dagan, Anisotropic magnetotransport at the $SrTiO_3/LaAlO_3$ interface, Phys. Rev. B **80**, 140403(R) (2009).

[29] A. D. Caviglia, S. Gariglio, C. Cancellieri, B. Sacépé, A. Fête, N. Reyren, M. Gabay, A. F. Morpurgo, and J.-M. Triscone, Two-dimensional quantum oscillations of the conductance at $LaAlO_3/SrTiO_3$ interfaces, Phys. Rev. Lett. **105**, 236802 (2010).

[30] S. Seri and L. Klein, Antisymmetric magnetoresistance of the $SrTiO_3/LaAlO_3$ interface, Phys. Rev. B **80**, 180410(R) (2009).

[31] R. Dingle, H. L. Störmer, A. C. Gossard, and W. Wiegmann, Electron mobilities in modulation-doped semiconductor heterojunction superlattices, Appl. Phys. Lett. **33**, 665 (1978).

[32] S. Hiyamizu, J. Saito, K. Nanbu, and T. Ishikawa, Improved electron mobility higher than 10^6 cm^2/Vs in selectively doped GaAs/*N*-AlGaAs heterostructures grown by MBE, Jap. J. Appl. Phys. **22**, L609 (1983).

[33] W. Walukiewicz, H. E. Ruda, J. Lagowski, and H. C. Gatos, Electron mobility in modulation-doped heterostructures, Phys. Rev. B **30**, 4571 (1984).

[34] S. Heikman, S. Keller, Y. Wu, J. S. Speck, S. P. DenBaars, and U. K. Mishra, Polarization effects in AlGaN/GaN and GaN/AlGaN/GaN heterostructures, J. Appl. Phys. **93**, 10114 (2003).

[35] L. Hsu and W. Walukiewicz, Theoretical transport studies of *p*-type GaN/AlGaN modulation-doped heterostructures, Appl. Phys. Lett. **74**, 2405 (1999).

[36] M. S. Shur, A. D. Bykhovski, R. Gaska, Two-dimensional hole gas induced by piezoelectric and pyroelectric charges, Solid-State Electron. **44**, 205 (2000).

[37] A. Tsukazaki, A. Ohtomo, T. Kita, Y. Ohno, H. Ohno, and M. Kawasaki, Quantum Hall effect in polar oxide heterostructures, **315**, 1388 (2007).

[38] R. C. Neville, B. Hoeneisen, and C. A. Mead, Permittivity of strontium titanate, J. Appl. Phys. **43**, 2124 (1972).

[39] A. B. Pippard, *Magnetoresistance in Metals* (Cambridge UP, Cambridge, 1989).

[40] E. Abrahams, P. W. Anderson, D. C. Licciardello, and T. V. Ramakrishnan, Scaling theory of localization: Absence of quantum diffusion in two dimensions, Phys. Rev. Lett. **42**, 673 (1979).

[41] H. Chen, A. M. Kolpak, and S. Ismail-Beigi, Fundamental asymmetry in interfacial electronic reconstruction between insulating oxides: An *ab initio* study, Phys. Rev. B **79**, 161402(R) (2009).

[42] R. Pentcheva and W. E. Pickett, Ionic relaxation contribution to the electronic reconstruction at the *n*-type $LaAlO_3/SrTiO_3$ interface, Phys. Rev. B **78**, 205106 (2008).

[43] P. Perna, D. Maccariello, M. Radovic, U. Scotti di Uccio, I. Pallecchi, M. Codda, D. Marré, C. Cantoni, J. Gazquez, M. Varela, S. J. Pennycook, and F. Miletto Granozio, Conducting interfaces between band insulating oxides: The $LaGaO_3/SrTiO_3$ heterostructure, Appl. Phys. Lett. **97**, 152111 (2010).

[44] D. C. Dube, H. J. Scheel, I. Reaney, M. Daglish, and N. Setter, Dielectric properties of lanthanum gallate ($LaGaO_3$) crystal, J. Appl. Phys. **75**, 4126 (1994).

[45] R. L. Sandstrom, E. A. Giess, W. J. Gallagher, A. Segmüller, E. I. Cooper, M. F. Chisholm, A. Gupta, S. Shinde, and R. B. Laibowitz, Lanthanum gallate substrates for epitaxial high-temperature superconducting thin films, Appl. Phys. Lett. **53**, 1874 (1988).

[46] Yu. F. Komnik, V. V. Andrievskii, and I. B. Berkutov, Manifestation of the spin-orbit interaction in bismuth films in a parallel magnetic field, Low Temp. Phys. **33**, 79 (2007).

[47] T. Kawaguti and Y. Fujimori, Magnetoresistance and inelastic scattering time in thin films of silver and gold in weakly localized regime, J. Phys. Soc. Jpn. **52**, 722 (1983).

[48] G. Bergmann, Influence of spin-orbit coupling on weak localization, Phys. Rev. Lett. **48**, 1046 (1982).

[49] G. Bergmann, Weak anti-localization—an experimental proof for the destructive interference of rotated spin 1/2, Solid State Commun. **42**, 815 (1982).

[50] P. E. Lindelof and S. Wang, Bulk and surface spin-orbit relaxation of the conduction electrons separated by weak-localization experiments, Phys. Rev. B **33**, 1478 (1986).

[51] G. L. Chen, J. Han, T. T. Huang, S. Datta, and D. B. Janes, Observation of the interfacial-field-induced weak antilocalization in InAs quantum structures, Phys. Rev. B **47**, 4084(R) (1993).

[52] S. Datta and B. Das, Electronic analog of the electro-optic modulator, Appl. Phys. Lett. **56**, 665 (1990).

[53] E. M. Hankiewicz and G. Vignale, Spin-Hall effect and spin-Coulomb drag in doped semiconductors, J. Phys.: Condens. Matter **21**, 253202 (2009).

[54] L. F. Mattheiss, Energy bands for $KNiF_3$, $SrTiO_3$, $KMoO_3$, and $KTaO_3$, Phys. Rev. B **6**, 4718 (1972).

[55] W. Luo, W. Duan, S. G. Louie, and M. L. Cohen, Structural and electronic properties of *n*-doped and *p*-doped $SrTiO_3$, Phys. Rev. B **70**, 214109 (2004).

[56] Y. Yamada and Y. Kanemitsu, Band-to-band photoluminescence in $SrTiO_3$, Phys. Rev. B **82**, 121103(R) (2010).

[57] A. Fert, Origin, development, and future of spintronics (Nobel lecture), Angew. Chem. Int. Ed. **47**, 5956 (2008).

[58] K. Yada, S. Onari, Y. Tanaka, and J. Inoue, Electrically controlled superconducting states at the heterointerface $SrTiO_3/LaAlO_3$, Phys. Rev. B **80**, 140509(R) (2009).

[59] B. Liu and X. Hu, Local electronic structure of the superconducting interface $LaAlO_3/SrTiO_3$, Phys. Rev. B **81**, 144504 (2010).

[60] K. S. Takahashi, M. Kawasaki, and Y. Tokura, Interface ferromagnetism in oxide superlattices of $CaMnO_3/CaRuO_3$, Appl. Phys. Lett. **79**, 1324 (2001).

[61] L. S. Senhouse, G. E. Smith, and M. V. DePaolis, Cyclotron resonance in potassium tantalite, Phys. Rev. Lett. **15**, 776 (1965).

Afterword

[1] M. Imada, A. Fujimori, and Y. Tokura, Metal-insulator transitions, Rev. Mod. Phys. **70**, 1039 (1998).

[2] J. Cao, E. Ertekin, V. Srinivasan, W. Fan, S. Huang, H. Zheng, J. W. L Yim, D. R. Khanal, D. F. Ogletree, J. C. Grossman, and J. Wu, Strain engineering and one-dimensional organization of metal-insulator domains in single-crystal vanadium dioxide beams, Nature Nanotech. **4**, 732 (2009).

[3] A. Ariando, X. Wang, G. Baskaran, Z. Q. Liu, J. Huijben, J. B. Yi, A. Annadi, A. Roy Barman, A. Rusydi, S. Dhar, Y. P. Feng, J. Ding, H. Hilgenkamp, and T. Venkatesan, Electronic phase separation at the $LaAlO_3/SrTiO_3$ interface, Nature Comm. **2**, 118 (2011).

[4] M. Breitschaft, V. Tinkl, N. Pavlenko, S. Paetel, C. Richter, J. R. Kirtley, Y. C. Liao, G. Hammerl, V. Eyert, T. Kopp, and J. Mannhart, Two-dimensional electron liquid state at $LaAlO_3$-$SrTiO_3$ interfaces, Phys. Rev. B **81**, 153414 (2010).

Appendix

[1] J. F. Nye, *Physical Properties of Crystals: Their Representation by Tensors and Matrices* (Clarendon, Oxford, 1985).

[2] P. Y. Yu and M. Cardona, *Fundamentals of Semiconductors: Physics and Materials Properties*, 4th edn. (Springer, Berlin, 2010).

[3] P. W. Anderson, Absence of diffusion in certain random lattices, Phys. Rev. **109**, 1492 (1958).

[4] V. F. Gantmakher, *Electrons and Disorder in Solids* (Clarendon, Oxford, 2005).

[5] E. Abrahams, P. W. Anderson, D. C. Licciardello, and T. V. Ramakrishnan, Scaling theory of localization: Absence of quantum diffusion in two dimensions, Phys. Rev. Lett. **42**, 673 (1979).

[6] P. A. Lee and T. V. Ramakrishnan, Disordered electron systems, Rev. Mod. Phys. **57**, 287 (1985).

[7] G. Bergmann, Weak localization in thin films: A time-of-flight experiment with conduction electrons, Phys Rep. **107**, 1 (1984).

[8] G. Bergmann, Weak anti-localization—an experimental proof for the destructive interference of rotated spin 1/2, Solid State Comm. **42**, 815 (1982).

[9] G. Bergmann, Influence of spin-orbit coupling on weak localization, Phys. Rev. Lett. **48**, 1046 (1982).

[10] J. Stöhr and H. C. Siegmann, *Magnetism: From Fundamentals to Nanoscale Dynamics* (Springer, Berlin, 2006).